MVSystems, Inc.
500 Corporate Circle, Ste. L • Golden, Colorado 80401 • USA
TEL. (303) 271-9907 Fax: (303) 271-9771 www.mvsystems.info Email: jhu@mvsystemsinc.com

FINAL REPORT

Photo-electrochemical Hydrogen Production

Reporting period:
September 1, 2007 - September 30, 2013

Contract number:
DE-FC36-07GO17105, A00

Recipient:
MVSystems Inc.

Sub-contractor:
Hawai'i Natural Energy Institute
University of Nevada, Las Vegas

Collaborators:
National Renewable Energy Laboratory

PIs:
Arun Madan (2007-2012)
Jian Hu (2013)

DOE managers:
Eric Miller and David Peterson

Executive Summary

The objectives of this project, covering two phases and an additional extension phase, were the development of thin film-based hybrid photovoltaic (PV)/photoelectrochemical (PEC) devices for solar-powered water splitting. The hybrid device, comprising a low-cost photoactive material integrated with amorphous silicon (a-Si:H or a-Si in short)-based solar cells as a driver, should be able to produce hydrogen with a 5% solar-to-hydrogen conversion efficiency (STH) and be durable for at least 500 hours. Three thin film material classes were studied and developed under this program: *silicon-based compounds*, *copper chalcopyrite-based compounds*, and *metal oxides*.

With the silicon-based compounds, more specifically the amorphous silicon carbide (a-SiC), we achieved a STH efficiency of 3.7% when the photoelectrode was coupled to an a-Si tandem solar cell, and a STH efficiency of 6.1% when using a crystalline Si PV driver. The hybrid PV/a-SiC device tested under a current bias of -3~4 mA/cm^2, exhibited a durability of up to ~800 hours in 0.25 M H_2SO_4 electrolyte. Other than the PV driver, the most critical element affecting the photocurrent (and hence the STH efficiency) of the hybrid PV/a-SiC device was the surface energetics at the a-SiC/electrolyte interface. Without surface modification, the photocurrent of the hybrid PEC device was ~1 mA/cm^2 or lower due to a surface barrier that limits the extraction of photo-generated carriers. We conducted an extensive search for suitable surface modification techniques/materials, of which the deposition of low work function metal nanoparticles was the most successful. Metal nanoparticles of ruthenium (Ru), tungsten (W) or titanium (Ti) led to an anodic shift in the onset potential. We have also been able to develop hybrid devices of various configurations in a monolithic fashion and optimized the current matching via altering the energy bandgap and thickness of each constituent cell. As a result, the short-circuit photocurrent density of the hybrid device (measured in a 2-electrode configuration) increased significantly without assistance of any external bias, i.e. from ≤1 mA/cm^2 to ~5 mA/cm^2.

With the copper chalcopyrite compounds, we have achieved a STH efficiency of 3.7% in a coplanar configuration with 3 a-Si solar cells and one $CuGaSe_2$ photocathode. This material class exhibited good durability at a photocurrent density level of -4 mA/cm2 ("5% STH" equivalent) at a fixed potential (-0.45 V_{RHE}). A poor band-edge alignment with the hydrogen evolution reaction (HER) potential was identified as the main limitation for high STH efficiency. Three new pathways have been identified to solve this issue. First, PV driver with bandgap lower than that of amorphous silicon were investigated. Crystalline silicon was identified as possible bottom cell. Mechanical stacks made with one Si solar cell and one $CuGaSe_2$ photocathode were built. A 400 mV anodic shift was observed with the Si cell, leading to photocurrent density of -5 mA/cm2 at $0V_{RHE}$ (compared to 0 mA/cm^2 at the same potential without PV driver). We also investigated the use of p-n junctions to shift $CuGaSe_2$ flatband potential anodically. Reactively sputtered zinc oxy-sulfide thin films was evaluated as n-type buffer and deposited on $CuGaSe_2$. Ruthenium nanoparticles were then added as HER catalyst. A 250 mV anodic shift was observed with the p-n junction, leading to photocurrent density at $0V_{RHE}$ of -1.5 mA/cm^2. Combining this device with a Si solar cell in a mechanical stack configuration shifted the onset potential further (+400 mV anodically), leading to photocurrent density of -7 mA/cm^2 at $0V_{RHE}$. Finally, we developed wide bandgap copper chalcopyrite thin film materials. We demonstrated that Se can be substituted with S using a simple annealing step. Photocurrent densities in the 5-6 mA/cm^2 range were obtained with red 2.0eV $CuInGaS_2$ photocathodes.

With the metal oxide compounds, we have demonstrated that a WO_3-based hybrid photoelectrode was feasible. Specifically, we showed that WO_3 paired with an a-Si tandem solar cell can generate short circuit photocurrent density of 2.5 mA/cm^2, equivalent to STH efficiency of 3.1%. Long-term durability tests demonstrated WO_3 ability to split water over extended periods, for up to 600 hours at current density levels of 2.0-2.5 mA/cm^2. Efforts have been done to decrease WO_3 bandgap using foreign elements incorporation. We did not manage to reduce the bandgap of WO_3 with this method. However, more promising results have been achieved with bilayered systems, where only the top part of WO_3 films was modified. Also, we have demonstrated that alloying WO_3 with CuO can form 2.2eV bandgap $CuWO_4$. Incorporating conductive carbon nanotubes in $CuWO_4$ reduced its intrinsic bulk resistance. Saturation photocurrent densities in the 0.4-0.5 mA/cm^2 range were achieved. Recently, in collaboration with University of Texas at Arlington, we have identified new quaternary metal oxides with $CuWO_4$ as primary material host. Our experimental work on ceramics confirmed the theoretical calculations that crowned bismuth as a possible candidate to improve $CuWO_4$ water splitting efficiency.

Table of Contents

List of Figures

List of Tables

1. Introduction

This multi-year project aimed to develop thin film-based hybrid photovoltaic (PV)/photoelectrochemical (PEC) devices used for solar assisted water splitting at a hydrogen production cost of ≤$22/kg. In Phase I of this program (September 1, 2007 – December 31, 2010), efforts were made to identify and develop photoelectrode materials which were capable of producing photocurrent ≥4 mA/cm^2, of durability greater than 200 hours, and compatible with the hybrid photoelectrode (HPE) approach when integrated with the amorphous silicon based solar cell as the PV drivers. In Phase 2 (January 1, 2011 – December 31, 2012, plus an extension period of January 1 – September 30, 2013), we focused mainly on improving performance of the hybrid device towards the final DOE's solar-to-hydrogen conversion efficiency (STH) and durability goals. This Final Technical Report covers both Phase I and Phase II of the program. The first part describes the work on amorphous silicon carbide (a-SiC:H or a-SiC) photoelectrodes and the hybrid PV/a-SiC devices, performed at MVSystems, Inc. Then, we present the research activities conducted by the Hawaii Natural Energy Institute (HNEI) on copper-chalcopyrites and the metal oxides compounds. Finally, we present the results of the techno-economic analysis for solar-assisted hydrogen production based on the hybrid PV/a-SiC device.

1.1 Background

Photoelectrochemical dissociation of water into hydrogen and oxygen at a semiconductor-liquid interface offers an environmentally benign approach to hydrogen production. Water splitting using PEC devices that incorporate thin film photoelectrodes and a solar cell in a monolithic structure has the potential for low-cost and efficient hydrogen production.

Fujishima and Honda were the first to investigate the feasibility of using a photoelectrode (n-TiO_2) to produce hydrogen directly from water using sunlight [1]. To this day, binary and ternary transition metal oxides still draw significant attention as they can provide at least a fraction of the energy necessary for water splitting, have good resistance to corrosion and are inexpensive to produce. However, due to the wide energy bandgap (typically ~3 eV) inherent to these materials, photon absorption above 440nm is very limited leading to low STH conversion efficiencies ~0.1% [2-5]. No single system or material having appropriate optical absorption, band alignment and good transport properties has been discovered yet.

Hybrid PV/PEC devices address the problem by having a solar cell supply the additional energy necessary to drive the water splitting reactions [6]. In 1998 Rocheleau at al achieved STH efficiencies as high as 7.8% using a photocathode fabricated from triple junction amorphous silicon solar cells and a separate catalytic anode. This architecture incorporates a solar cell to the device, however, this is not a monolithic structure as the anode is connected to the solar cell by wires. Also, the durability data reported for the oxygen and hydrogen evolution reaction (OER and HER) catalysts used to drive the surface reaction was obtained in separate tests (i.e not the integrated PEC device).

To take full advantage of the hybrid concept, one must incorporate the photoelectrode with a solar cell in a multijunction configuration as shown in Figure 1. Advantages of this system include the elimination of lateral current collection and simplification of device geometry for ease of fabrication [6].

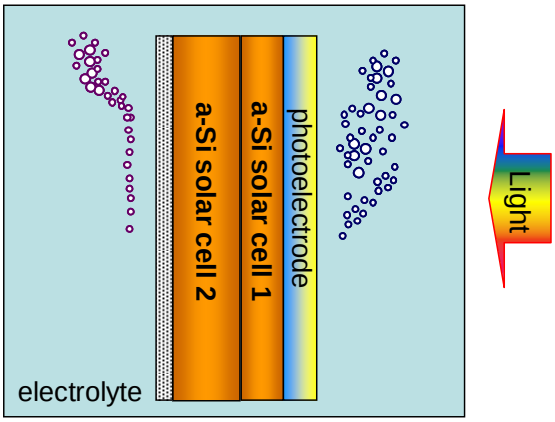

Figure 1 The schematic diagram of the monolithic hybrid PV/PEC device consisting of a photoelectrode (PEC layer) and an amorphous silicon-based tandem solar.

Of the solar cells considered for this application multijunction amorphous silicon cells offer appropriate voltage output, are inexpensive to manufacture and in some cases can be produced in the same deposition system that later deposits the top photoelectrode layer. A noteworthy previous work done with such structures include report by Nocera et al in which earth-abundant metals and cobaltborate catalysts were used in conjunction with an a-Si triple- junction leading to a STH conversion efficiency of 2.5% [7]. The use of semiconductor photoelectrodes such as amorphous silicon (a-Si) and I-III-VI_2 alloys, e.g. $Cu(In_xGa_{1-x})Se_2$ (CIGS), which can be produced with suitable bandgaps should yield higher STH efficiencies.

1.2 Objectives

Based on its potential to meet long-term goals, research and development (R&D) centering on multi-junction hybrid PV/PEC technology defined the scope of this collaborative project. Within this scope, particular emphasis was put in the development of low-cost photoactive materials integrated with a-Si-based solar cells as a driving force with photocurrents greater than 4 mA/cm^2, and with the durability necessary to meet the lifetime requirement of ≥500 hours. Specifically, three thin film material classes were studied and developed for hydrogen production, including *silicon-based compounds*, *copper chalcopyrite-based compounds*, and *metal oxides-based compounds*. In addition to the materials related R&D activities, the development of laboratory-scale demonstration devices and the generation of preliminary energy/economic analysis for hydrogen production cost based on the developed PEC technology were undertaken during the project. To support the device-demonstration activities, appropriate auxiliary components have been developed for incorporation in PEC photoelectrode designs, including attention to the necessary process integration techniques.

1.3 Approaches

The general approach of this collaborative effort focused on the DOE PEC Working Group's "feedback" philosophy integrating state-of-the-art theoretical, synthesis and analytical techniques to identify and develop the most promising materials classes to meet the PEC challenges in efficiency, stability and cost. Materials modeling, bulk-film optimization, film-surface enhancement along with comprehensive material and device characterization have been employed to facilitate the R&D process. More specifically, throughout this project, MVSystems, Inc and the Hawaii Natural Energy Institute (HNEI), in collaboration with the National Renewable Energy Laboratory (NREL), made a joint effort via the following approaches:

- Both photo-anodes and photo-cathodes were evaluated under one program
- All 3 hybrid PEC devices used the a-Si tandem solar cell as a driving engine

This synergistic and feedback approach has been applied to three material classes, to enhance understanding of fundamental performance parameters, and expedite development of process-compatible forms of these materials. The most promising candidate materials were identified, with the short-term goal of demonstrating

laboratory-scale water-splitting devices, and with a long-term goal of transferring the fabrication processes toward the commercial scale.

1.4 Key results

(1) Amorphous silicon-based compound Films

- Fabricated a-SiC photoelectrodes with saturation photocurrent of ~8 mA/cm^2 measured at -2V (vs. SCE) in pH2 aqueous electrolyte;
- Successfully fabricated monolithic PV/a-SiC devices comprising a-SiC photoelectrode and the Si based solar cell. Without assistance of an external bias, the hybrid devices using a-Si solar cells as the driver were capable of producing photocurrent of 3 mA/cm^2, with a STH efficiency of 3.7%. A higher photocurrent of 4.91 mA/cm^2 was obtained using a crystalline Si PV device as a driver, equivalent to a STH efficiency of **6.1%**;
- The hybrid PV/a-SiC devices exhibited a durability of **790 hours** in 0.25 M H_2SO_4 electrolyte, under a current density level of 3 to 4 mA/cm^2 (@1.5V bias).

(2) Copper chalcopyrite-based compounds

- Synthesized copper gallium di-selenide ($CuGaSe_2$) photocathode capable of generating 14 mA/cm^2 at -0.6V_{RHE};
- Demonstrated a **3.7%** STH efficiency using a coplanar device made with 3 a-Si solar cells connected in series with one CuGaSe2 photocathode;
- The durability of $CuGaSe_2$ was demonstrated for **400 hours**. Beyond this period, the thin films generally flecked of the FTO substrates (rather than dissolved);
- New paths have been identified to improve the STH efficiency of copper chalcopyrite-based photocathode, including new PV drivers (crystalline silicon instead of amorphous silicon), the use of p-n structures made with p-type $CuGaSe_2$ and n-type buffers and the development of wide bandgap chalcopyrite materials.

(3) Metal oxide-based compounds

- Achieved a **3.1%** STH efficiency with a WO_3 photoanode coupled with an a-Si tandem solar cell;
- Long-term durability tests demonstrated WO_3 durability for up to **600 hours** at current density levels of 2.0-2.5 mA/cm^2;
- Efforts have been done to decrease WO_3 bandgap using foreign elements incorporation. Good results have been achieved with bilayered systems;
- Demonstrated that WO_3 can be alloyed with CuO to form a 2.2 eV bandgap $CuWO_4$ material. Saturation photocurrent densities in the 0.4-0.5 mA/cm^2 range were achieved;
- Identified new quaternary metal oxides, using $CuWO_4$ as primary material host. Our experimental work on ceramics confirmed the theoretical calculations that crowned bismuth as a possible candidate to improve $CuWO_4$ water splitting efficiency.

(4) Techno-economic analysis (performed for silicon-based compound films)

- A production cost of $19.3 was obtained with a Type 3 reactor using STH efficiencies demonstrated in this program (5%) and absorber costs reported for amorphous silicon-based multijunction PV components ($28/m^2);
- Reducing the material costs (Type 3) or the total area occupied by the solar absorbers (Type 4) has little effect on the cost of hydrogen if the STH efficiency is low (5%);
- The only way to significantly reduce the cost of hydrogen production is to increase the STH efficiency to at least 15%. In this condition, a cost of $4.8 per kg of hydrogen can be achieved.

2. Silicon-Based Compounds

2.1 Motivation and main technology barriers

Amorphous silicon has been investigated for PEC applications but it shows poor durability in the typical aqueous solutions used for PEC [8]. However, the knowledge base on a-Si semiconductors is extensive due to its wide use in thin-film transistors, memory devices and particularly in photovoltaic solar cells. By modifying the composition of the a-Si (alloying), one can improve both the corrosion resistance and bandgap required for PEC water splitting. Hydrogenated amorphous silicon carbide (a-SiC:H or a-SiC) is one of such amorphous silicon alloys. Like a-Si:H, a-SiC:H presents long-range disorder but retains the short-range order. Incorporation of carbon into the amorphous silicon widens the bandgap (Eg), from 1.7 to ~2 eV, making a-SiC:H an ideal material for PEC water splitting [9]. The maximum photocurrent achievable in this semiconductor (with Eg=2 eV) is 14.8 mA/cm^2, corresponding to the maximum STH efficiency of 18.2% (see Figure 2).

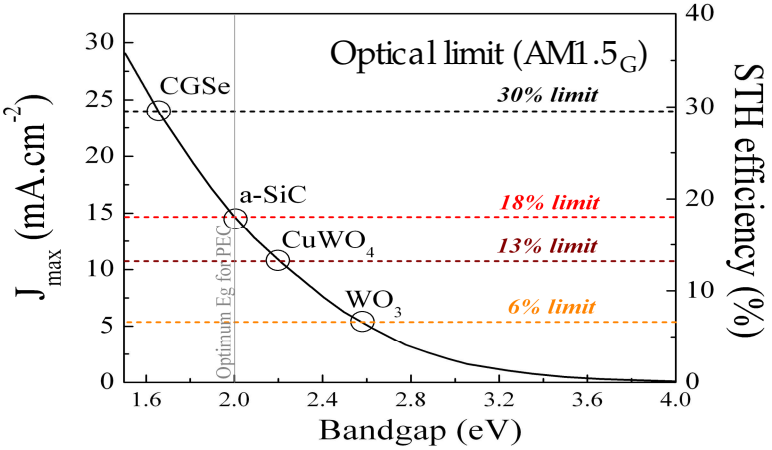

Figure 2 Maximum theoretical photocurrent density and corresponding STH efficiency as a function of the bandgap of various thin films materials used in this project. A total absorption of photons with energy hν ≥ Eg is assumed.

Here, the STH efficiency is defined as [10],

$$STH = \left[\frac{\left| j_{sc}(mA/cm^2) \right| \times (1.23V) \times \eta_F}{P_{total}(mW/cm^2)} \right] \times 100\%, \qquad (1)$$

where j_{sc} is the short-circuit photocurrent density under 1-sun illumination conforming to AM1.5G spectrum; the voltage of 1.23 V is the thermodynamic water splitting potential (based on the Gibbs free energy per mole of H_2 generated, ΔG^0 = 237 kJ/mol at 25 °C); and P_{total} is the impinging sun-light intensity (=100 mW/cm^2 under AM1.5G illumination). η_F is the Faradaic efficiency for hydrogen evolution, which unless specified, is assumed to be 100% throughout this work. Hence, the STH efficiency (%) can be simply calculated as 1.23×j_{sc} (j_{sc} is in unit of mA/cm^2).

Incorporating carbon in the amorphous silicon films should also lead to increase in the corrosion resistance in aqueous electrolyte compared to the conventional a-Si:H films [8]. Furthermore, the bandgap of a-SiC:H can be tuned by altering the flow of carbon source gas during growth. Since the method of fabrication of a-SiC:H films is identical to that of a-Si:H (both using the Plasma Enhanced Chemical Vapor Deposition (PECVD) technique), both PV and PEC components in a hybrid device could be fabricated as a monolithic device and mass-produced in a cost-effective fashion. For all of these reasons, a-SiC:H shows great promise with respect to the major materials-related barriers listed in the US DOE EERE Hydrogen Program plan [11].

2.2 Addressing the challenges

Materials Durability. Although a-SiC:H is known to be more durable than a-Si:H, the corrosion and photo-corrosion behavior over extended time periods and under a variety of electrolyte and environmental conditions were not known.

Materials Efficiency. The band-edge of a-SiC:H could poorly align with the H_2O/O_2 redox potential, and large interfacial barrier at a-SiC/electrolyte interface could exist, inhibiting extraction of photocurrent.

Device Configuration Designs. Although the method for fabrication of a-SiC:H is identical to that used for a-Si solar cells, optimized tandem/multijunction device configurations would need to be fabricated to match the photocurrent and photovoltage characteristics of newly-developed a-SiC photoelectrodes.

Our strategy for achieving the STH efficiency > 5% in the hybrid PV/a-SiC device was to subdivide the entire PEC hydrogen production process into two major parts:

Step 1: Photo-generation of electron-hole pairs in the photoelectrode.
Step 2: Charge transfer through the photoelectrode/electrolyte interface for hydrogen evolution reaction.

Step1 is basically a solid-state process requiring high quality a-SiC:H thin films, whereas Step 2 is related to surface energetics and dynamics at the a-SiC/electrolyte interface. Each step has been investigated thoroughly and optimized towards achieving the highest STH efficiency.

In the following sections, the main results on preparation of a-SiC:H films and fabrication of a-SiC photoelectrodes will be presented. Fabrication of the hybrid PV/a-SiC device and improvement of surface energetics will be described in Sections 2.4.1.1 through 2.4.1.4.

2.3 Fabrication of amorphous silicon carbide (a-SiC) photoelectrodes

2.3.1 Preparation of high quality a-SiC:H thin films

The a-SiC:H films were fabricated in an in-house PECVD cluster tool system built by MVSystems, Inc. A-SiC:H is a well-known amorphous semiconductor for which electronic properties are fundamentally affected by the density of defect states (DOS) in the energy bandgap, which in turn is determined by the PECVD growth process. There are several independent PECVD processing parameters that affect the properties of the film, among those the methane (CH_4) to silane (SiH_4) gas ratio used in the growth of a-SiC:H is one of the key variables. Incorporation of carbon into the film widens the bandgap as needed, however, it also increases disorder in the material since the bonding lengths differ for C-C (1.54 Å) and Si-Si bonds (2.24 Å). Hence, care must be taken to minimize generation of defect density while the bandgap is increased. In the following, the effect of the raw gas ratio, $CH_4/(SiH_4+CH_4)$, on the electrical properties of a-SiC:H films will be described and main results will be presented.

Figure 3(a) and (b) show the variation of bandgap, Eg, photoconductivity (σ_{ph}) and the gamma factor (γ) as a function of $CH_4/(SiH_4+CH_4)$ gas ratio. As $CH_4/(SiH_4+CH_4)$ increases, Eg increases linearly from ~1.8 eV to over 2.0 eV (Figure 3(a)) while σ_{ph} decreases from about 10^{-5} to 10^{-8} S/cm. The dark conductivity (σ_d), not shown here, decreases to $<10^{-12}$ S/cm. The parameter γ is used to infer the DOS in the amorphous semiconductor, defined from the correlation: $\sigma_{ph} \propto F^{\gamma}$, where F is the illumination intensity [9]. High-quality a-Si:H materials generally exhibit $\gamma>0.9$. As shown in Figure 3(b), when $CH_4/(SiH_4+CH_4)$ reaches > 0.35, γ decreases to a low value of ~0.7, indicative of a material with high defect states. For $CH_4/(SiH_4+CH_4)$ <0.3, $\gamma>0.9$, which indicates that the DOS in materials is low. The carbon concentration in a-SiC:H films, as determined by XPS technique, is typically ~7% for films of E_g=2 eV [12].

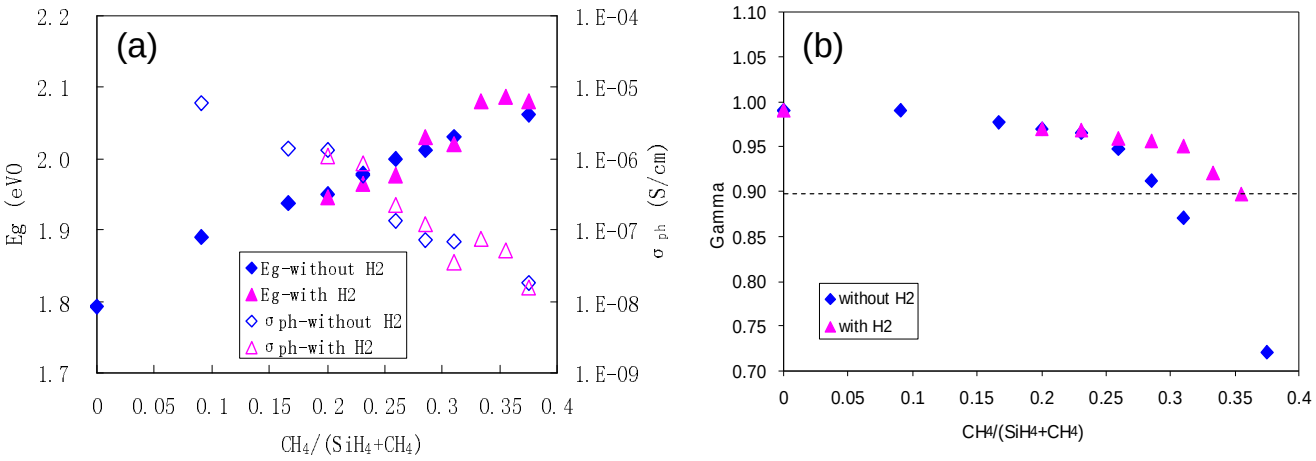

Figure 3 Variation of (a) Eg and σ_{ph} as well as (b) γ with the $CH_4/(SiH_4+CH_4)$ ratio for a-SiC films with and without H_2 dilution during the deposition.

Figure 3 also shows the effect of the hydrogen flow (100 sccm) on the properties of a-SiC:H films. As seen in Figure 3(a), the E_g appears not to be affected by hydrogen dilution. In contrast, the γ factor exhibits a more pronounced change at high $CH_4/(SiH_4+CH_4)$ gas ratio region of >0.25, increasing from <0.9 to ~0.95 at $CH_4/(SiH_4+CH_4)$=0.3, indicating that the DOS is decreased due to H_2 passivation (see Figure 3(b)). It was observed that, the photoconductivity, σ_{ph} increased with increasing H_2 dilution from 4.0 x 10^{-7} S/cm (without H_2 dilution) to 3.2 x 10^{-6} S/cm (H_2 flow rate = 150 sccm) due to the reduced DOS in the film.

It should be noted that the decrease in σ_{ph} with increasing $CH_4/(SiH_4+CH_4)$ gas ratio as shown in Figure 3(a) might not be related to an increase of the DOS in a-SiC:H since the γ factor remains ≥ 0.9. More likely, the decrease of σ_{ph} is due to the reduction in the absorption coefficient as Eg increases. In order to evaluate this further, we measured the photocurrent, I_p, at a specific wavelength (i.e. 600 nm) for which uniform bulk absorption occurs. The wavelength dependent photocurrent can be expressed as,

$$I_p = eN_{ph}(\lambda)(1-R_\lambda)[1-\exp(-\alpha_\lambda d)]\eta\,\tau/t_t, \qquad (2)$$

where $N_{ph}(\lambda)$ is the photon flux, R_λ is the reflection coefficient, α_λ is the absorption coefficient, d is the film thickness, η is the quantum efficiency of photo generation, τ is the recombination lifetime and t_t is the transit time. Assuming that η, τ, t_t and $(1-R_\lambda)$ are constant for different films (i.e. different Eg), then to a first order approximation, the normalized photocurrent, $I_p/(1-\exp(-\alpha_\lambda d))$, can account for the changes in the absorption coefficient as Eg varies. The measurement indeed confirmed that the normalized photocurrent did not change significantly as Eg increased (not shown here). This then suggests that the DOS in the a-SiC:H film has remained low and is consistent with γ >0.9 (low DOS) throughout the range. The results indicate that high quality a-SiC:H with Eg ~ 2.0 eV can be fabricated.

To test the viability of a-SiC:H material in device application, we incorporated it into a normal solar cell in the configuration, glass/Asahi U-Type SnO_2/p-a-SiC/i-a-SiC/n-a-Si/Ag. For the a-SiC intrinsic layer of 300 nm thick, the a-SiC solar cell exhibits an open-circuit voltage (Voc) of 0.91 V, short-circuit current (Jsc) of 11.6 mA/cm^2, and fill factor (FF) of 0.66. In addition, both FF under blue (400 nm) and FF under red (600 nm) illuminations were 0.7, indicative of high quality a-SiC:H material. For an intrinsic layer thickness of ~100 nm, a J_{sc} of ~8.45 mA/cm^2 was obtained. This analysis further confirms that high quality a-SiC:H films can be used as a PEC photoelectrode.

2.3.2 Configuration of the a-SiC photoelectrode and PEC performance

The configuration used for the a-SiC photoelectrode, shown in Figure 4, consists of an intrinsic a-SiC:H and a thin p-type a-SiC:H layer. In general, the a-SiC photoelectrode behaves like a photocathode where the photogenerated electrons inject into the electrolyte at the a-SiC(i)/electrolyte interface to reduce H^+ ions for hydrogen evolution.

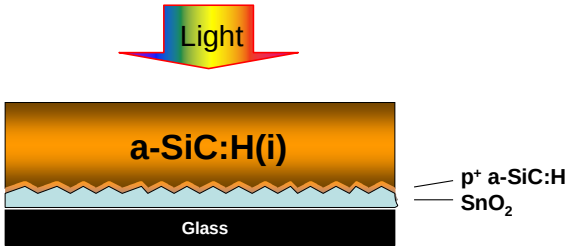

Figure 4 Configuration of a-SiC photoelectrodes.

The typical current density vs. potential curve of the a-SiC photoelectrode is shown in Figure 5(a) [12,13]. The thickness of the intrinsic a-SiC:H layer tested was about 200 nm. The measurement was performed in a pH2 electrolyte in a 3-electrode setup, illuminated with a light intensity conforming to AM1.5G spectrum. The reference electrode used was either SCE (saturated camel electrode) or Ag/Ag/Cl and the counter electrode was Pt. The onset potential for photocurrent generation is about -0.5 V (vs SCE). Figure 5(b) shows variation of the flatband potential (V_{fb}) of the a-SiC photoelectrode with the pH of the electrolyte, where V_{fb} was measured by the illuminated open-circuit potential (IOCP) method. At pH2, the V_{fb} = +0.256 V (vs. Ag/AgCl). With respect to the hydrogen and oxygen redox potentials, it is seen that the pH dependence of V_{fb} roughly follows the Nernst relation [14], with a 59 mV shift per pH unit. It is important to note that the Fermi level of a-SiC is located between HER and OER at all pH values. As a consequence, an external bias is required to split water.

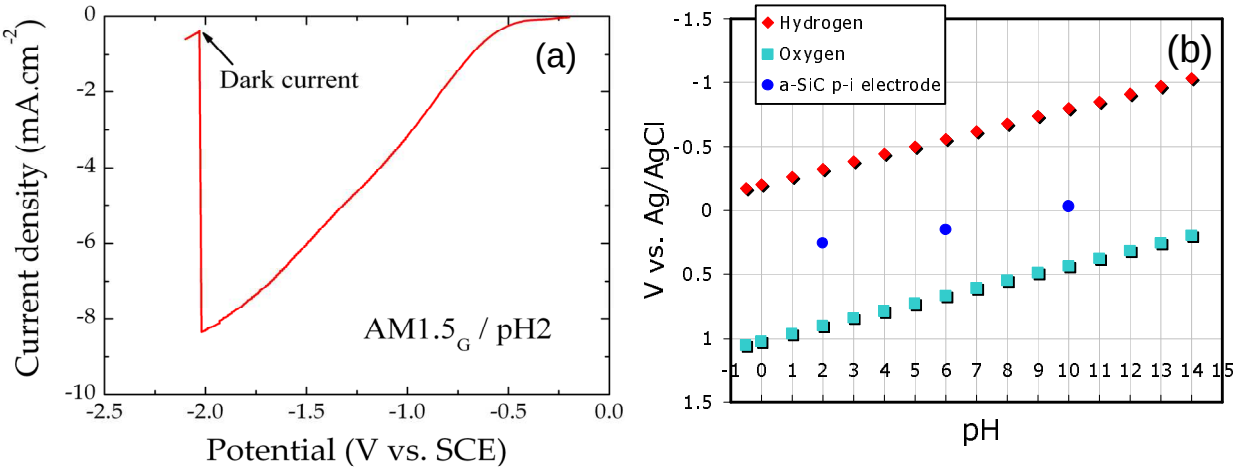

Figure 5 (a) Current density vs. potential. (b) V_{fb} vs. pH.

Based on the measured flatband voltage and the photovoltage data, the energy band diagram for the a-SiC(p)/a-SiC(i)/Electrolyte system under illumination and flatband condition is shown in Figure 6. It can be clearly seen that the hydrogen evolution reaction is unrestricted at the surface of the a-SiC:H photoelectrode, since the photogenerated electrons are of energy which is higher than the redox potential of H^+/H_2. On the other hand, the quasi-Fermi energy level of photogenerated holes, E_{fp} is higher than the H_2O/O_2 redox potential (i.e. by about 0.5 V), which prevents the reaction from occurring at the counter electrode (Pt). Thus, to promote oxygen evolution, an external bias is needed, which is in agreement with the experimental observation.

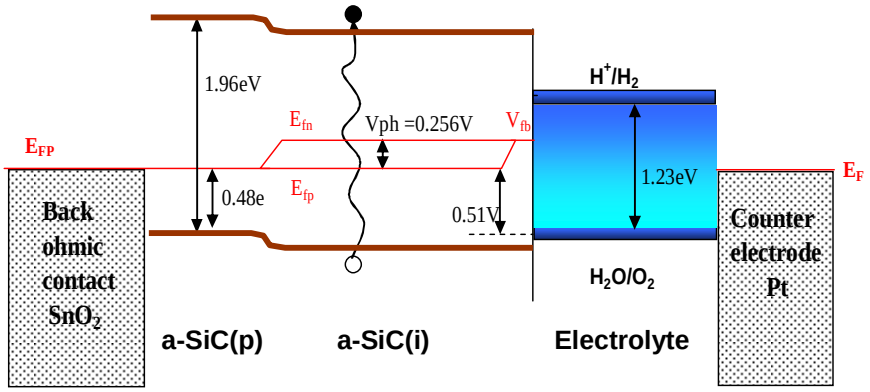

Figure 6 The schematic energy diagram for the a-SiC(p)/a-SiC(i)/Electrolyte system under illumination and flatband condition.

2.4 Fabrication of hybrid PV/a-SiC devices

We have shown in the previous section that an external bias is needed to split water in a stand-alone configuration due to the non-ideal alignment of the valence band edge of the a-SiC photoelectrode with respect to the H_2O/O_2 redox potential. To overcome this problem, we fabricated a hybrid PV/a-SiC device in which the a-SiC photoelectrode was monolithically integrated with an a-Si tandem solar cell, which provided the extra voltage required for practical water splitting. In this section, the main properties of the hybrid device will be described.

2.4.1 Hybrid devices with a-Si tandem solar cell as driver

2.4.1.1 Configuration

Figure 7(a) shows the schematic diagram of the hybrid PV/a-SiC device. The a-SiC photoelectrode was typically 100 nm thick. Both the a-Si tandem solar cell and the a-SiC photoelectrode were fabricated by the PECVD technique in a same multi-chamber PECVD cluster tool system.

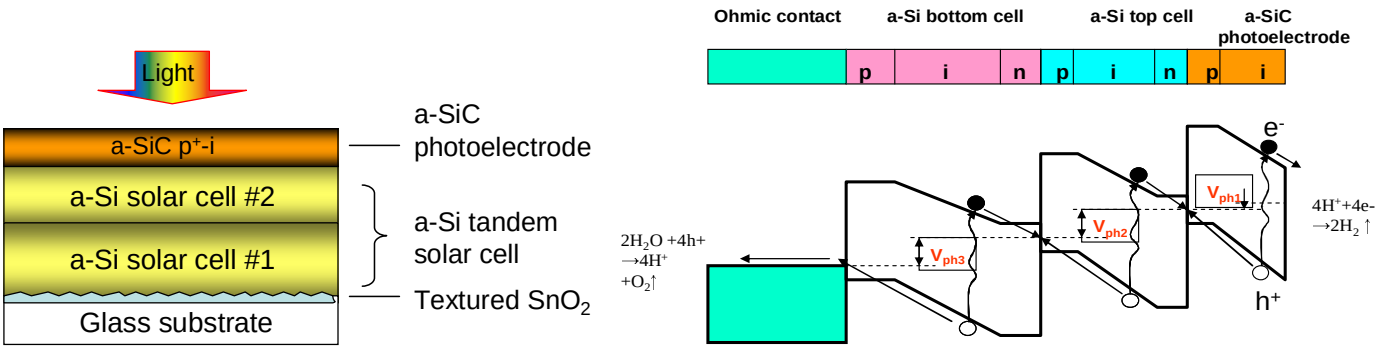

(a) (b)

Figure 7 (a) Schematic diagram of the hybrid PV/PEC cell containing an a-Si p-i-n/p-i-n tandem solar cell and a-SiC p-i photoelectrode. (b) The energy band diagram of the hybrid device.

The a-Si solar cell, which serves as the driving engine for hydrogen production, is the backbone of the entire hybrid PV/PEC cell architecture design. The a-Si tandem solar cell consists of two a-Si single junction devices of p-i-n/p-i-n configuration. Figure 8(a) shows the light J-V curve of a state-of-the-art a-Si single junction solar cell

with a conversion efficiency ~10%. The typical performance of an a-Si tandem solar cell is shown in Figure 8(b). For better current matching, the thickness of the top cell was typically kept as ~60 nm whereas the bottom cell was ~400 nm thick. It is seen that the tandem device exhibits an efficiency ~9% and the Voc ~1.7 V, which should provide sufficient voltage for the hybrid device to split water.

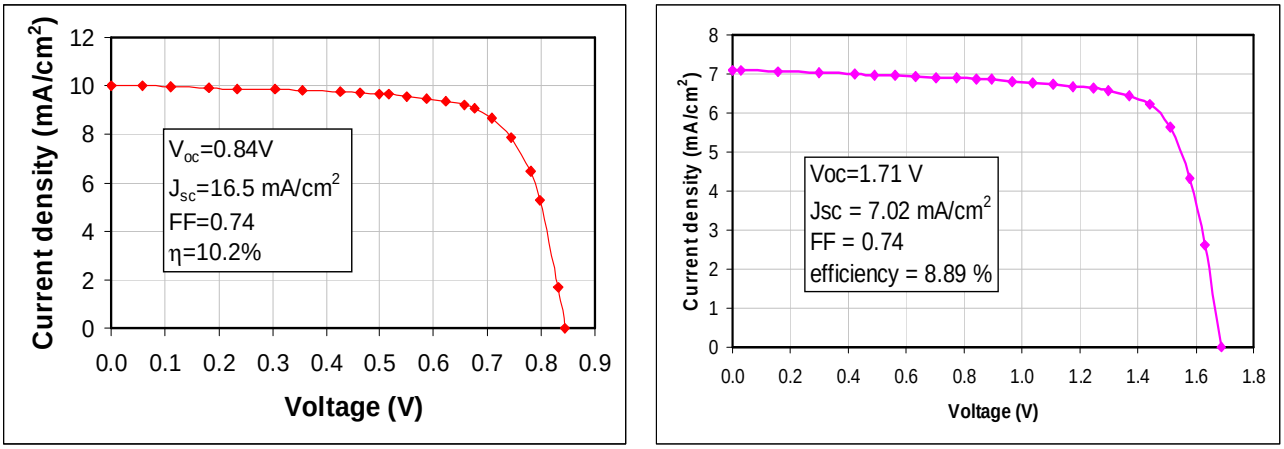

(a) (b)

Figure 8 Light J-V curves of (a) the a-Si single junction solar cell and (b) the a-Si tandem solar cell.

The hybrid device consisting of the a-Si tandem solar cell and a-SiC photoelectrode is actually a triple junction semiconductor device of different bandgaps. The performance of such a multi-junction device relies critically on the current matching among three cells which is a function of the bandgap and thickness of each layer. To achieve good current matching, we fixed the bandgap of each constituent (i.e. a-Si:H and a-SiC:H), and altered their thicknesses. To evaluate the performance of the actual hybrid device, a thin transparent indium tin oxide (ITO) layer was deposited on the top surface of the a-SiC cell. Comparison of the J-V curves of two solid-state hybrid devices is shown in Figure 9.

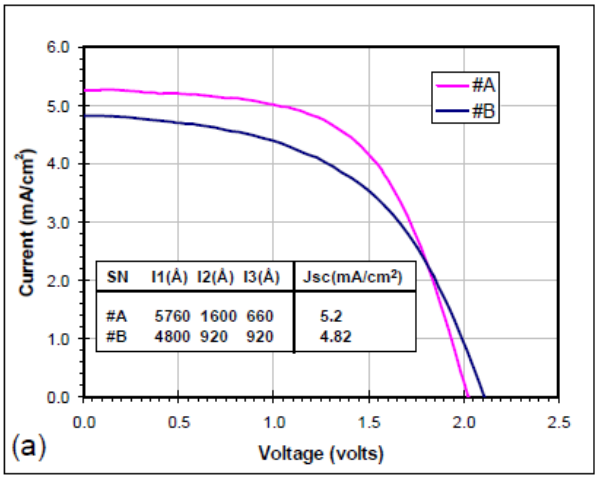

Figure 9 Light J-V curves of two hybrid devices with varying intrinsic layer thicknesses.

After optimization of the thicknesses of the intrinsic layers, a short circuit photocurrent density of ~5.2 mA/cm^2 was achieved (sample #A). At 1.5V (300 mV overpotential for water splitting), the photocurrent reached ~4.1 mA/cm^2.

2.4.1.2 PEC performance

As seen in Figure 7(b), the hole quasi-Fermi level is lowered with addition of the a-Si tandem cell. This is confirmed by the downside shift in the flatband potential of the hybrid device (see Figure 10 below). The

flatband voltage of three hybrid PV/a-SiC devices was determined by the IOCP method, as summarized in Table 1 [15].

Table 1 The flatband potential for an a-SiC photoelectrode and three hybrid PV/PEC devices.

pH	a-SiC	#A	#B	#C	Increase by
2	0.26	1.88	1.76	1.85	1.57
6	0.15	1.69	1.67	1.67	1.53
10	-0.03	1.46	1.46	1.46	1.49

Figure 10 plots the V_{fb} as a function of pH value for both the a-SiC photoelectrode (blue triangles) and three hybrid PV/a-SiC devices (HPE #A, #B, #C). It is seen that, in the case of the hybrid device, the V_{fb} at pH2 shifts from +0.26 V (vs. Ag/AgCl) (for a-SiC photoelectrodes) to +1.88 V, or +0.974 V (vs. Ag/AgCl) below the H_2O/O_2 redox potential, as the pink arrow indicates. This shift in V_{fb} arises from the a-Si tandem solar cell that provides extra 1.6~1.7 V photovoltage as is to be expected. The change in the flatband potential should aid in the generation of photocurrent without the use of external biases.

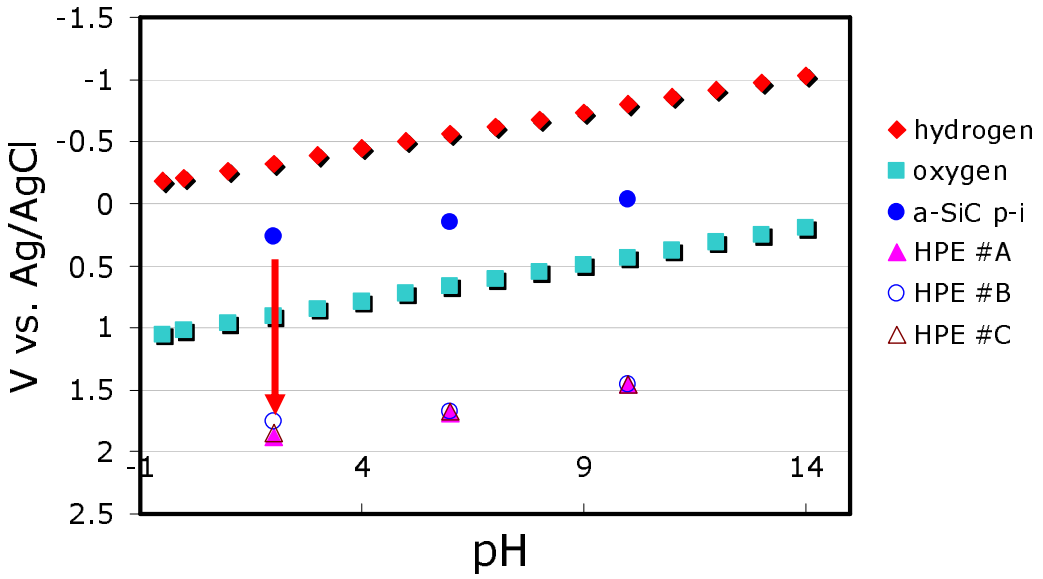

Figure 10 Flatband voltage vs. pH.

Figure 11(a) and (b) show the current vs. potential characteristics for hybrid PV/a-SiC devices fabricated on the textured tin oxide SnO_2 substrate and measured using 3-electrode and 2-electrode setup respectively. In the case of the 2-electrode setup, ruthenium oxide (RuO_2) was used in the measurements. More details about the fabrication of this counter electrode can be found in section 3.3.2. It can be seen from Figure 11(a) that the saturated photocurrent of the hybrid cell reaches -4 mA/cm^2. We notice, however, that the photocurrent measured in the 2-electrode setup shown in Figure 11(b) is quite low, merely about -1 mA/cm^2 at zero bias.

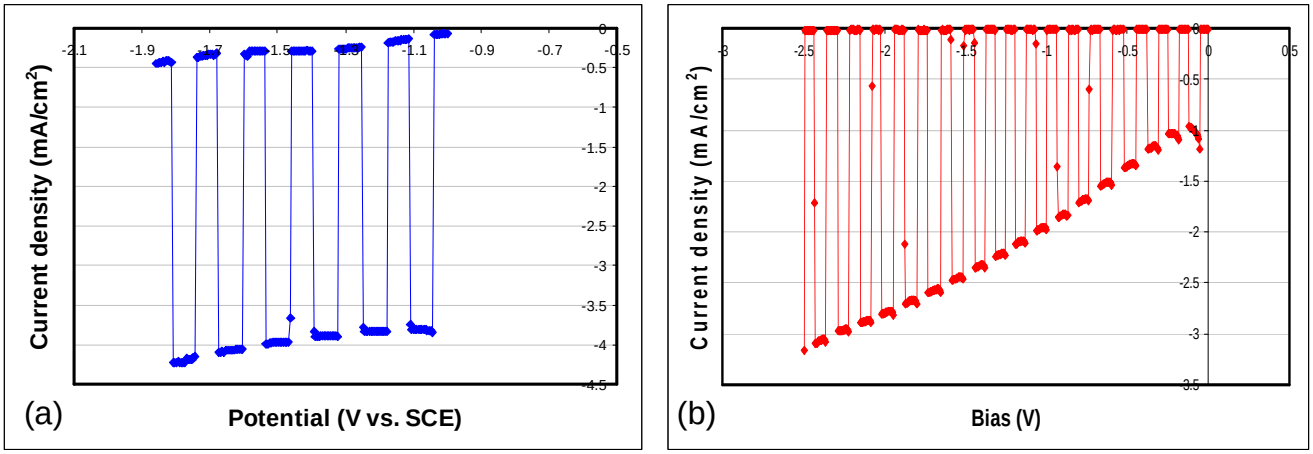

Figure 11 Current vs. potential characteristics measured on a hybrid PV/a-SiC device in (a) 3-electrode and (b) 2-electrode configurations.

Using the hybrid PV/a-SiC device fabricated on SnO_2/glass substrate, we performed a qualitative experiment to demonstrate the evolution of hydrogen bubbles. Figure 12 shows the experimental setup, with the hybrid device short-circuited with the RuO_2 counter electrode. Hydrogen bubbles can be clearly seen on the surface of the hybrid device. The light intensity of a Xenon lamp was adjusted to obtain a close match to the global AM1.5G spectrum.

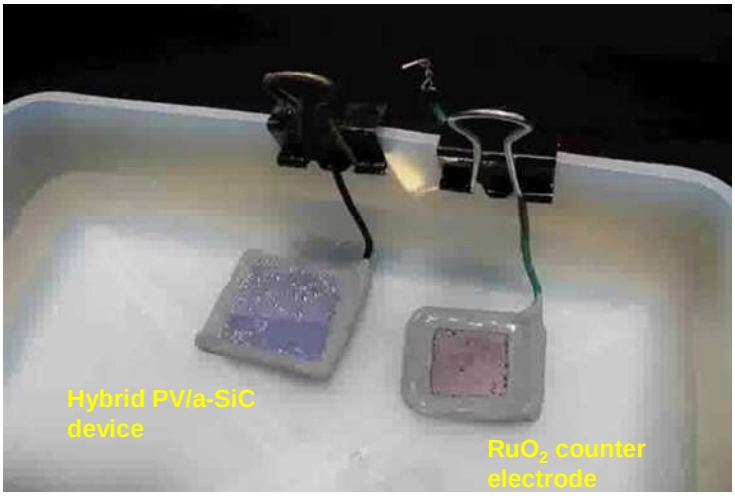

Figure 12 Experimental setup for hydrogen bubble generation on a hybrid device short-circuited with a RuO_2 counter electrode in 0.33M phosphoric acid (H_3PO_4) electrolyte.

2.4.1.3 Improvements of solid-state hybrid PV/a-SiC devices

Since the performance of the PEC device was below expected we reassessed the intrinsic aspects of the structure. In this experiment, a thin n type a-Si and a-SiC layer (~10 nm thick) was added to the top of an a-SiC photoelectrode. To evaluate the performance of the actual hybrid device, a thin transparent indium tin oxide (ITO) layer was deposited on the top surface of the a-SiC cell (see Figure 13(a)).

Figure 13(b) shows two hybrid devices with adding the n-type a-Si:H and a-SiC:H top layer. Another noticeable change by adding a n-type layer is the increase of Voc, i.e., >2.2 V, higher than the hybrid PV/a-SiC device without the n-type layer, which is typically ~2 V. This enhancement in Voc is caused by a higher built-in electric field in the p-i-n configuration (compared with the p-i configuration). The slightly low Jsc in the former is mainly due to absorption loss in a-n+ layer. Care was taken to use a-n+ layer with optimized thickness.

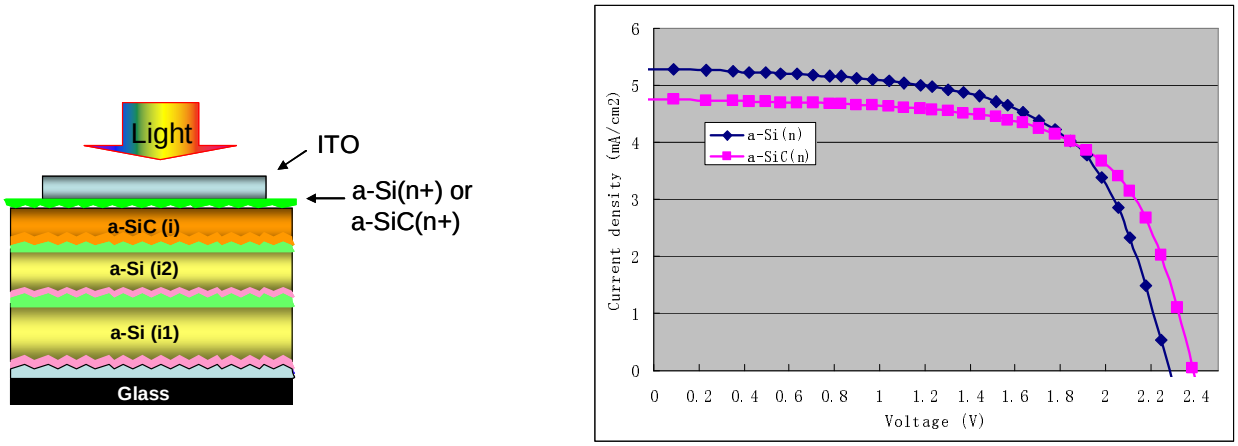

(a) (b)

Figure 13 (a) Schematic diagram of the solid-state hybrid device with the ITO as the top contact. (b) Light J-V curves of two hybrid devices with n-type a-Si:H and a-SiC:H.

With the state-of-the-art a-Si solar cells and improvements in performance of the hybrid device, the efficiency of the solid-state hybrid device increased steadily over the course of the study, from ~5% to ~8%. Table 2 shows improvements of the hybrid device throughout this project.

Table 2 Progress in solid state device performance.

Year	Voc (V)	Jsc (mA/cm^2)	FF	Efficiency (%)
2009	1.98	4.71	0.54	5.04
2012	2.03	5.33	0.53	5.73
2013	2.44	4.75	0.68	7.88

2.4.1.4 Improvement of device performance by surface modification

Besides improving the bulk structure and properties of the device it was evident that much of the loss in the PEC device was due to the reactions occurring at the interface between the semiconductor catalyst material and the electrolyte. In §2.4.1.2, it was shown that the zero-bias photocurrent in the hybrid PV/a-SiC device (see Figure 11(b)) is much smaller than the saturation current measured in 3-electrode (see Figure 11(a)), suggesting that there exist limiting factors that impede extraction of the photogenerated electrons through the a-SiC:H/electrolyte interface for hydrogen evolution.

To understand the origin of this low short circuit photocurrent problem, a solid-state version of the HPE device was fabricated. A thin ITO layer was deposited on the top of the hybrid device (Figure 14(a)). As shown in Figure 14(b), this structure is capable of generating a short-circuit current of ~4.5 mA/cm^2 and an operational current of ~3.3 mA/cm^2 at 300 mV overpotential for water splitting (1.5V). Based on the photocurrent density obtained in PEC configuration (0.3 mA/cm^2), we concluded that our HPE operated at a bias of ~2 V (as shown by the green dashed line if Figure 14(b)). This analysis revealed large overpotentials for a-SiC towards HER.

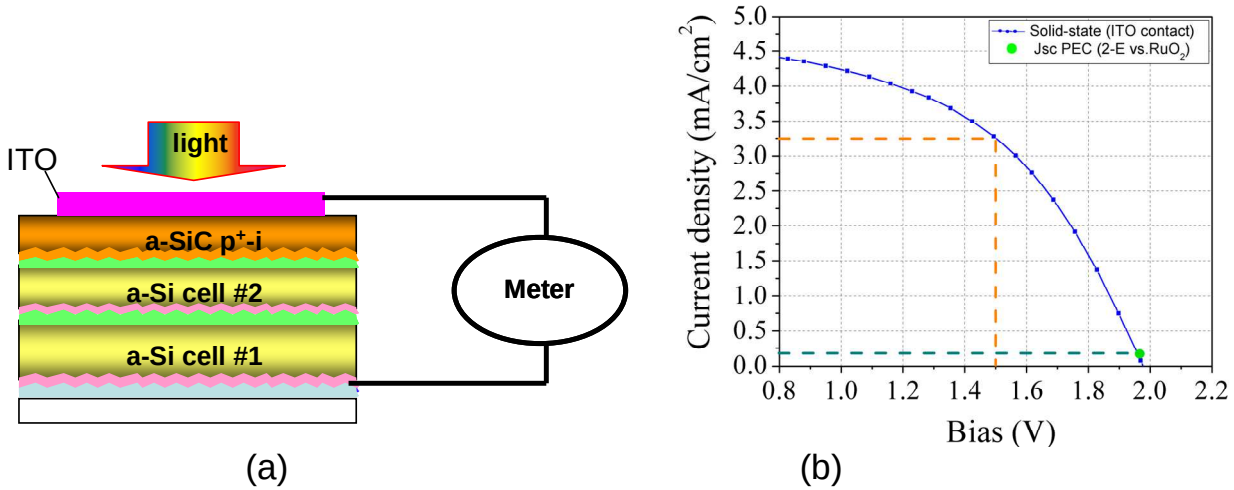

Figure 14 (a) The schematic diagram of the solid-state version of the hybrid device. (b) Current vs. voltage curve of the device.

To overcome the overpotential problem, we performed a comprehensive study on surface modification of the a-SiC:H top layer. Over the course of the study, the following techniques were investigated: HF (hydrofluoric) acid dip, H_2 plasma treatment, passivation by thin a-SiNx , thin C-rich layer or thin nc-SiC, methylation treatment (CH_3 termination) and metal nanoparticles treatment. We are reporting here only the treatments that led to significant results on PEC performance, i.e. HF etch and metal nanoparticles.

A. Effect of native oxide on PEC performance of a-SiC photoelectrodes

It is well known that a thin native oxide layer exists on the surface of silicon carbide [16]. To understand how this oxide layer affects the performance of the hybrid device, we subjected the photoelectrode to an etching process prior to the PEC test. In this experiment, an a-SiC photoelectrode (250 nm thick) was dipped in HF (concentration =24%) for 30 sec, rinsed with de-ionized water and immediately immersed into the electrolyte. Figure 15 shows the variation of the photocurrent measured prior to and after the HF dip prior to PEC test in electrolyte [13].

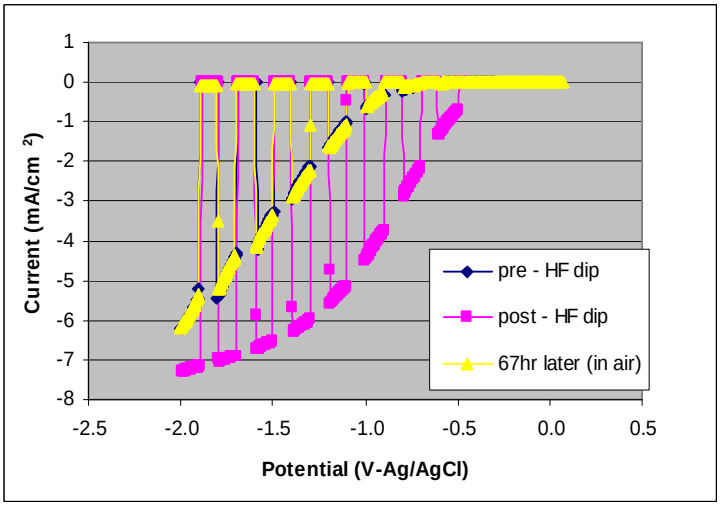

Figure 15 Current vs. potential characteristics measured on an a-SiC photoelectrode before and after a HF etch, as well as a 67-hour long air exposure after the HF dip.

After the 30-sec HF dip, the photocurrent onset potential exhibits a significant anodic shift by about +0.23 V (pink curve). Concurrently, the fill-factor of the curve and the saturation photocurrent density increased. This improvement in PEC characteristics is most likely due to the removal of the thin SiOx layer formed at the surface of the a-SiC photoelectrode. The effect of SiOx was further confirmed by changes in the J-V curve

(yellow one) when the etched a-SiC photoelectrodes was exposed to air for 67 hours, where we see the onset potential reverts back to its original value, likely caused by re-oxidation of the surface.

Further HF etching experiments showed that changes in PEC characteristics depend on both etching concentration and duration. It should be noted that the effect of the surface treatment by HF dip was limited. The treated hybrid devices rarely exhibited a photocurrent density greater than 1 mA/cm^2 at 0V in a 2-electrode setup. Nevertheless, this study shows that the native SiOx layer must be removed prior to any additional surface modification for improving surface energetics of the a-SiC photoelectrodes.

B. Surface treatment by metal nanoparticles

Metal particles have long been used to enhance catalysis facilitating hydrogen evolution [17-19]. However, the use of nanoparticles on top of the PEC device has to be carefully controlled. The right material can indeed improve the reaction dynamics but the particles also shadow the device from the photons necessary to generate the electron-hole pairs that drive the reaction. The metals used for this study can be divided into two groups. One group includes noble metals with high work function such as Pt, Pd or their alloys PtAu (platinum-gold) and PdAu (palladium-gold). These metals are well-known catalysis for hydrogen evolution. The other group includes non-precious metals of low work function such as Ti, Ru and W. Surface treatment by noble metals will be first described, followed then by that of low work function metals.

(i) Surface treatment by noble metals

Gold/palladium islands were deposited on the a-SiC photoelectrodes using a sputter-coating apparatus [20]. Prior to the deposition, the samples were treated using HF dip to remove the native oxide. The best conditions for deposition of nanoparticle was achieved at an argon pressure of 160 mT. The size of PdAu nanoparticles increased from approximately 2 nm to 10 nm as deposition time was varied from 30 sec to 90 sec, as shown in Figure 16.

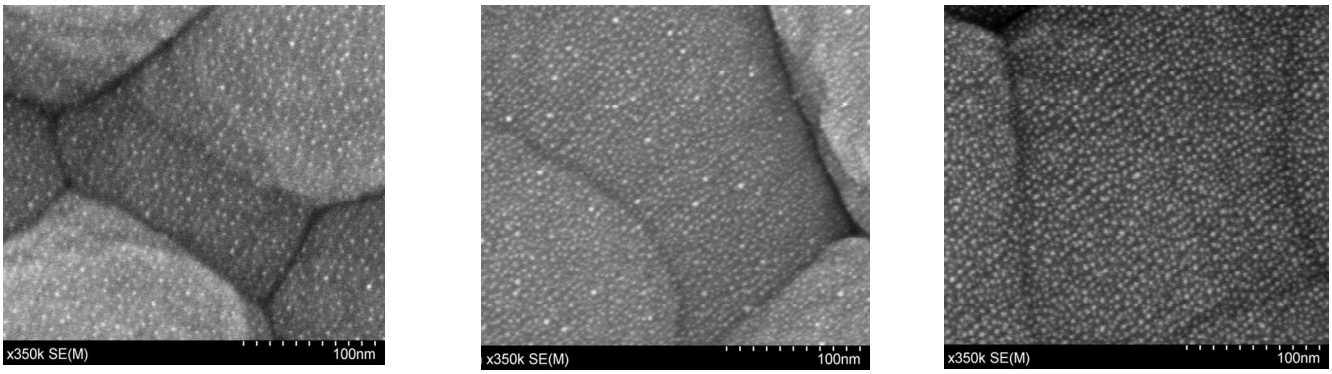

Figure 16 PdAu nanoparticles sputtered at 160 mT argon pressure: (a) 30 sec, (b) 60 sec, (c) 90 sec deposition time.

PEC tests were then performed on the PdAu nanoparticle coated a-SiC photoelectrodes using a RuO_2 as the counter-electrode and the SCE as reference electrode. As seen in Figure 17(a), the onset potential shifted cathodically after PdAu nanoparticle application. A similar behavior was observed with PtAu nanoparticles, as shown in Figure 17(b) [20].

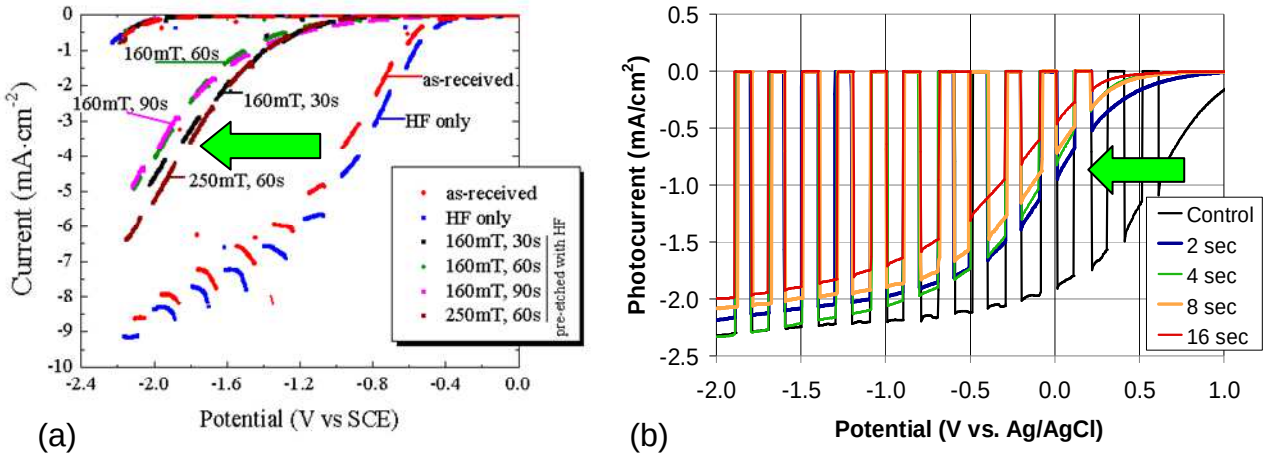

Figure 17 Current density vs. potential characteristics measured prior to and after surface treatment with (a) PdAu nanoparticles; and (b) PtAu nanoparticles.

(ii) Surface treatment by Ru nanoparticles

Figure 18(a) shows the scanning electronic microscopy (SEM) image of a SnO_2:F witness sample with Ru nanoparticles sputtered on the surface [21]. Size of the Ru nanoparticles was less than 5 nm. Transmittance and reflectance of the Ru nanoparticle thin layer are presented in Figure 18(b). It is seen that the transmission is over 80% and reflection is less than 20% in the visible light range. Note that the optical characteristics of the SnO_2:F were subtracted from this measurement.

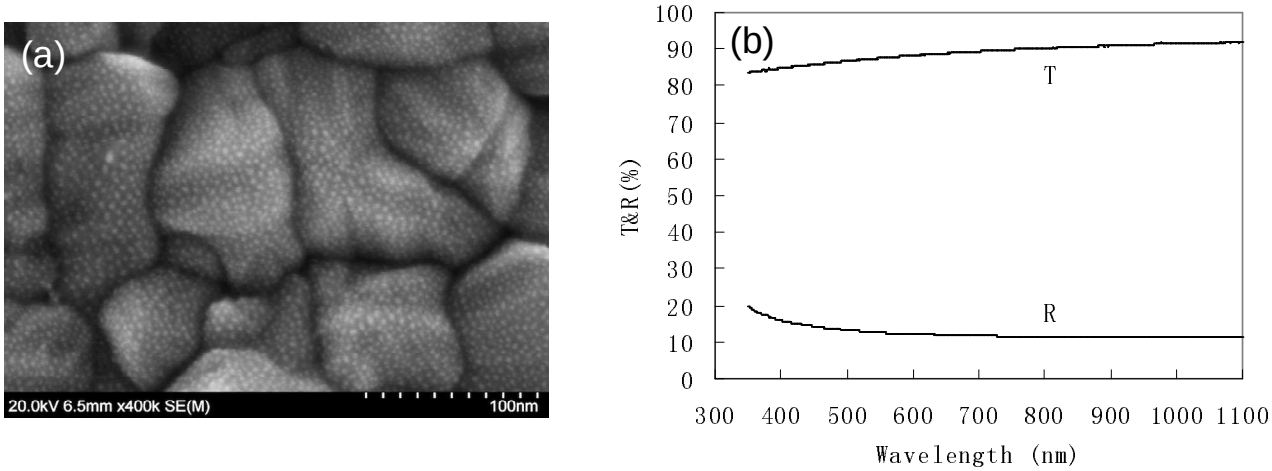

Figure 18 (a) SEM image of SnO2:F coated with Ru nanoparticles similar to those used in surface modification, and (b) transmittance and reflectance of Ru nanoparticles coated on glass (SnO2:F's optical characteristics were subtracted).

Figure 19(a) shows the photocurrent density vs. potential characteristics measured on the hybrid PV/a-SiC devices treated with and without Ru nanoparticles as well as the sample treated by HF etch (5%, 90s). It can be seen that there is a notable anodic shift in the photocurrent vs. voltage curve after the surface treatment with Ru nanoparticles. The photocurrent onset changes from ~1.25 V (vs. SCE) (untreated case) to ~1.69 V (vs. SCE) (after treatment). This is also confirmed by the change of flatband potential, determined by the IOCP technique, as shown in Figure 19(b), which exhibits an anodic shift of +0.4 V. This indicates an improvement in surface energetics, resulting in an increase of the photocurrent at 0V bias (true short-circuit) by an order of magnitude, from ~0.7 mA/cm^2 (untreated case) to 2 mA/cm^2 (after treatment).

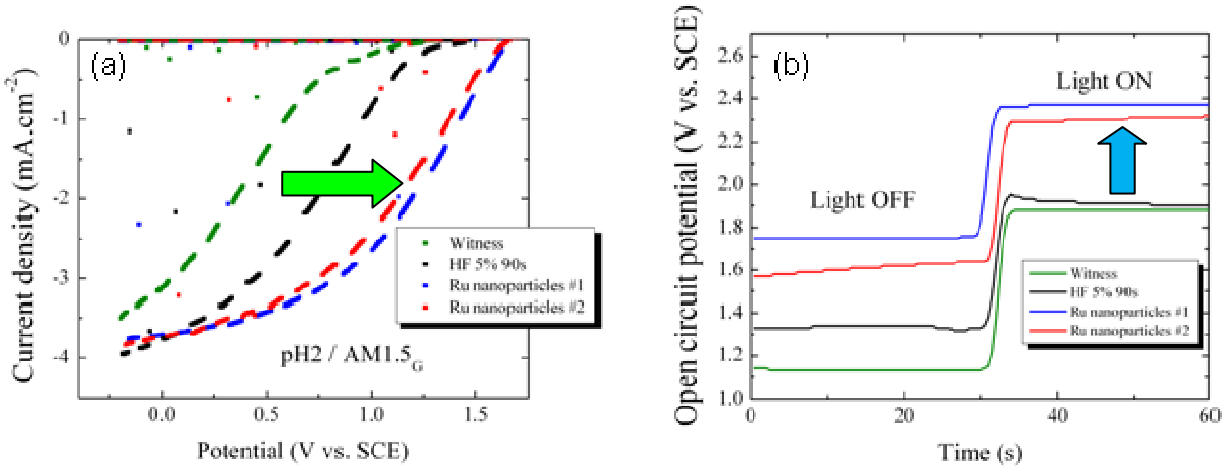

Figure 19 (a) Photocurrent density vs. potential curves prior to and after Ru nanoparticle treatment. (b) Changes in V_{fb}. For comparison, the results by HF etch are also presented.

(iii) Surface treatment by Ti and W nanoparticles

Similar studies on the transmission and reflection characteristics of the material surface were evaluated and deposition conditions were optimized to minimize loss of transmitted light into the device. As with Ru, hybrid devices treated with Ti and W nanoparticles [22] exhibited an anodic shift in the onset potential, as presented in Figure 20(a) and (b).

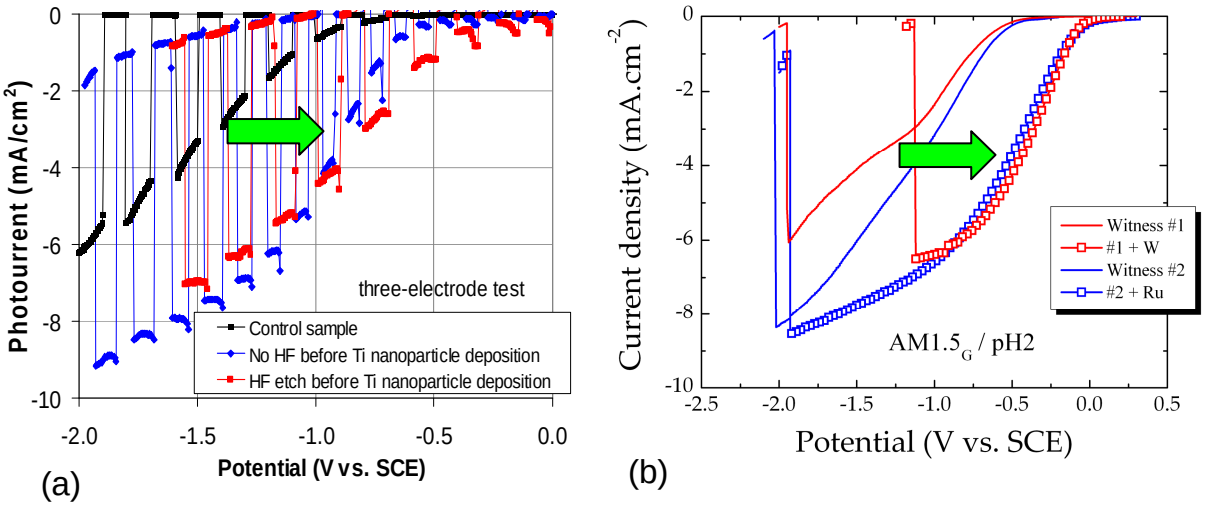

Figure 20 Photocurrent density vs. potential curves prior to and after metal nanoparticle treatments: (a) with Ti nanoparticles; and (b) with W nanoparticles (red curve).

In general, the Ru nanoparticles led to the largest onset potential shift when compared to W and Ti nanoparticles. Table 3 summaries the onset potential shift ΔV (taken in a range of -3 mA/cm^2 on current vs. potential curves).

Table 3 The measured potential shift (ΔV) for Ti, Ru, and W.

Metal	ΔV (V vs SCE)
Ti	0.41
Ru	0.84
W	0.75

The above results show that the surface energetics of the hybrid device is improved by the addition of low work function metals (e.g. Ru, Ti and W) nanoparticles to its surface, as evident by the anodic shift of the onset potential and the flatband voltage. As a result, charge transfer at the a-SiC/electrolyte interface increases resulting in enhanced photocurrent. The cathodic shift exhibited by high work function metal nanoparticles (e.g. Pt, Pd and their alloys) is quite unexpected. One possible cause could be a high Schottky barrier formed at the a-SiC/Pt (or Pd) contact, which could block the photogenerated electron transport through the interface.

Improvements in the solid-state devices, combined with the surface modification with metal nanoparticles led to a noticeable enhancement in performance of the hybrid PV/a-SiC device. Figure 21 shows the current density vs. bias curve for two hybrid device with the n-type a-Si:H and a-SiC:H top layer, measured in 2-electrode setup. The zero-bias photocurrent of 3 mA/cm^2 is achieved in the hybrid device with the a-SiC(n+) top layer, which is significantly higher than that with n-type a-Si top layer. This difference is mainly due to a higher photovoltage in the former (see Figure 13).

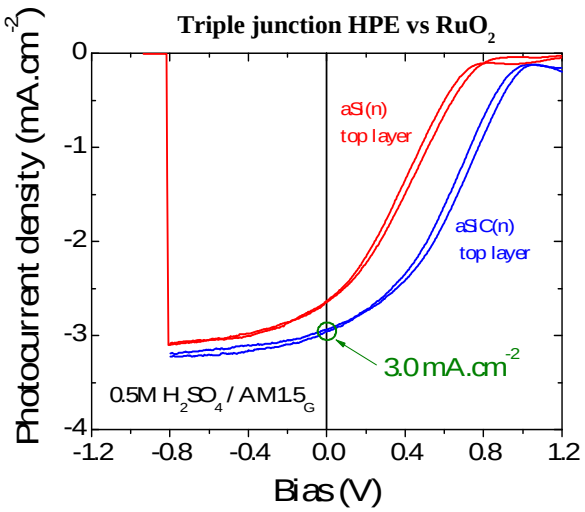

Figure 21 Photocurrent density vs. bias curves of two slightly different types of the hybrid PV/a-SiC devices. Blue curves: with a-SiC(n+) top layer; red curves: with a-Si(n+) top layer, both with surface treatment by Ru nanoparticles.

2.4.1.5 Limitation of the hybrid device with the a-Si tandem engine.

We have shown that, with surface modification by the low work function metal nanoparticles, the hybrid device utilizing the a-Si tandem solar cell can achieve photocurrent density in excess of -3mA/cm^2 and a consequent STH efficiency of ~4% (see Figure 21). The surface modification by metal nanoparticles reduces the surface barrier at a-SiC/electrolyte interface significantly, allowing more effective extraction of photogenerated electrons and charge transfer. In order to further enhance the STH efficiency to reach the DOE's goal, i.e. ≥5%, the performance of the PV driver needs to be improved. A major limiting factor of using the a-Si tandem solar cell resides in the fact that the bandgap of a-Si:H intrinsic layer, 1.7-1.8 eV, is close to that of a-SiC:H (~2 eV), which affects a more effective absorption of photons in the solar spectrum. To fully utilize the "spectrum splitting" effect in the multijunction PV/a-SiC device to increase the photocurrent and hence the STH efficiency, a smaller

bandgap than that of a-Si:H would be desired. To overcome the limit of the a-Si tandem solar cell, a high performance crystalline Si solar cell (Eg=1.12 eV) was introduced to boost the performance of the hybrid PV/a-SiC device. Detailed results are described below.

2.4.2 Hybrid devices with high performance Si solar cell as driver

In this experiment, we fabricated a multijunction PEC stack comprising a crystalline Si PV cell (bottom cell) and an a-Si tandem cell with a n-type a-SiC:H top layer. Figure 24(a) shows the schematic configuration of such hybrid device. An a-Si tandem solar cell was first deposited on the textured SnO_2 (fluorine doped) substrate, comprising a thin n-type a-SiC:H as the top layer). In order not to affect the conductivity of the n layer (~10^{-2} S/cm), we limited the bandgap of the n-type a-SiC:H to 1.85 eV, which was slightly higher than that of a-Si:H (~1.7 eV). Then, the a-Si tandem solar cell was stacked on top of a low bandgap Si solar cell (Eg<1.4 eV). The two components were finally assembled with a mechanical stack fashion, forming a triple junction solar cell of Si p-n/a-Si p-i-n/a-SiC p-i-n (Figure 22(a)).

Prior to testing the PEC device we characterized the solid-state device of same configuration. The quantum efficiency (QE) of the initial Si cell (red curve) and the one filtered by the a-Si/a-SiC tandem device (blue curve) are shown in Figure 22(b). For comparison, the transmission spectrum through the tandem cell is also presented (pink curve). It can be seen that the majority of the light absorption by the a-Si tandem solar cell occurs under 680 nm, which is in agreement with the bandgap of a-Si:H and a-SiC:H (1.75~1.85 eV). Beyond this wavelength range, absorption in the tandem device decreases rapidly. The transmitted photons are then absorbed by the low bandgap Si cell.

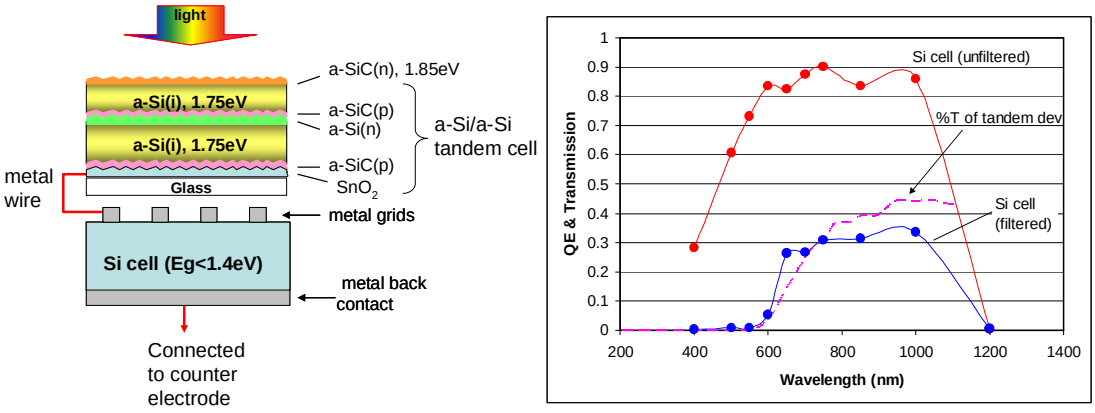

(a) (b)

Figure 22 (a) Schematic diagram of the high performance hybrid device in a mechanical stack configuration. (b) The QE curves of the stack: red curve - initial QE of the Si cell; blue curve - filtered by the a-Si/a-Si tandem device (with n-type a-SiC:H on top); pink curve – the transmission spectrum through the tandem cell.

Table 4 summarizes the performance of the Si/a-Si/a-SiC stack measured in solid-state. In addition, the performances of the individual cell (including a-Si tandem cell and the filtered Si cell) in each stack are also shown. The Jsc was obtained by integrating the QE spectrum curve (see Figure 22(b)), whereas V_{op} and J_{op} are the voltage and photocurrent density at the maximum power point, estimated from the relations $\sqrt{FF} * V_{oc}$ and $\sqrt{FF} * J_{sc}$, respectively.

Table 4 Performance of the Si/a-Si/a-SiC stack measured in solid-state.

Cell type	Voc (V)	Jsc (mA/cm^2)	FF	Vop (V)	Jop (mA/cm^2)
a-Si tandem cell	1.66	6.91	0.64		
Filtered Si-cell	0.56	12.4	0.61		
Entire stack	2.22	6.91	0.61	1.74	5.4

The device was then sent to HNEI for surface treatment and PEC characterization. Prior to the deposition of Ru nanoparticles, the native SiO_2 was first removed in 5% HF for 90 sec. A photograph of the hybrid PV/a-SiC device tested at HNEI is presented in Figure 23(a). The current vs. voltage characteristic of this device (shown in Figure 23(b) was then measured in 2-electrode configuration using a RuO_2 counter electrode. The electrolyte was 0.5M H_2SO_4. The illumination density was calibrated to AM1.5G using a spectroradiometer. It can be seen that a noticeable anodic shift in potential onset, 0.6~0.7 V, occurred with surface treatment. This is also confirmed by the change in the flatband potential (i.e. by 0.6V, not shown here). At zero bias, the photocurrent reached 4.91 mA/cm^2, which is equivalent to a STH efficiency of ~6.1%, the highest ever value achieved in this program.

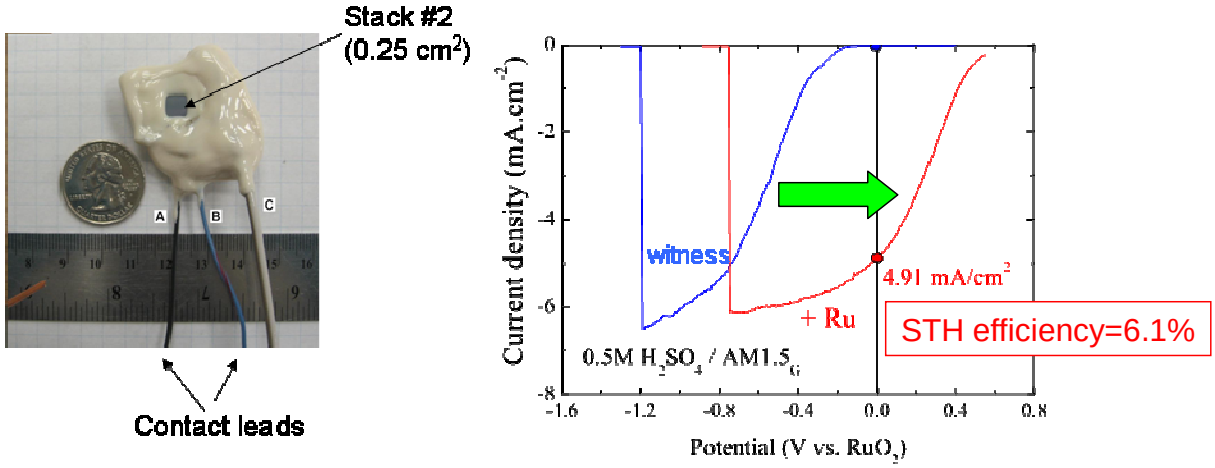

(a) (b)

Figure 23 (a) Image of the new hybrid PV/a-SiC device constructed in mechanical stack, and (b) Current density vs. potential measured in 2-electrode setup. The arrow indicates the anodic shift in onset potential.

It should be noted that significant optical losses are expected at multiple interfaces in such a mechanical stack including the a-Si:H/glass, glass/air, air/Si cell, etc. Higher performances should be expected in a monolithically integrated hybrid device, eliminating reflection losses at these interfaces. In addition, it can be seen from Table 4 that the component limiting the stack performance is the a-Si tandem cell. Further improvements are expected by optimizing current matching (i.e. via altering energy bandgap and thickness of the constituent cells) in the monolithic integrated hybrid device.

2.4.3 Durability of hybrid PV/a-SiC devices

With improved surface energetics and PEC performance, the hybrid device should be able to sustain a higher current bias. We performed the durability test on hybrid devices with a higher current bias, i.e. 3~4 mA/cm^2 (which was close to the working current density required to achieve the STH efficiency of 5%). The hybrid device used in the experiment was the top part of the high-performance PV/a-SiC PEC devices, which is of a-Si/a-SiC tandem configuration (see Figure 22(a)).

Prior to the durability test, tungsten (rather than Ru) nanoparticles were deposited by sputtering technique in MVSystems' cluster tool. During the course of the durability test, the photocurrent of the hybrid device was measured on a daily basis. The Pt counter electrode was used throughout the test. The electrolyte was 0.25 M H_2SO_4. An ELH tungsten lamp was used as the light source with its intensity calibrated by a standard PV cell (Hamamatsu cell) to match the AM1.5G spectrum. Since the ELH lamp is of limited lifetime, typically, 50-72 hours, we had to change the lamp from time to time. To avoid any variation in light intensity arising from different lamps, the lamp intensity was determined and calibrated by the photocurrent of a monocrystalline Si solar cell each time a new lamp was installed. A water filter was inserted between the ELH lamp and the sample to suppress the infrared component and avoid possible rising of the sample temperature during the test. To maintain a necessary photocurrent through the device, an external bias between 1.3 V and 1.5 V was applied throughout the test.

Figure 24 shows the photocurrent density as a function of the testing time over a period of 790 hours. The initial photocurrent was measured as 4.7 mA/cm^2 under a voltage bias of 1.3 V. It quickly degreased to ~3.5 mA/cm^2 after the first 14 hours. Multiple reasons could cause this initial degradation such as the light-induced degradation (Staebler-Wronski effect). After this initial drop, the photocurrent becomes stabilized. Hydrogen evolution was observed throughout the entire test. No increase in dark current occurred (shown by the blue solid squares). There are a few moments during the test when the photocurrent showed a noticeable decrease (as indicated by the arrow), which were mainly due to artifacts, such as issues with the water filter or broken lamps.

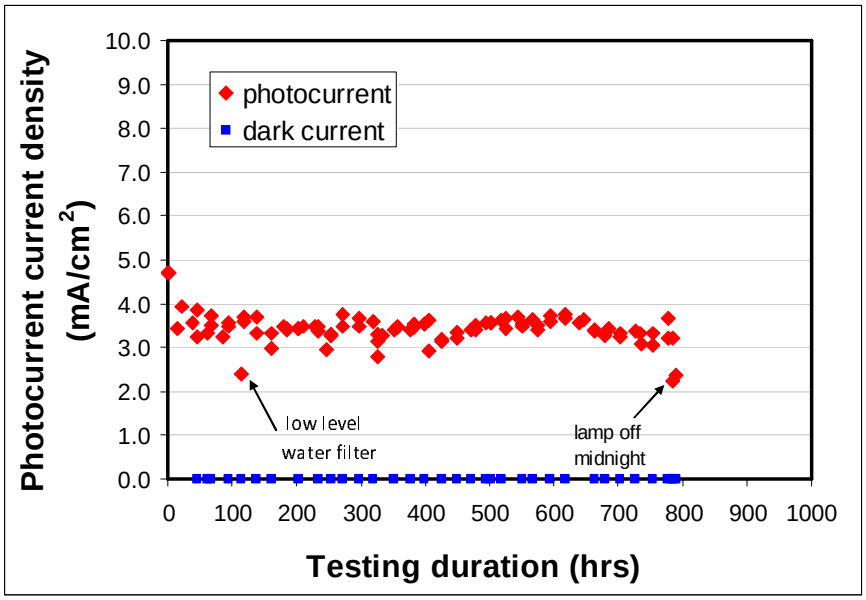

Figure 24 Photocurrent vs. testing time.

We noticed that the prolonged dark current conditions (for instance, broken lamp overnight or weekend) had an important effect on the lifetime of the device, as a non illuminated device reverts to a high resistance state. Since the DC voltage bias was still applied to the device, a high electric field developed across the device (mainly over the high resistive space charge region), damaging the device. This situation happened at the final stage of the test when the photocurrent dropped to ~2 mA/cm^2 after 790 hours, as show in Figure **24**. The test was then stopped (although hydrogen gas was still being evolved). Note that for dark condition less than 5~6 hours, the device usually recovered. It is worth mentioning that complete hybrid devices should be more stable, as no bias would be applied under dark condition.

Changes in surface morphology of the device during the course of the experiment are shown in Figure 25. It is seen that after the ~800 hour test, the device appears mostly unchanged (e.g. no color change or material peeling off), except a few local spots. It was noted that after 325 hours, several power outages occurred in the lab which caused voltage spikes once the power was restored. The occurrence of the power outages coincide with the appearance of pinholes across the sample (see Figure 25(b)). Interestingly, these local defects appeared not to affect the PEC performances of the device, as the photocurrent slightly decreased below 3 mA/cm^2 temporarily and then quickly recovered to ~3.5 mA/cm^2 (see variation of photocurrent around 325 hours in Figure 24).

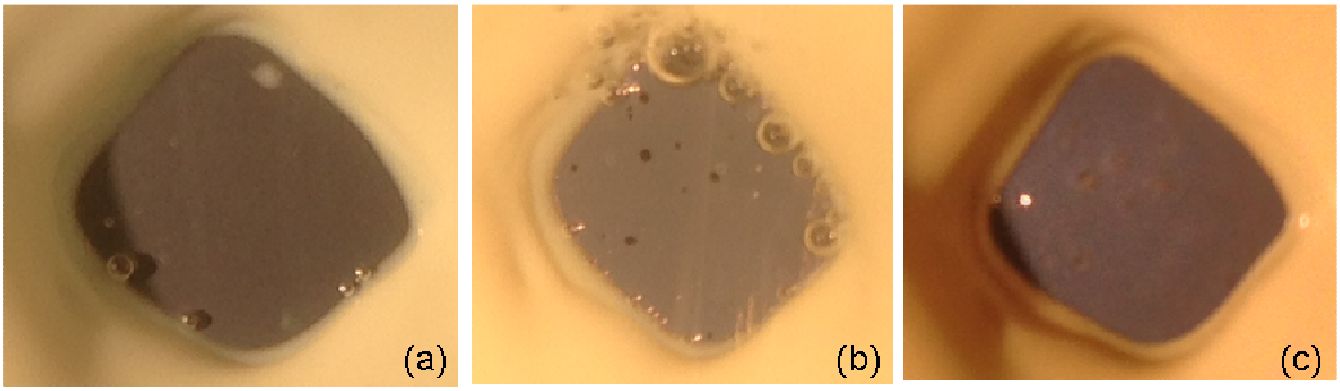

Figure 25 Photographs of the hybrid device under test: (a) prior to the test; (b) after 325 hours; (c) after the 789-hour test. Note both (a) and (b) were taken in the electrolyte.

In summary, the above results show that hybrid devices covered with W nanoparticles exhibits very good durability of up to ~800 hours (so far tested), when operating under a photocurrent density of 3-4 mA/cm^2. This indicates that a-SiC:H film is quite durable when used as a photoelectrode material for solar-powered water splitting.

3. Copper Chalcopyrite Compounds

3.1 Motivations and main technology barriers

The I-III-VI_2 alloyed semiconductor class, championed in the photovoltaic scientific field by $Cu(In_xGa_{1-x})Se_2$ (often abbreviated "CIGS"), incorporates a wide range of materials that are useful in solar energy conversion. Within this material class, bandgaps between 1.0eV and 2.43eV can be obtained by varying the alloy ratios in each elemental group [23]. Of most interest for PEC water-splitting is the higher-bandgap members of this class, such as $CuGaSe_2$ with a bandgap of 1.65eV which has served generally as the baseline material for this application. The variable bandgap of the copper chalcopyrite compounds has been studied extensively, most often for PV applications, making this material class particularly attractive for the development of PEC materials and systems by utilizing the very rich existing knowledge base [23,24]. The very high $Cu(InGa)Se_2$ PV conversion efficiency of 20.3% (Nov. 2011) with lower-bandgap material is made possible by the strong optical absorption due to a direct bandgap, exceptional carrier transport properties, and compositional tunability enabling highly beneficial bandgap grading [25]. These traits are just as important for a PEC device and are, for the most part, maintained in the higher-bandgap materials like $CuGaSe_2$. Despite the existing knowledge base, significant work is needed to tune the material properties for PEC applications. It is worth mentioning that any CIGSe-based PEC technologies would rely on existing fabrication techniques already implemented for CIGSe PV technologies, allowing for the rapid deployment of PEC devices when a suitable material is developed. Because materials viable for PEC devices have high bandgaps, much of the visible solar spectrum is not absorbed. This offers the opportunity to harvest the unabsorbed photons with underlying PV cells of smaller bandgaps resulting in multi-junction devices that can more effectively utilize incident light. Multi-junction devices are electrically connected in series, resulting in a summation of voltages to counteract typically insufficient band edge alignment and kinetic overpotentials of the water-splitting reactions. Multi-junction absorbers have been utilized to achieve world record efficiencies in both PV [26] and PEC [27] devices utilizing the III-V material class, and are the optimal configuration in the development of most planar PEC water-splitting devices. This is particularly convenient for alloyed semiconductors like the I-III-VI_2 material class because the ability to engineer the bandgaps by alloy compositions permit tuning to optimize absorption via multi-layers within the same material class.

3.2 Addressing the challenges

The research philosophy in this material class has so far aimed to take an optimized material ($Cu(InGa)Se_2$), proven to have excellent optoelectronic properties in the PV field, and repurpose it for the requirements of water-splitting. The first requirement is a high bandgap of *at least* 1.23eV, and preferably much higher in the 1.6-2.1eV range 28]. By removing indium from optimized PV devices resulting in $CuGaSe_2$, the bandgap is raised to a modest 1.65eV, which can, in an appropriate configuration, be used to split water. $CuGaSe_2$ thus serves as the baseline material for this material class. Its chemical simplicity, ease of fabrication, and close relation to commercial PV $Cu(InGa)Se_2$ has resulted in very robust fabrication of high-quality cells, and performance and durability have proven to be exceptional [29-31].

With the increase of Ga, however, the bandgap is expanded by a rise in the conduction band while the valence band remains misaligned with respect to the oxygen evolution potential. This occurs because the valence band energy is dominated by the Cu-3d to Se-4p orbital bond, which is unaffected by the group-III alloy content (In,Ga) [32]. Furthermore, $CuGaSe_2$ is subjected to the "doping pinning rule", common in highly-doped semiconductors, wherein the Fermi level is pinned at a certain level interrupting the band bending vital to photovoltage production [33]. This doping pinning precludes the formation of a surface inversion layer that is very highly relied upon in $Cu(InGa)Se_2$ PV devices, resulting in a sub-proportional increase in open circuit voltages as bandgaps are raised with an increase in the Ga/(In+Ga) ratio [32,34]. This effect is also evident in PEC devices where $CuGaSe_2$ exhibits much lower photovoltage than would be expected for its bandgap, and therefore requires a very high voltage bias (presumably provided by light-harvesting PV cells) to split water.

Therefore (with the design philosophy of using $CuGaSe_2$ as a baseline material), the largest barrier in the I-III-VI_2 material class is overcoming the excessive voltage requirements originating from the misaligned valence

band edge. Because the valence band energy is dominated by the I-VI bond (Cu-Se in the base case), it is the Cu and/or Se content that must be modified by, for example, replacing some Cu with Ag or Se with S.

3.3 Technical accomplishments

3.3.1 Chalcopyrite material synthesis, optoelectronic properties and PEC characteristics

Copper chalcopyrite materials used in this research program were fabricated using co-evaporation techniques using a 2-stage process where Cu/Ga/Se and Ga/Se elements were deposited in two successive sequences (Figure 26(a)). This process was chosen to fabricate $CuGaSe_2$ film having a copper-graded film with copper-poor surface in order to prevent the formation of $CuSe_2$, a material notoriously known for lowering efficiency of chalcopyrite-based devices. With deposition temperatures relatively low (<450^{o}C), copper diffusion is limited, leading to the formation of a bilayered-like film, with a copper poor (Ga>Cu) bottom layer and a copper-deficient (Ga>>Cu) surface. The effect of this process on the $CuGaSe_2$ characteristics can be seen directly on the Tauc plot (Figure 26(b)), showing basically two absorption thresholds in the $CuGaSe_2$ films.

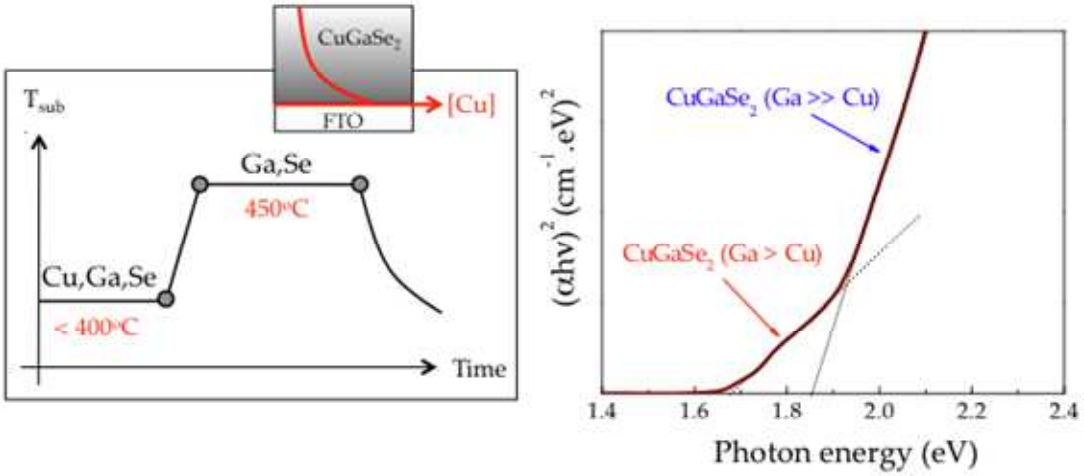

(a) (b)

Figure 26 (a) Temperature profiles used in the $CuGaSe_2$ 2-stage deposition process. (b) Tauc plot of $CuGaSe_2$ thin films.

The basic PEC characteristics of $CuGaSe_2$ photocathode are presented in Figure 27. Incident photon-to-electron efficiency measurements (quantum efficiency) indicate that this material converts a significant part of absorbed photon in the visible, up to 60% in the 450-650nm range under saturation conditions (-0.6 V_{RHE}) in 0.5M H_2SO_4. Integrating this IPCE curve over AM1.5G leads to a photocurrent density of 14 mA/cm^2. As a consequence, $CuGaSe_2$ has the potential to produce hydrogen with STH efficiency 17%, assuming such current density can be achieved without external bias. Unfortunately, $CuGaSe_2$ falls short in terms of band alignment for water splitting and photo-voltage produced. As shown in Figure 27 (top, right) and Figure 27 (bottom, left), the Fermi level of $CuGaSe_2$ sits only 275 mV below H+/H2 level when immersed in 0.5M H_2SO_4 and $CuGaSe_2$ generates only 100 mV of photo-voltage. Therefore, overpotentials for water reduction with this material are rather large, and a potential of at least -0.2V_{RHE} is required to produce hydrogen.

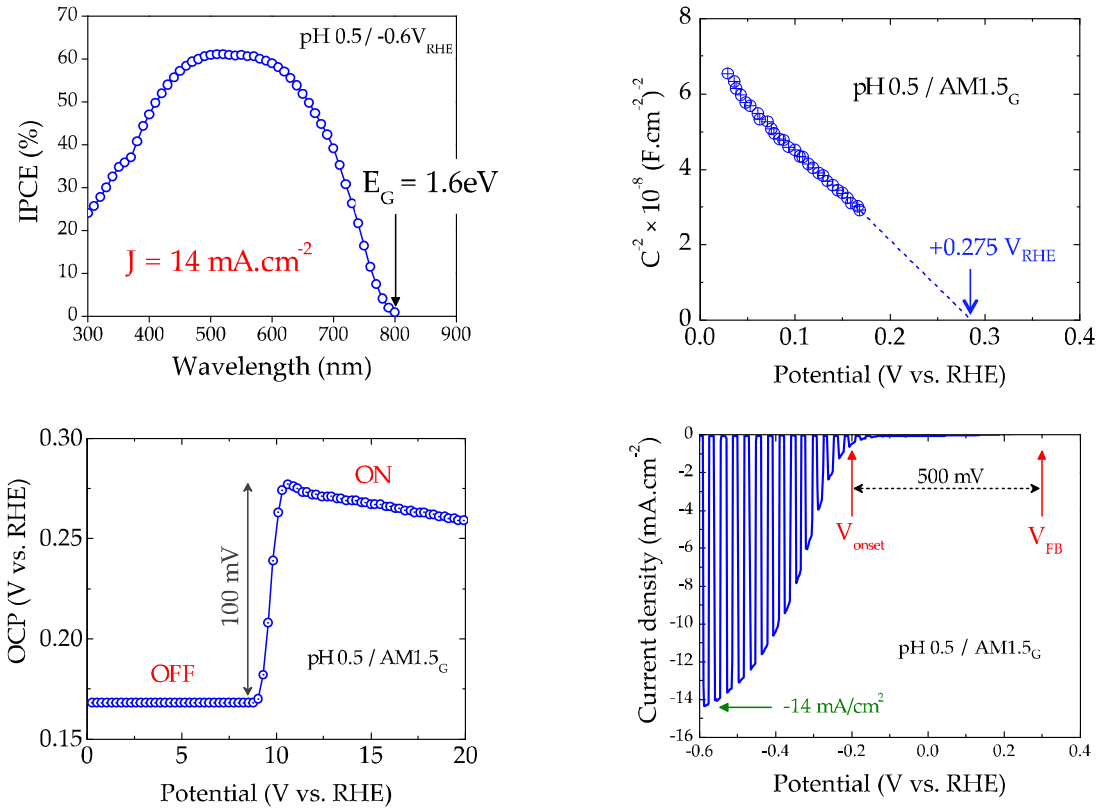

Figure 27 (Top left) Incident photon-to-current efficiency (top right) Mott-Schottky plot (bottom left) open circuit potential and (bottom right) linear sweep voltammetry measured on $CuGaSe_2$ photocathode in 0.5M H_2SO_4 electrolyte under simulated AM1.5G illumination.

Fortunately, majority of electrons photo-generated a potential more cathodically than -0.2 V_{RHE} participating to the hydrogen evolution reaction. As presented in Figure 28(a), un-catalyzed $CuGaSe_2$ photocathodes have a Faradaic efficiency (ratio of electrical charges over amount of gas evolved) greater than 85%. The stability of $CuGaSe_2$ was also evaluated by mean of chronoamperometry measured at AM1.5G in 0.5M H_2SO_4 under a constant potential (-0.45 V_{RHE}). Under these tests conditions, a steady photocurrent density 4 mA/cm^2 was measured for 400 hours. Passed this period, parts of the $CuGaSe_2$ photocathode flaked of the substrate, most likely via corrosion mechanisms at the substrate/$CuGaSe_2$ interface rather than dissolution of the $CuGaSe_2$ thin film itself. Such failure mechanism could be explained by the presence of pinholes in the $CuGaSe_2$ film.

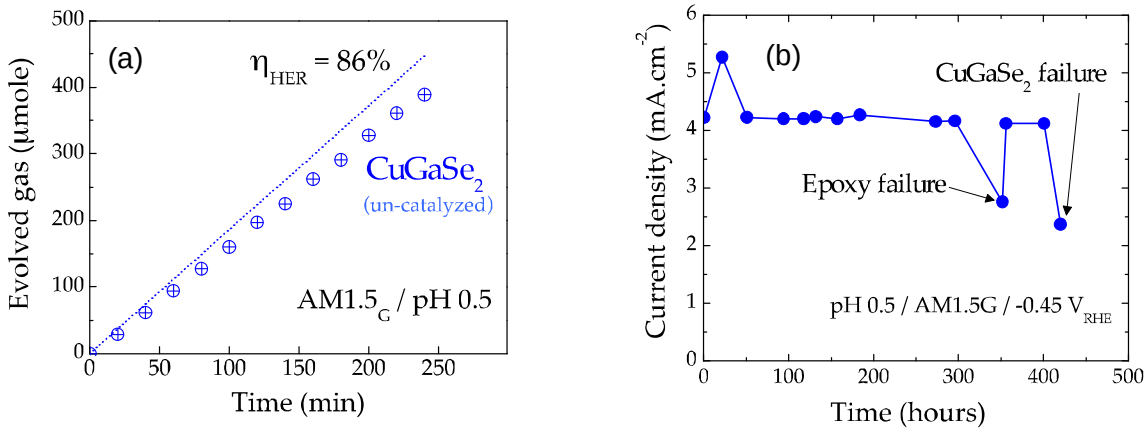

Figure 28 (a) Amount of hydrogen produced as function of time and (b) chronoamperometry (current density vs. time) measured on $CuGaSe_2$ photocathode in 0.5M H_2SO_4 under simulated AM1.5G illumination.

3.3.2 Development of a passive OER anode for STH efficiency benchmarking

Several efficiency definitions are used to report the efficiency of semiconductor materials. However, the solar-to-hydrogen (STH) efficiency is only method that can be used to compare PEC systems an impartial and meaningful way. As its name suggests, photons are the only source of energy and neither electrical nor chemical biases can be used in this measurement. The measurement must be done in a 2-electrode fashion using existing components that are assembled to form a standalone device. Since most of materials studied by the PEC community are photoanodes (WO_3, TiO_2, Fe_2O_3, $CuWO_4$…etc.), little effort has been made to develop efficient passive anode materials in order to report efficiency of photocathodes. As a consequence, many (including our team) have used Pt for oxygen evolution reaction (OER) in the past to report benchmark STH efficiency of photocathode materials. As shown in Figure 29(a), overpotentials for OER at a current density of 10 mA/cm^2 with Pt are quite large, c.a. 0.75 V. Efforts were made during this research program to develop RuO_2 counter electrodes in order to lower overpotentials and improve the STH of our photocathodes. Our team selected ruthenium oxide, a well-known catalyst for OER. Our RuO_2 thin films were deposited by reactive sputtering process using a Ru target. The low temperatures used (<200°C) allowed to deposit this material on any kind of substrate (glass, foil, polymer), while maintaining excellent catalytic activity. As shown in Figure 29(a), the overpotential for OER obtained with RuO_2 at 10 mA/cm^2 is as low as 0.25 V, representing a reduction in overpotential of 500 mV when compared to Pt. The Faradaic efficiency of these RuO_2, measured in 0.5 M H_2SO_4 electrolyte at 400 mV overpotentials for OER, was close to 90% (Figure 29(b)).

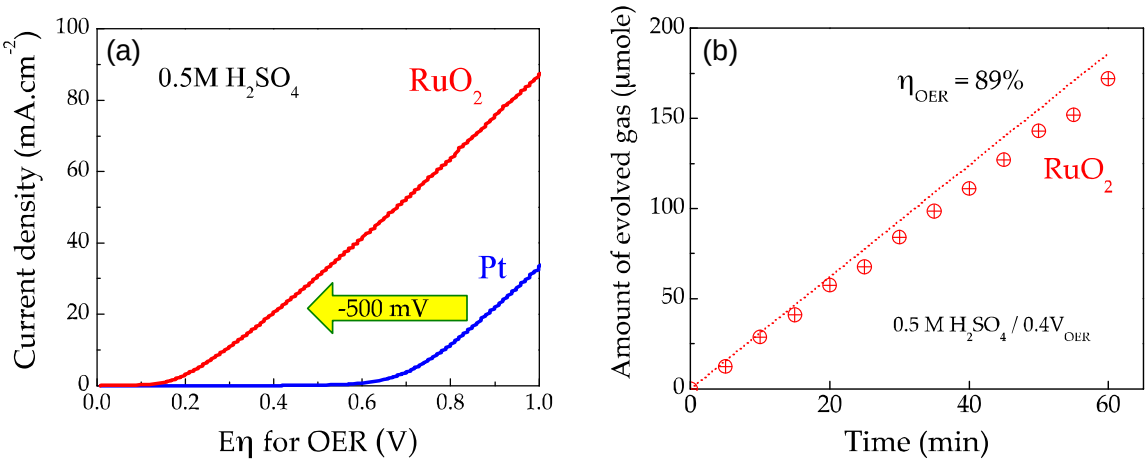

Figure 29 (a) Polarization curves measured in 0.5M H_2SO_4 on RuO_2 and Pt for OER. (b) Amount of oxygen produced as function of time by a RuO_2 thin film at 0.4 V_{OER} in 0.5M H_2SO_4 electrolyte.

At this stage of the program, no copper chalcopyrite materials with bandgaps greater than 1.68 eV were discovered. Therefore, $CuGaSe_2$ could not be integrated as in a stacked HPE configuration, since both $CuGaSe_2$ and amorphous silicon have similar bandgaps. One way to circumvent this issue is to take advantage of the large photocurrent density generated by $CuGaSe_2$ and sacrifice part of the device estate to form a coplanar device. Preliminary studies performed at HNEI were done to identify the optimum relative area between the two components. The LSV characteristic of $CuGaSe_2$ measured in a 2-electrode fashion against RuO_2 and the J-V curve of the a-Si triple junction device (comprising three a-Si single junction solar cells connected in series, whose performance is shown in Figure 8(a)) are plotted on the same graph and normalized to different relative area (Figure 30(a)). As an example, 50% PEC/50% PV relative area would mean that half of the total device area is occupied by the PEC electrode, whereas the other half is used by the PV device. Both LSV and PV characteristics where then plotted with different relative areas, as shown in Figure 30(a). The optimum area ratio was then determined by the maximum photocurrent density achievable by this co-planar system, defined by the intersect of both current-voltage characteristics. We founded that a PEC/PV area ratio of 30% was optimal, operating at 1.6 V and generating a photocurrent density of 3.7 mA.cm^2. Such a device was made using $CuGaSe_2$ and a-Si components and tested under AM1.5G outdoor conditions. It should be noted that the aSi-based triple junction was kept out of the electrolyte. As predicted by the load-line analysis, a photocurrent density of 3.5 mA.cm^2 was achieved, corresponding to a STH benchmark efficiency of 3.7% (η_F=86%).

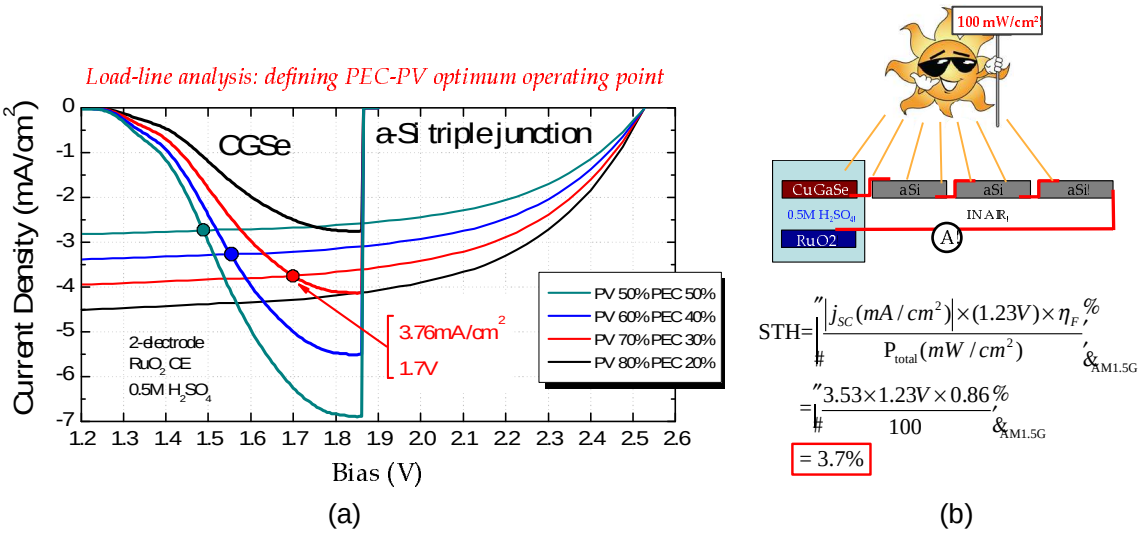

Figure 30 (a) Load-line analysis used to define the optimum relative area between $CuGaSe_2$ PEC and a-Si triple junction solar cell (comprising three a-Si single junction solar cells connected in series) in a coplanar device. (b) Schematic of the coplanar device and calculation of the benchmark STH efficiency obtained with this system.

Achieving 3.7% STH efficiency with $CuGaSe_2$ and a-Si components is an important milestone for this program. It is worth mentioning that this value was not based on the short-circuit photocurrent density only, but takes into account the Faradaic efficiency of un-catalyzed $CuGaSe_2$ (86%). One should also bear in mind that this value was achieved with 4 junctions connected in series in a coplanar fashion. The use of a coplanar system was mandatory since both $CuGaSe_2$ and a-Si have similar bandgap, whereas the number of cells (1 PEC and 3 PV) was dictated by $CuGaSe_2$ poor surface energetics in water (V_{FB}=0.275 V_{RHE} and V_{photo}=100 mV).

Since, several paths have been identified that could potentially improve the STH of copper chalcopyrite-based hybrid photoelectrode devices. Some of these alternative routes are presented in the following section.

3.4 Paths toward efficient copper chalcopyrite-based PEC devices

3.4.1 Identifying PV technologies compatible with $CuGaSe_2$

Achieving STH efficiencies greater that 3.7% using $CuGaSe_2$ as photocathode will require the use of solar cells having absorber with bandgap lower than 1.68 eV. That way, one or more solar cells can be placed under the $CuGaSe_2$ photocathode, reducing the relative area occupied by the PV drivers. Figure 31(a) shows the maximum photocurrent density and STH efficiency achievable with hydride structures as function of the optical bandgap of the bottom and top cell [35]. This calculation was done assuming the optical limit (100% quantum efficiency within absorption range) and a 100% Faradaic efficiency. Assuming a bandgap of 1.68 eV for the top cell (case for $CuGaSe_2$), a photocurrent density greater than 21 mA/cm^2 is theoretically achievable with a 1.1 eV bandgap bottom cell, corresponding to a STH upper limit of 26%. A crystalline Si/$CuGaSe_2$ hybrid device was built by mechanically stacking a $CuGaSe_2$/FTO sample on top of a p-n Si solar cell. As presented in Figure 31(b), the maximum quantum efficiency of the silicon solar cell measured at 0V is significantly reduced once filtered by the $CuGaSe_2$/FTO at wavelengths greater than 750 nm (out of $CuGaSe_2$ absorption range). This is explained by the fact that a significant fraction of light is still reflected by the $CuGaSe_2$ thin film. Integrating the QE of the filtered silicon cell over AM1.5G leads to a photocurrent density of 8 mA/cm^2, a value three times lower than the one predicted by the theoretical analysis. It is important to note that this current density is lower than that generated by a $CuGaSe_2$ at saturation (14-16 mA/cm^2). Therefore, the photocurrent density achievable with a $CuGaSe_2$/Si solar cell hydride photoelectrode will not exceed 8 mA/cm^2. Nevertheless, such photocurrent density could potentially lead to an STH efficiency in the 9-10% range, assuming it can be obtained in a standalone configuration.

Figure 31(c) presents the J-V characteristics measured on a silicon solar cell filtered or not by a $CuGaSe_2$/FTO sample. As expected, the short circuit photocurrent density is reduced when filtered with $CuGaSe_2$, from 34

mA/cm^2 to 8 mA/cm^2. It is important to not that the open circuit potential of the cell decreased by only 50 mV, to reach 480 mV once filtered with $CuGaSe_2$. Therefore, a significant bias is expected from the Si cell in a hybrid configuration.

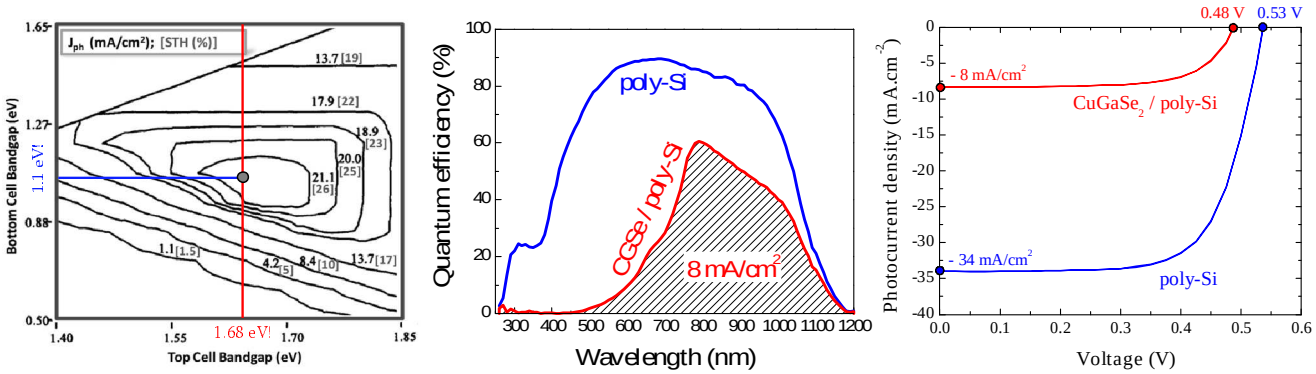

(a) (b) (c)

Figure 31 (a) Maximum photocurrent density and STH efficiency achievable with 2 semiconductors stacked on top of each other as function of their optical bandgap, assuming optical limit and 100% Faradaic efficiency [35] ; (b) Quantum efficiency measured at 0V for the poly-crystalline silicon solar cell (blue) and for the CGSe/crystalline silicon stack (red); and (c) J-V characteristic measured on a polycrystalline silicon solar cell filtered or not by a $CuGaSe_2$ thin film deposited on FTO.

A $CuGaSe_2$/poly-Si solar cell hydride photoelectrode was then constructed and tested. Wires were attached to the cell and covered with epoxy. A clear coating was applied on top of the silicon cell to protect it from the sulfuric acid solution, while the transmitted light not absorbed by the $CuGaSe_2$ photocathode. The exposed area of the cell adjusted with opaque epoxy. The $CuGaSe_2$/FTO PEC electrode was then placed on top and aligned in such a way that its exposed area defined the one of the hybrid photoelectrode (Figure 32(a)). The two devices were finally connected by shorting the wire attached to top contact of the solar cell with the one soldered onto the transparent conductive substrate of the photocathode. The open circuit potential of the device was measured under a 1-sun illumination to ensure that an additional bias provided by the silicon cell. As presented in Figure 32(b), a photovoltage of 425 mV was obtained with this structure, a value significantly higher than the one measured on $CuGaSe_2$ alone (100 mV). Concurrently, a 400 mV anodic shift in onset potential was observed with the hybrid structure when compared to $CuGaSe_2$ alone, as presented in Figure 32(c). $CuGaSe_2$ is compatible with the concept of hybrid photoelectrode, although improvements at surface energetics level are required lower overpotentials for HER in order to split water in a standalone configuration. One example of such improvement is presented in the next section.

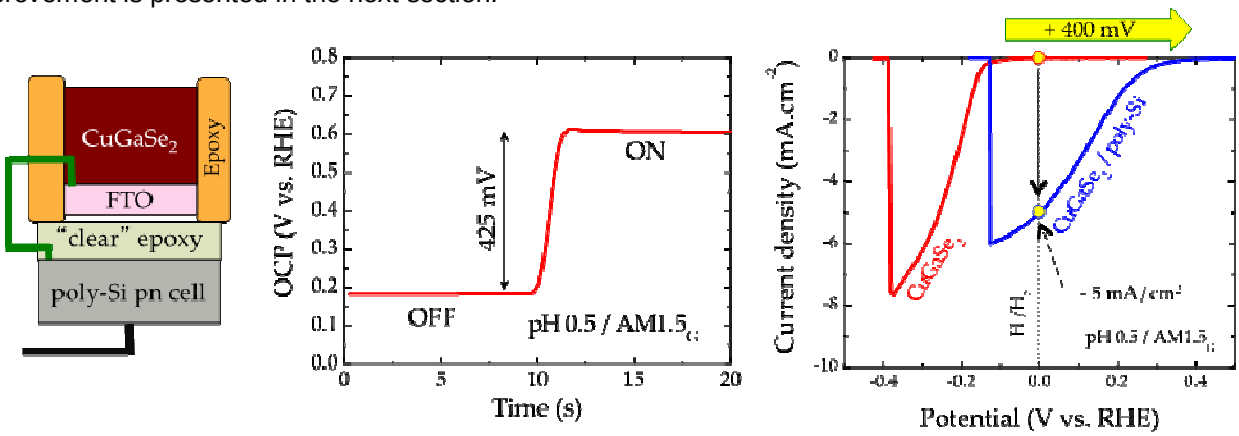

(a) (b) (c)

Figure 32 (a) Schematic of a $CuGaSe_2$/poly-Si solar cell hydride photoelectrode obtained by mechanical stack, (b) open circuit potential measured on a $CuGaSe_2$/poly-Si solar cell hydride photoelectrode under dark and light conditions and (c) LSV measured on $CuGaSe_2$ and $CuGaSe_2$/Si solar cell hydride photoelectrodes.

3.4.2 Reducing $CuGaSe_2$ overpotentials for HER

As demonstrated above, the main limitation to $CuGaSe_2$ resides in poor surface energetics in aqueous solutions. As a matter of fact, Mott-Schottky analysis indicated that $CuGaSe_2$ Fermi level is located only 275 mV below HER and, once illuminated, it generates only 100 mV in photovoltage. One simple way to address this issue is to add an additional material with appropriate energetics on top of $CuGaSe_2$ to move its Fermi level further down (towards OER) and increase the flatband potential. Such improvement can be obtained with n-type semiconductors to form a p-n junction. Cadmium sulfide is a common n-type "buffer" used in copper chalcopyrite absorber for PV that was evaluated also with $CuGaSe_2$ [36-38] in a PEC configuration. However, it is still not clear at this stage if a CdS layer can remain stable is aqueous solution under extended operation. Our research group recently evaluated a non-toxic alternative buffer for PV applications, zinc oxi-sulfude. This material was synthetized via reactive sputtering using a ZnS target. The bandgap of the synthetize film was controlled by adjusting the oxygen partial pressure during the deposition. Thin layers of ZnOS 80 nm thick with bandgap as low as 2.7 eV were deposited on the top of $CuGaSe_2$ photocathodes, followed by the deposition of Ru nanoparticle (HER catalyst). The effect of the ZnOS buffer on $CuGaSe_2$ PEC characteristics is shown in Figure 33(b). After deposition of the ZnOS buffer and the Ru nanoparticles, the onset potential of the $CuGaSe_2$ photocathode shifted anodically by 250 mV, from -150 mV_{RHE} to +100mV_{RHE}. As a consequence, a photocurrent density measured at 0 V_{RHE} increased with the creation of a p-n structure, from 0 mA/cm^2 to -1.5 mA/cm^2.

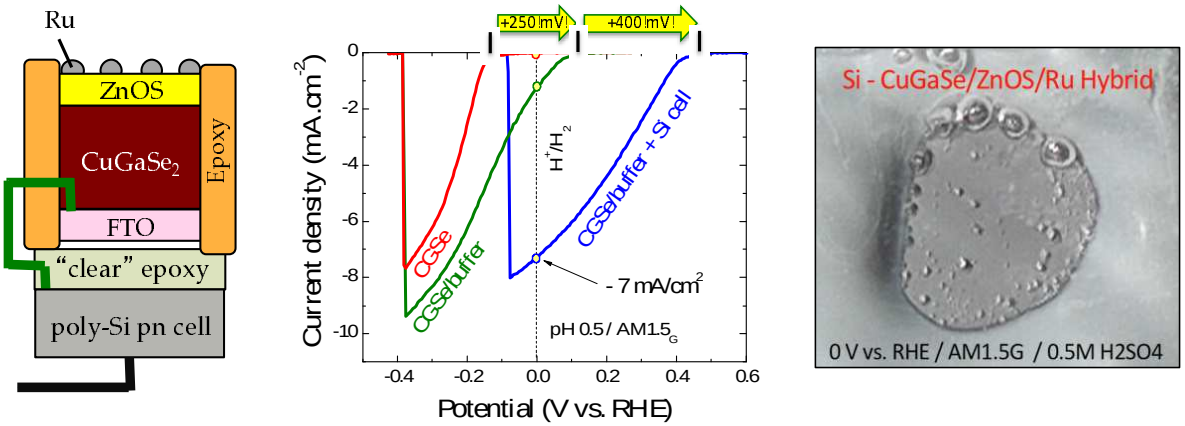

(a) (b) (c)

Figure 33 (a) Schematic of a poly-Si/$CuGaSe_2$/ZnOS/Ru hydride photoelectrode obtained by mechanical stack (b) LSV characteristics measured in 0.5M H2SO4 under simulated AM1.5G illumination on $CuGaSe_2$ photocathode (red curve) $CuGaSe_2$/ZnOS/Ru "p-n-HER structure" (green curve) and poly-Si//$CuGaSe_2$/ZnOS/Ru hybride photoelectrode (blue curve). (c) Picture of hydrogen evolved at the surface of a poly-Si//$CuGaSe_2$/ZnOS/Ru hybride photoelectrode at 0 V_{RHE}.

Also presented in Figure 33(b) are the PEC performances of a hybrid photoelectrode made with the newly formed $CuGSe_2$/ZnOS/Ru "p-n HER" structure and a silicon solar cell. With such structure, the onset potential was shifted 750 mV anodically when compared to $CuGaSe_2$ alone (+250 mV from the p-n structure and +400 mV from the silicon solar cell), leading to a photocurrent density of -7 mA/cm^2 at 0 V_{RHE}. A picture showing hydrogen being evolved at the surface of the poly-Si//$CuGaSe_2$/ZnOS/Ru hybride photoelectrode is showed in Figure 33(c). Although the Faradiac efficiency of this device has not been measured yet, it is expected to be at least as high as the one measured on un-catalyzed $CuGaSe_2$ (86%).

3.4.3 Wide bandgap copper chalcopyrite materials

Creating PEC materials with a 2.0 eV bandgap has been an ongoing mission throughout this research program. As explained above, these values are considered optimal for water splitting since they lead to the best compromise between photocurrent and photovoltage generated is a hybrid photoelectrode. Until recently, our research team had investigated essentially selenide-based copper chalcopyrite material class for PEC applications. Our research confirmed that the highest bandgap achievable with this class cannot exceed 1.68 eV, as demonstrated with $CuGaSe_2$ photocathode. Figure 34 (top left) presents the evolution of the bandgap calculated for of the $Cu(In_{(1-x)}Ga_x)(Se_{(1-y)}S_y)_2$ material class as function of the indium-to-gallium (x-variable) and

selenium-to-sulfur (y-variable) ratios [39]. One can see that a partial or total substitution of selenium with sulfur extends the optical bandgap of this material class beyond 1.68 eV, up to 2.4 eV with $CuGaS_2$. Thus, it is in theory possible to synthesize 2.0 eV copper chalcopyrite materials by choosing appropriate indium-to-gallium and selenium-to-sulfur ratios, as evidenced by the black line in Figure 34 (top left). Although the synthesis of pentanary $Cu(In_{(1-x)}Ga_x)(Se_{(1-y)}S_y)_2$ is technically doable, our team has chosen to focus on quaternary sulfide systems obtained via sulfurization of $CuInGaSe_2$ thin films. This procedure was chosen based on experimental evidences showing that FTO substrates decompose under sulfur atmosphere at temperatures above 350°C via the formation of volatile SnSx species. As a consequence, it was concluded that the synthesis of sulfide-based copper chalcopyrite on FTO via co-evaporation was nearly impossible.

In HNEI process, a 1 micron-thick $CuInGaSe_2$ layer is first deposited on FTO using a 2-stage process similar to the one used for $CuGaSe_2$, except for the deposition temperature that was kept below 350°C to prevent complete crystallization of the film. The $CuInGaSe_2$ are then sealed into a closed capsule with a small piece of elemental sulfur under argon. The capsule is then placed into a furnace and annealed at a temperature and for a duration that depends on the $CuInGaSe_2$ thickness and co-evaporation temperature.

Figure 34 (top right) presents the XRD spectra of $CuIn_{0.3}Ga_{0.7}Se_2$ before and after annealing. One can see that $CuIn_{0.3}Ga_{0.7}Se_2$ spectrum is shifter to higher angle after the annealing step, matching the theoretical spectrum for $CuIn_{0.3}Ga_{0.7}S_2$ (sulfide). Both samples were sent to Clemens Heske's group at UNLV for surface analysis. X-ray photoemission spectroscopy confirmed the sulfurization of as-deposited selenide-based copper chalcopyrite thin films, as annealed samples contained only sulfur 2p was on their surface (Figure 34, bottom left). Subsequent Raman analysis performed at HNEI essentially confirmed the XRD and XPS results, although one peak corresponding to the selenide-based copper chalcopyrite remained after the annealing step (Figure 34, bottom right). Bulk composition analysis obtained by energy dispersive x-ray method confirmed that the annealed samples contained roughly 2% selenium and 45% sulfur. The nature of the sulfurization process (top to bottom diffusion of sulfur) leads us to believe that majority of the selenium is located near the FTO/$CuInGaS_2$ interface (also confirmed by the fact the no selenium was detected by XPS at the surface of the film).

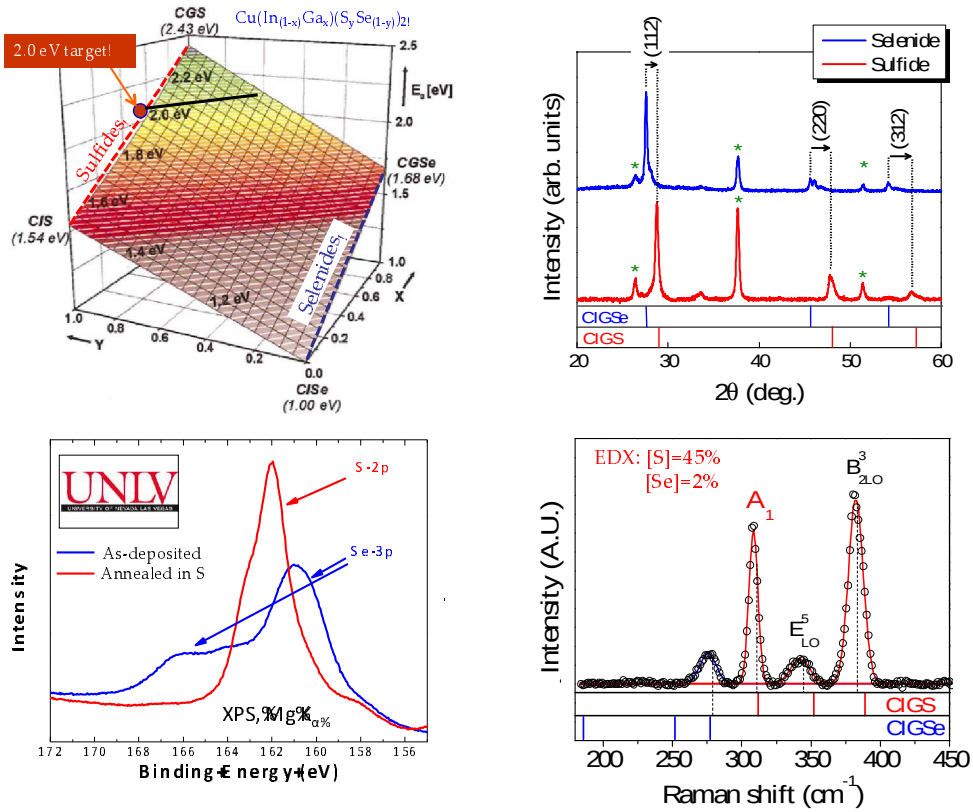

Figure 34 (Top left) Contour plot representing the evolution of the bandgap of $Cu(In_{(1-x)}Ga_x)(Se_{(1-y)}S_y)_2$ as function of the indium-to-gallium (x-variable) and selenium-to-sulfur (y-variable) ratios (from [39]). (Top right) X-ray diffraction (bottom left) X-ray photoemission spectroscopy (performed at UNLV) and (bottom right) Raman spectra measured on as-deposited and sulfur-annealed $CuInGaSe_2$.

A picture of $CuInGaS_2$ samples obtained via sulfurization of $CuInGaSe_2$ is presented in Figure 35 (top left). The sample on the left is HNEI's 1.68 eV baseline $CuGaSe_2$. After sulfurization, this sample turned into a bright yellow 2.4eV CuGaS2 film (last sample on the right). Then, increasing the indium-to-gallium competent during the $CuInGaSe_2$ synthesis, the bandgap decreased from 2.4eV to 2.2eV (orange film, third sample from the left) to finally reach 2.0eV (red film, second sample from the left). The Tauc plot measured on these samples before and after annealing is presented in Figure 35 (top right). Preliminary PEC tests were performed on 2.0eV $CuIn_{0.3}Ga_{0.7}S_2$ samples. A flatband potential of -0.5 V_{RHE} was measured by Mott-Schottky (M-S) analysis. Figure 35 (bottom left) presents the expected surface energetics of $CuIn_{0.3}Ga_{0.7}S_2$ obtained by combining data gathered from M-S and UV-visible spectroscopy analyses. When compared to $CuGaSe_2$, the valence band in $CuIn_{0.3}Ga_{0.7}S_2$ sites 200 mV lower (closer to OER), whereas the conduction band is located 100 mV higher. This suggests that the bandgap modification in sulfurized films primarily stems from a downward shift of the valence band, an ideal situation for photocathode systems. Linear sweep voltammetry performed in 0.5M H_2SO_4 under AM1.5G simulated illumination revealed the excellent photo-conversion properties of the newly formed 2.0 eV $CuIn_{0.3}Ga_{0.7}S_2$ material, with photocurrent densities of -3.5 and -6.0 mA/cm2 at 0 VRHE and -0.4 VRHE, respectively, with negligible dark current from flatband potential (+0.5 VRHE) to photocurrent saturation (-0.5 VRHE), as shown in Figure 35 (bottom right). It is worth mentioning that photocurrent is being generated in 200 mV anodic from the flatband potential, a clear improvement when compared to the 500 mV required to turn water splitting on with $CuGaSe_2$.

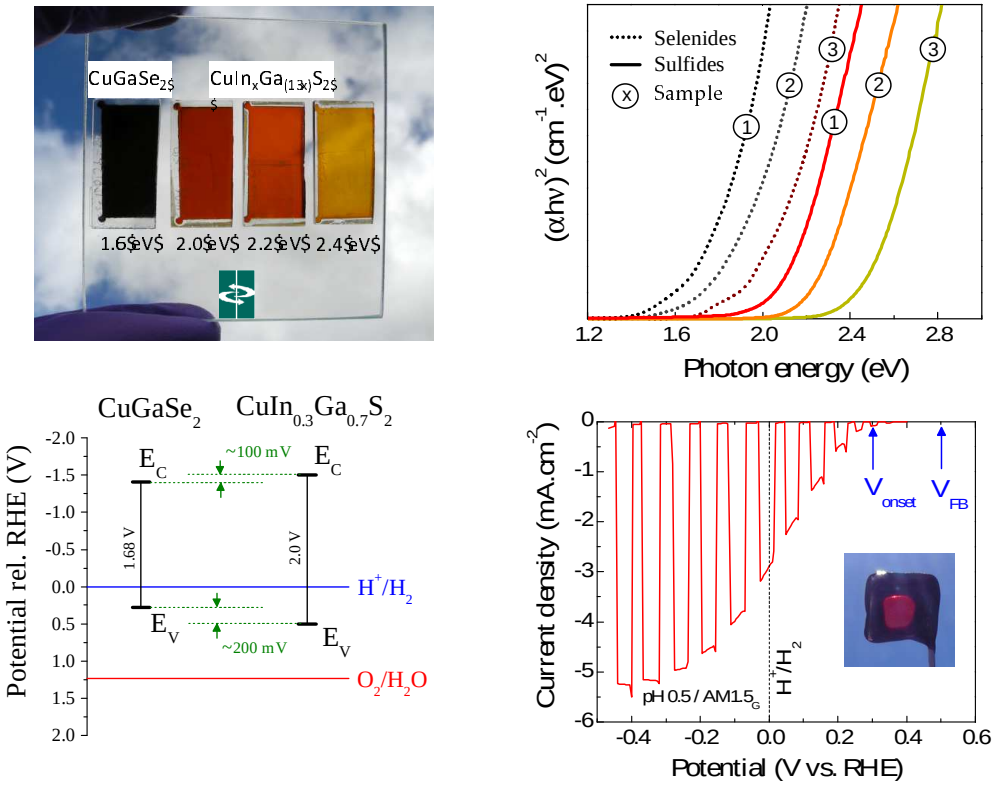

Figure 35 (Top left) Optical images and (top right) Tauc plots of wide bandgap $CuInGaS_2$ materials. (Bottom left) Proposed surface energetics of 1.6eV $CuGaSe_2$ and 2.0eV $CuInGaS_2$ photocathodes. (Bottom right) LSV characteristics measured on a 2.0eV $CuInGaS_2$ photocathodes.

4. Metal Oxides

4.1 Motivations and main technology barriers

Three decades after the demonstration of photo-electro-chemical water splitting by Fujishima and Honda with TiO_2 [1], intensive research is still ongoing to identify a suitable semiconductor to be integrated in an efficient, cost effective, and reliable photo-electro-chemical (PEC) system. Among all candidates, binary transition metal oxides are still drawing lots of attention as they offer good resistance to corrosion and are inexpensive to produce. However, no system having both appropriate optical absorption and good transport properties have been discovered yet. Tungsten trioxide (WO_3) is an n-type semiconductor that has been chosen as a model material to validate the concept of photoelectrochemical (PEC) photoanodes. WO_3 has been an ideal photoanode material in the study of PEC water-splitting systems because it inherently has good photon absorption generating decent amount of photocurrent, good electron transport properties, and stability against photo-corrosion. In practice, WO_3 photoanodes have been implemented in prototype multijunction PEC systems including hybrid photoelectrode [40] and dual photoelectrode cell approach [41]. As the basis for a thin-film photoanode in an efficient water-splitting device, pure WO_3 falls short on two principal fronts. The first barrier is a bandgap (between 2.5-2.8 eV) that is too high to absorb an adequate portion of the solar spectrum. As experimentally validated, the high bandgap limits achievable photocurrents, resulting in devices with solar to hydrogen (STH) conversion efficiencies which do not exceed 3 percent [42]. In perspective, optimized material systems will be needed to meet the DOE's 2020 benchmark of 20% STH conversion efficiency. A second barrier for pure WO_3 is the non-optimal band-edge alignment of the conduction band. PEC experiments on WO_3 films in acidic aqueous media have indicated a conduction band minimum that is lower than the hydrogen evolution reaction reduction potential. In the photoanode configuration, this non-favorable band edge alignment results in the need for a supplemental voltage bias, complicating the design of practical water-splitting devices. As we continue to forward in the R&D of tungsten-based compounds, the primary thrust of our research plan is focus on the bandgap and band-edge alignment issues. Based on comprehensive theoretical and experimental feedback efforts, new multi-component tungsten-based compounds are being developed with raised valence band maximum and conduction band minimum, ideally resulting in a sufficiently low bandgap for high photocurrents and favorable band-edge alignment to minimize or eliminate voltage bias requirements. Materials processing and stability issues for new promising compounds are also be addressed.

Although pure WO_3 is not sufficient to meet DOE's long-term water-splitting performance targets, tungsten-based compounds show great promise with respect to the three major materials-related barriers listed in the US DOE EERE Hydrogen program plan. This section highlights the challenges and strengths of tungsten-based compounds in this context, and outlines research solution pathways specific to this material class.

4.2 Addressing the challenges

Materials Durability. Long-term stability in acidic media needs to be evaluated on tungsten oxide-based materials.

Materials Efficiency. Different approaches are currently being evaluated to address WO_3 bandgap reduction, band-edge alignment with water redox potential and optimized surface activity. Incorporation of ions into WO_3 bulk film can be performed to enhance absorption properties (i.e. bandgap reduction), as predicted by density functional theory calculation.

Bulk Materials Synthesis. Several techniques including sol-gel, CVD and reactive sputtering are ideally suited to this material. Other methods such as Atomic Layer Deposition (ALD) should be evaluated.

Device Configuration Designs. For initial studies, the multijunction device structure can be validated via mechanical stacks (already validated with WO_3). With identification of an ideal top PEC material, the engineering of the complete multi-junction device will be concluded. Work on fully integrated (monolithic) devices will require close collaboration with our industrial partner (MVSystems).

4.3 Technical accomplishments achieved with tungsten trioxide

4.3.1 Material durability

Material durability is a critical aspect of hydrogen production via solar-powered water splitting. To be durable, a semiconductor material must preferentially reduce or oxidize ions rather than corrode. Whether a photoanode (n-type materials such as WO_3) is resistant to corrosion depends on the alignment of its oxidation potential relative to H_2O/O_2 level. As a rule of thumb, a photoanode is stable if its redox potential is lower than either H_2O/O_2 redox potential or its valence band position (VBM) [43]. Figure 36(a) presents the relative position of the conduction band and valence band of various semiconductors with respect to their corrosion potentials as well as the water splitting potentials at pH0 calculated by ab initio. It the case of WO_3, one can see that the oxidation potential (red bar) is located between its VBM (green block) and water oxidation potential (red dashed line). Therefore, tungsten trioxide is theoretically stable is acidic solutions, as photo-generated hole would preferentially oxide water. The potential dependence of WO_3 stability in various pH was reported several times in the literature. So-called Pourbaix diagram presented in Figure 36(b), WO_3 is stable in acidic solution (pH0 to pH4) under anodic potentials. Thus WO_3 photoanode should be stable under PEC operation (anodic potential for photoanodes).

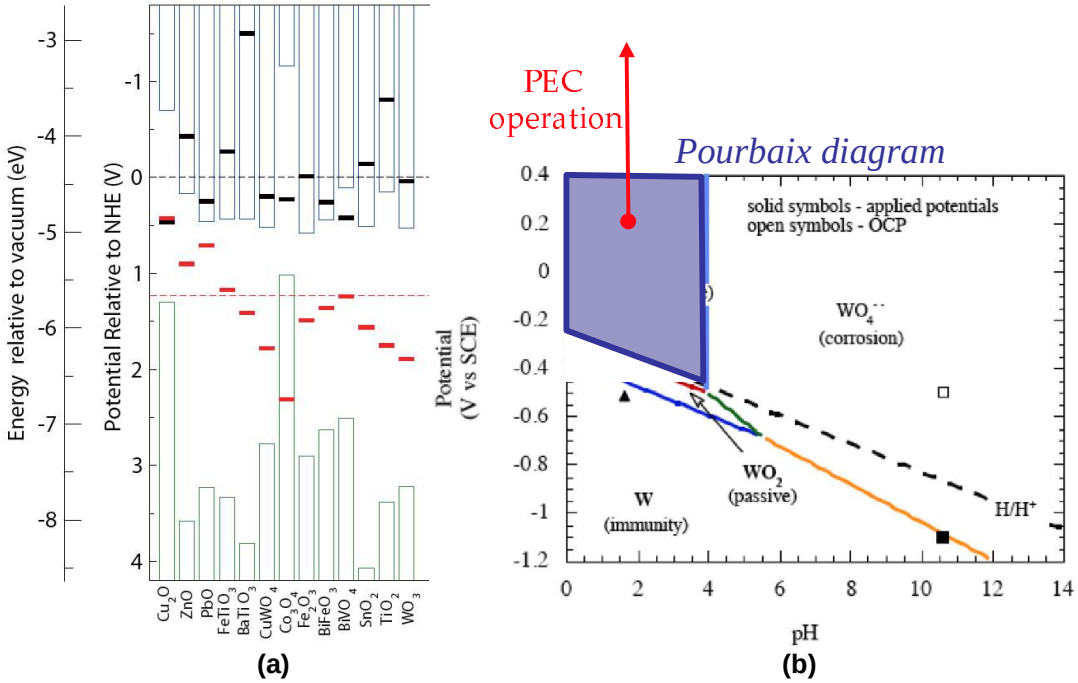

Figure 36 (a) Position of the conduction (blue blocks) and valence band (green blocks) of several semiconductors with respect to their reduction (black bars) and oxidation (red bars) potentials and water reduction (black dashed line) and oxidation (red dashed line) potentials. (b) Pourbaix diagram of WO_3.

The stability of WO_3 photoanodes was experimentally validated by HNEI on reactively sputtered WO_3 thin films in pH2 buffer electrolyte under a constant potential of 1.6V vs. SCE. Several light sources were evaluated as an alternative to costly (and short lifespan) Xe-arc bulbs usually used to mimic AM1.5G illumination. Tungsten bulbs were ruled out as they do not emit enough UV. Decision was made to use UV-white LED light bulbs instead. Under these conditions, a fairly steady photocurrent density of 3 mA/cm^2 was recorded on five WO_3 samples over 600 hours, with no visible degradation observed on the sample, as showed in Figure 37.

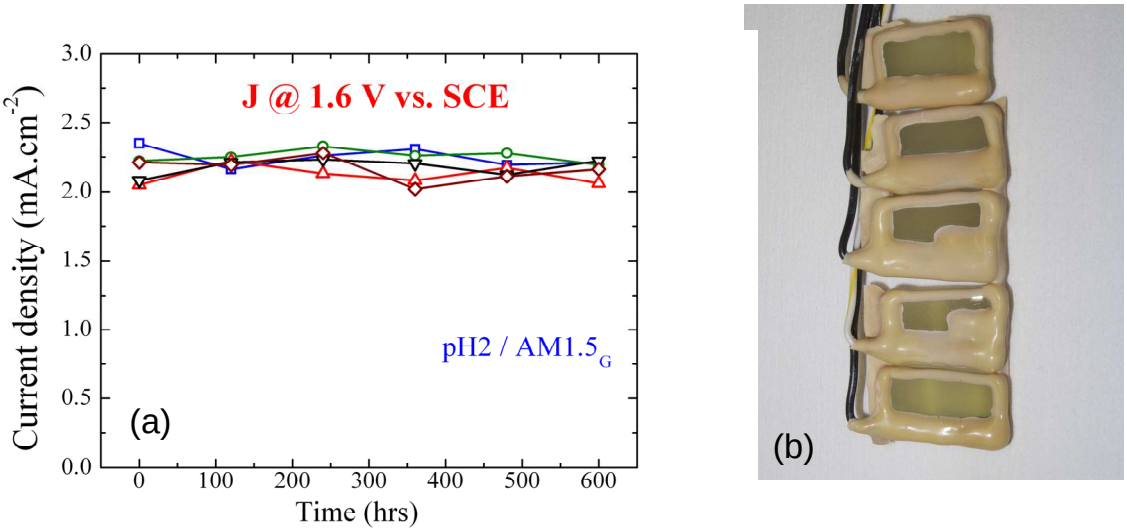

Figure 37 (a) Chronoamperometry (current density vs. time) measured on 5 WO_3 photoanodes at a potential of 1.6 V vs. SCE. (b) Picture of the 5 samples after the 600-hour durability test.

4.3.2 Near-surface engendering with bilayer approach

Several attempts were performed during this research program to improve the surface energetics of WO_3 material class. Based on theoretical calculation [44], a series of foreign elements have been incorporated into tungsten trioxide bulk, including sulfur and nitrogen. In both cases, no clear evidence of band-edge modification was observed, although absorption characteristics were impacted by these treatments. A closer look at UV-visible spectra revealed possible free carrier absorption for WO_3:N and WO_3:S systems which could originate from defect points in the newly formed systems. It is worth mentioning that structural characterization (X-ray analysis) pointed out a dramatic phase modification after foreign element incorporation, from monoclinic/orthorhombic (known structures for WO_3) to cubic-like system. The later could emerge only if a high concentration of defects (oxygen vacancies) is present in the material. Subsequent PEC characterization pointed out poor performances when compared to pure WO_3 material; mostly related to weak carrier transport due to grain structure degradation [45]. It is worth mentioning that in the nitrogen case, XPS analyses performed at UNLV at newly formed thin film surface has not revealed so far the presence of any nitrogen species, indicating weak bonds between involved species.

Encouraging results have been obtained when Mo is incorporated at the WO_3 surface only, forming a bilayer structure with a 200nm thick Mo-doped WO_3 layer sitting on a 2 micron thick WO_3 absorber (Figure 38, top left). A 15% enhancement of the generated photocurrent at 1.6V vs SCE as well as a 200 mV onset potential reduction (tested under simulated AM1.5G illumination in 0.33M H_3PO_4 electrolyte) were observed [46] (Figure 38, top right).

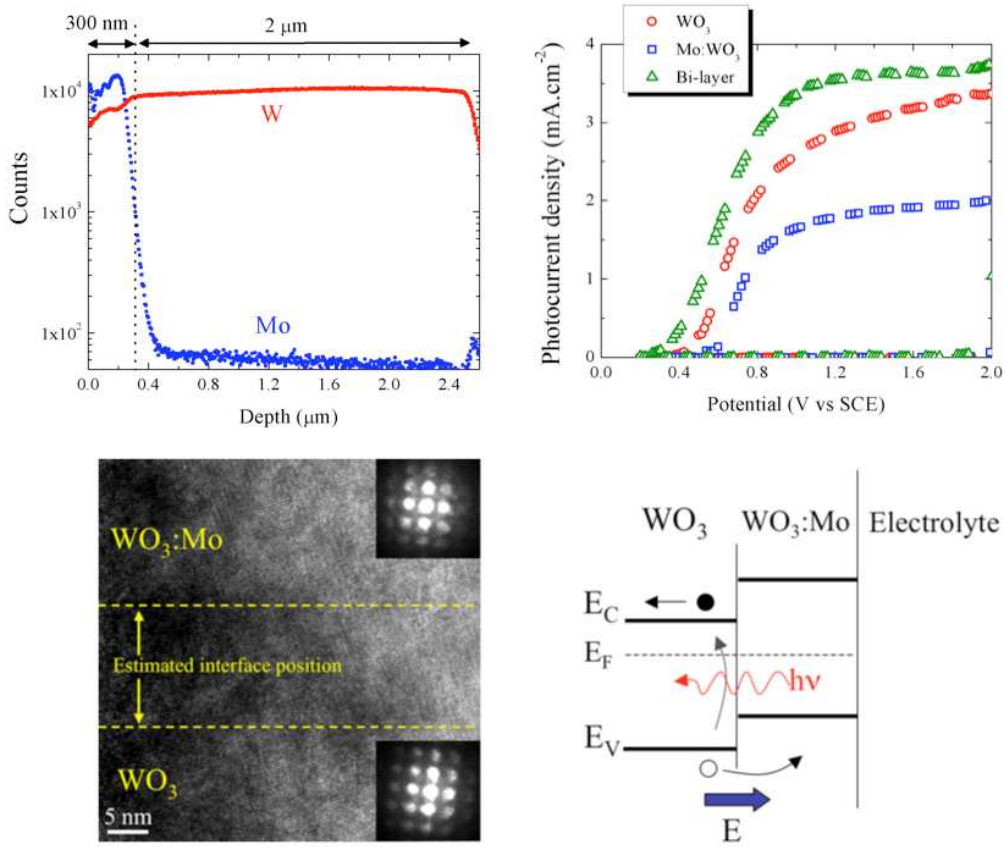

Figure 38 (Top left) Secondary Ion Mass Spectroscopy measured on a bilayer sample. (Top right) Linear Sweep Voltammetry scans measured on pure WO_3, Mo-doped WO_3 and Mo:WO_3/WO_3 bilayer PEC electrodes. (Bottom left) High resolution TEM image of the interface between the Mo-doped WO_3 top and WO_3 bottom layers. (Bottom right) Proposed energy band diagram of the bilayer structure using surface spectroscopy analyses performed at UNLV.

It is believed that improved bilayer performances may come from a beneficial effect of the WO_3 bottom layer on Mo:WO_3 grain growth. In fact, bilayer structure shows highly crystalline grains when compared to those of bulk Mo:WO_3 materials (Mo incorporation in the whole film). High-resolution TEM characterizations performed at NREL indeed validated this point (Figure 38, bottom left). Further electron spectroscopy analyses (UPS and IPES) performed at UNLV pointed out that Mo incorporation into WO_3 leads to a conduction band-edge position increase of 210 meV [47] when compared to pure tungsten trioxide [48]. In a bilayer configuration, this difference in Fermi level position leads to the formation of built in potential which direction and strength promotes photogenerated holes diffusion toward the PEC material/electrolyte interface (Figure 38, bottom right).

4.3.3 Surface catalysis of WO_3

First evaluation of RuO_2 particle deposition on WO_3 films has been evaluated by UCSB for catalytic purposes. RuO_2 particles have been either deposited using an electrochemical process on HNEI reactively sputtered WO_3 or deposited using spray pyrolysis on UCSB electrodeposited WO_3. No major improvement in either saturated photocurrent or the onset potential has been observed after RuO_2 surface treatment. In a second phase, HNEI developed at RuO_2 nanoparticle sputtering process using a pure Ru target in oxidizing environment. By adjusting the deposition duration (basically less that 30 seconds), RuO_2 nanoparticles (5-10 nm mean size) were successfully deposited on tungsten trioxide thin films (Figure 39(a)). Subsequent PEC characterization indicated a 20% increase in photocurrent density a low potential while the onset potential and the saturated photocurrent remained unchanged (Figure 39(b)). This is a clear indication that surface catalysis was effectively addressed with RuO_2 treatment. In addition, full sheet RuO_2 films have been fabricated at HNEI using identical process. Tests in a two electrode configuration using p-type material (CGSe or a-SiC) as working electrode and an

optimal RuO2 film as counter electrode have already shown improved results, i.e. a 500 mV onset potential reduction when compared to Pt counter electrode.

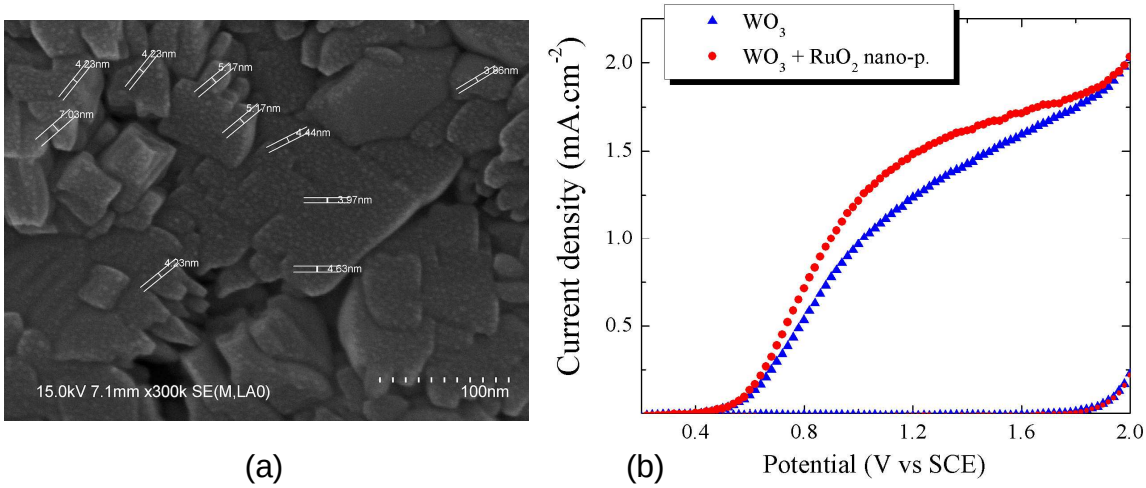

Figure 39 (a) SEM picture of WO_3 covered with RuO_2 nanoparticles (3-5 nm in diameter). (b) LSV characteristics measured on WO_3 before and after RuO_2 surface treatment.

4.3.4 Integration of WO_3 into a standalone PEC/PV device

Since hydrogen production using a standalone device is our main goal, efforts have been made to combine both a-Si tandem solar cells and tungsten trioxide PEC electrode in one monolithically integrated device. Preliminary tests were done using so-called mechanical stack, where the WO_3 photoelectrode was placed above MVSystems' a-Si tandem solar cell (see Figure 8(b)), as depicted in Figure 40(a). Under these conditions, photons with energy greater than 2.6 eV (wavelength less than 475 nm) are absorbed by WO3, whereas photons with energy less than 2.6 eV are transmitted to the a-Si-based tandem solar cell. In these conditions, a short circuit photo-current density of 2.5 mA/cm2 was obtained in acidic solution under simulated AM1.5G illumination (Figure 40(b)), corresponding to a STH efficiency of 3.1% (assuming 100% Faradaic efficiency).

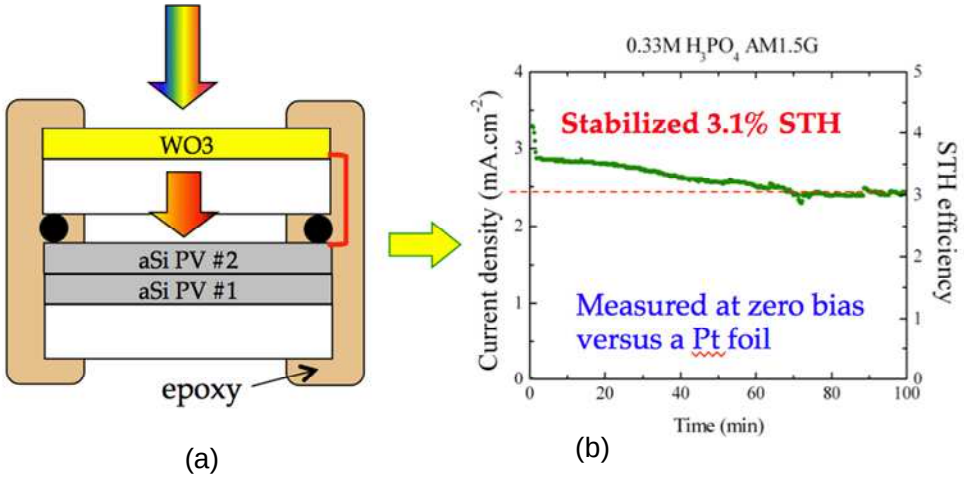

Figure 40 (a) Schematic representing a hybrid a-Si/a-Si PV/WO_3 PEC electrode obtained by mechanical stack. (b) Short circuit photocurrent density measured with this device vs. a platinum foil under simulated AM1.5G illumination.

Forming a WO_3-aSi monolithic device is not a simple task. The main barrier lies in the process temperature incompatibility between the engine (a-Si) and the PEC material (WO_3). HNEI demonstrated via temperature cycling that WO_3 couldn't be integrated in traditional hybrid structure where the PEC material is deposited on top of the PV system, as a-Si solar cells degrades rapidly when exposed to 300°C for 3 hours (Figure 41(a)). The

solution resides in a bifacial integration, where the tungsten oxide film is deposited first on the front side of the transparent conductive oxide (TCO) substrate (performed at HNEI) followed by the deposition of the solar cell on the backside (performed at MVS). First monolithic devices were successfully fabricated in 2011 (Figure 41(b)) and tested under out-door conditions (Figure 41(c)). Although, the overall STH efficiency (1.5%) was lower than that obtained with mechanical stacks (3%), this demonstration proved that the concept was feasible. It is worth mentioning that the limiting factor in this integration scheme is no longer the a-Si material but the TCO substrate which can withstand temperatures up to 550°C. This makes the bifacial approach compatible with numerous PEC materials, including I-III-VI2 (e.g. CuGaSe2).

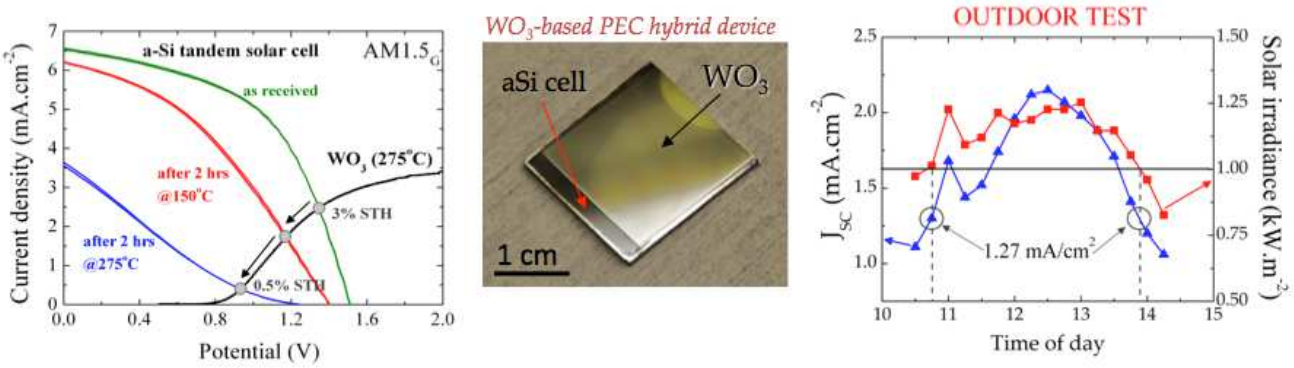

Figure 41 (a) J-V characteristics measured on an a-Si solar cell after being annealed at different temperatures for 2 hours. (b) Picture of a bi-facial hybrid aSi-aSi/WO_3 photoelectrode. (c) Short circuit photocurrent density measured under outdoor illumination at different time of the day.

4.4 Identifying new tungsten oxide-based material with optimum optical characteristics for PEC water splitting

The optical and electronic properties of all existing binary systems have been studied and are well documented. To the best of our knowledge, only two binary metal oxides can fulfill the requirements in term of band gap for PEC applications: Fe_2O_3 (2.0 eV) and Cu_2O (1.95 eV). In the latter case, recent work performed on cuprous oxide showed that this material can generate up to 7 mA/cm^2 at saturation, making this material the best binary oxide ever synthesized for solar conversion applications [49]. The only issue with such system is its thermodynamic stability. Indeed, it is possible that, over time and under operation, cuprous oxide (Cu_2O) turns into cupric oxide (CuO), whose bandgap (1.2 eV) is far from ideal for PEC applications. In the light of these examples, it appears that one needs to search beyond binary oxides in order to find the ideal oxide system for low-cost solar-assisted hydrogen production.

With the increased number of elements in ternary and quaternary compounds, it is difficult to design a unique system capable of satisfying optical absorption, electronic conductivity and resistance to corrosion. One approach resides in pure combinatorial analysis, where sets of selected elements are automatically blended to form series of compounds. Though rather challenging to perform with vacuum-based processes (e.g. sputtering), recent progress in solution-based (ink) have greatly improved combinatorial-based PEC research and led to the emergence of interesting new PEC systems. However, one should bear in mind that the success of such approach should not be based only on opportune material discovery. Similar combinatorial approach has been employed in the past in the field of superconductors to investigate compounds containing up to 6 elements (i.e. HgTlBaCaCuO). While material discoveries in this field were used to be quite “serendipitous” [50], modern density functional theory calculation has since permitted to predict trends to design new superconducting material classes. Thus, the ability to design new ternary and quaternary oxide minerals for PEC applications guided by density functional theory predictions is the most effective way to identify new metal oxides with appropriate properties for PEC water splitting.

4.4.1 Ternary tungstate materials

With an electronic band-gap of 2.2 eV and optimum surface energetics for water splitting [51,52], copper tungstate ($CuWO_4$) is a promising material-class that merits further investigation. Although fairly new in the field of PEC, metal tungstates have been investigated for more than three decades for their scintillation characteristics. A large number of papers have been published on the microstructure and optical characteristics of this material class and metal tungstate-based scintillators are widely used in the field of detection. As an example, calcium tungstate currently equipped the Dark Matter Cryogenic detector at CRESST in Gran Sasso in Italy. Cadmium tungstate is widely used for positron emission tomography in medical diagnosis. Finally, the Electromagnetic Calorimeter detector at the Large Hadron Collider (CERN) is made of approximately 100,000 lead tungstate crystals. In this material class, copper tungstate is the only material with a bandgap (2.2 eV) that is appropriate for PEC applications. However, less than ten papers have been published specifically on the photoelectrochemical properties of $CuWO_4$ since Benko's (Brock University) first report in 1982 [53]. Initial work done at HNEI indicated that the conductivity type of $CuWO_4$ was strongly affected by its crystallographic properties [54]. Co-sputtered films deposited at 300°C were found to be amorphous with p-type conductivity, whereas films annealed at 500°C in argon turned crystalline and exhibited n-type conductivity (Figure 42(a)). Subsequent PEC characterizations revealed that only n-type copper tungstate was photoactive (Figure 42(b)). Finally, impedance analyses indicated that the low photocurrent densities achieved with this material class originated primarily from a relatively high bulk resistivity.

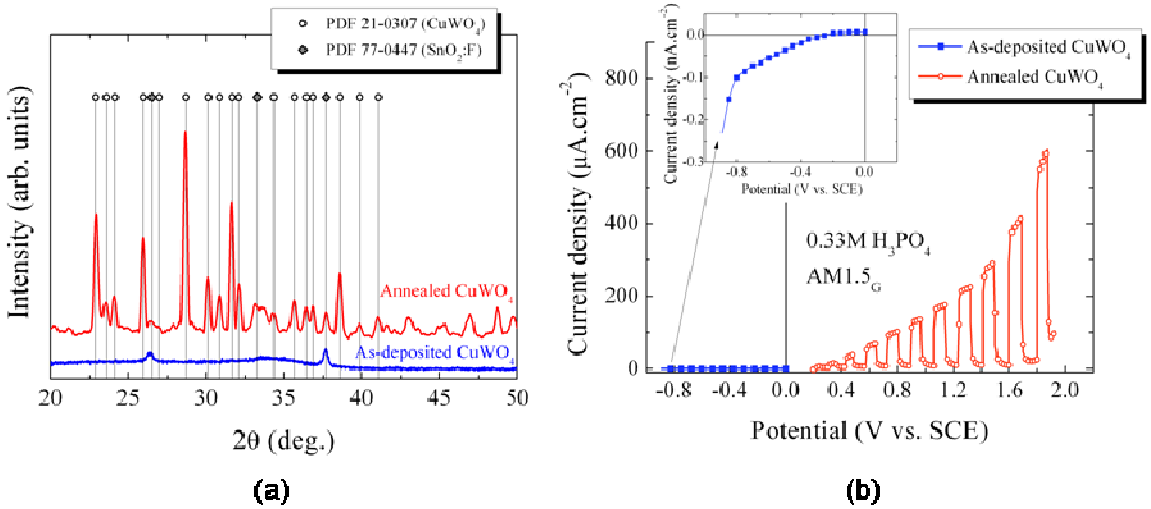

Figure 42 (a) X-ray diffraction patterns measured on as-deposited and annealed CuWO4 thin films. (b) LSV scans measured in 0.33M H3PO4 electrolyte under simulated AM1.5G illumination.

Several approaches were tested to reduce copper tungstate bulk resistivity. The most effective method was to incorporate conductive carbon nanotubes (CNT) into $CuWO_4$. Such nanocomposite systems were fabricated by means of spray deposition using solutions containing copper acetate, ammonium metatungstate and carbon nanotubes (CNT). After annealing in air at 500°C, $CuWO_4$ nanoparticles were formed onto the CNT, as presented in the TEM image in Figure 43(a). Incident photon-to-current spectroscopy (IPCE) analyses were performed on both un-modified $CuWO_4$ and nanocomposite photoanodes at a potential of $0.8V_{SCE}$ in pH10 buffer solution (Figure 43(b)). Photon-to-current efficiencies measured on nanocomposites exhibited highest efficiencies over un-modified $CuWO_4$ photoanodes. More importantly, the increase in efficiency after addition of CNT was found to be relatively constant at all wavelengths within $CuWO_4$ absorption range (i.e. +22%). This indicates that CNT current collectors operate with the same effectiveness in the entire $CuWO_4$ bulk, shuttling electrons photo-generated by high-energy photons near the point of entry of light as well as low-energy photons deeper in the semiconductor bulk. This study demonstrated that a *light absorber/charge collector* composite approach could be used to improve the performances of photoelectrochemical systems known to be limited by poor charge transport properties.

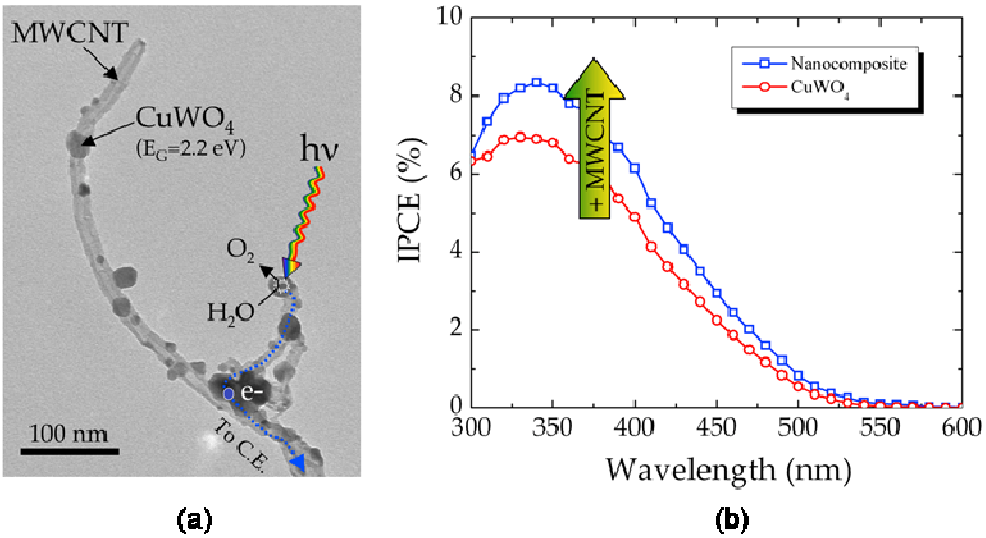

Figure 43 (a) TEM picture of $CuWO_4$-carbon nanotube composite material. (b) Incident photon-to-electron efficiencies measured on pure $CuWO_4$ and $CuWO_4$-carbon nanotube composite photoanodes.

4.4.2 Quaternary tungstate materials

It has been mentioned earlier that the introduction of impurities for doping would create unwanted defect-states in the band gap, which, in turn, would be detrimental to the crystallinity and the transport properties of the host materials. In addition, the presence of highly localized orbitals at the band edges (such as at the valence band maxima or the conduction band minima of Mott or charge transfer-type insulators), results in high effective mass charge-carriers, and hence high electron-hole recombination rate. On the other hand, a thermodynamically stable alloy structure with desirable materials compositions can provide better crystallinity and, hence improved charge transport properties. From the theoretical point of view, predicting novel alloys of multi-cation metal oxides satisfying all the electronic criteria of an efficient photocatalyst is a challenging task. Nonetheless, recent advances in computers and theoretical methods made it possible to investigate and predict materials at a fundamental level, which was not possible before. In addition, an efficiently combined experiment-theory approach can expedite the prediction and characterization processes further. With our new theoretical approach for materials design by searching mineral data-base, we were able to predict several new tungstate-based multi-cation metal-oxides. For example, from a combined mineral data-based search and DFT calculations, we were able to predict so far unknown crystal structure of $AgBiW_2O_8$, and the corresponding electronic properties such as band structure, density of states, optical absorptions, etc. These results were then compared with the experimental findings. We recently have predicted the crystal structure of a new alloy, namely $CuBiW_2O_8$, which has a lower band gap and a higher valence band maximum than $AgBiW_2O_8$. In contrast to WO_3, both of these two materials straddle the hydrogen and oxygen reduction potentials. The theoretical XRD plot and other electronic and optical properties were calculated for the newly predicted material to guide the experimental findings. Figure 44 presents the band structure of both $CuWO_4$ and $CuBiW_2O_8$ materials obtained by DFT in Prof. Huda's group at University of Texas at Arlington (UTA). One can see that $CuWO_4$ contains mid-gap empty split states that originate from Cu-d bands. These localized empty states could potentially trap photogenerated electrons, limiting the photocurrent. It can be also seen that the conduction band are relatively flat, suggesting a very high electron effective mass. This could also limit the overall photogeneration process due to high a recombination rate. However, the addition of bismuth significantly alters the band structure of the material. In fact, one can see that the mid-gap states (traps) disappeared after in $CuBiW_2O_8$. Also, the conduction band is more dispersed, indicating a higher mobility for electrons. As a consequence, one can expect high electrical conductivity in $CuBiW_2O_8$.

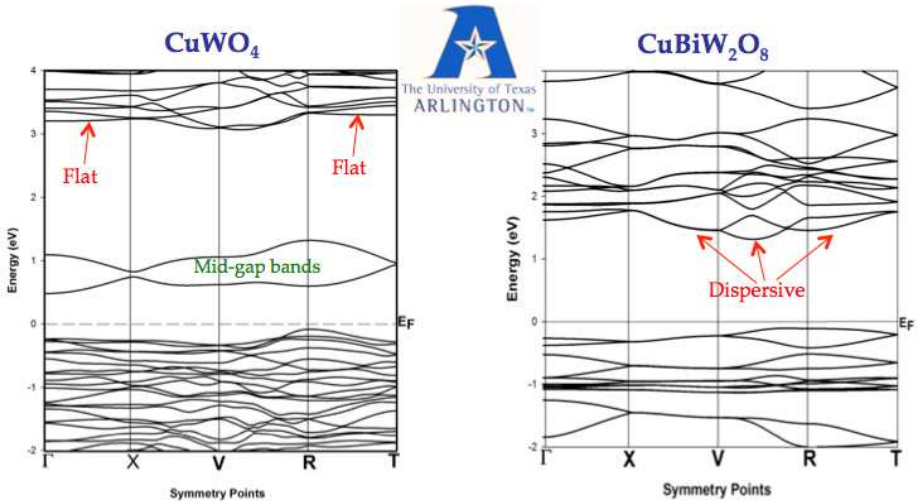

Figure 44 Band structures of (left) $CuWO_4$ and (right) $CuBiW_2O_4$ semiconductors calculated by DFT calculations.

In order to validate this theoretical calculation, conductivity measurements were performed on solid ceramic oxides containing copper, bismuth, tungsten and oxygen. Precursors used were nanopowder of CuO, Bi_2O_3 and WO_3. All nanopowders were taken in stoichiometric amount and mixed thoroughly by using mortar. Apart from this, another alloy was prepared contained mortar mix nano powder of CuO and WO_3 with 2.5 % Bi_2O_3 doped (equivalent to a doping level of 1000 ppm). Powders were then compacted using a uniaxial press under a pressure of 2 ton/cm^2 to make pellets. Finally, the pellets were annealed in air at 850^{0}C for 6 hours. Samples were soldered using indium coating for the resistance measurement that was carried out at various temperatures using impedance spectroscopy analysis (Figure 45(a)). The results of these analyses are presented in Figure 45(b), plotted in Arrhenius fashion. First, one can see that WO_3 present the highest conductivity of all materials (10^{-4} S.cm-1 at RT), which is not surprising. Also, it should be pointed out that similar characteristics were measured on both WO_3 ceramic pellets (3 mm thick) and WO_3 thin film (2 microns) sputtered on glass. This indicates that measuring conductivity on bulk ceramic is a convenient and reliable method to access the properties of new oxide minerals. One can see also that $CuWO_4$ presents the lowest conductivity (10^{-8} S.cm^{-1} at RT), in good agreement with previous PEC characterizations. However, the addition of only 2.5% Bi (1000 ppm) had a tangible effect on the conductivity, especially above 60^{o}C. When added to form $CuBiW_2O_8$ alloy, the addition of bismuth increased the conductivity by a factor of 100 when compared to $CuWO_4$, confirming the theoretical calculations made by Prof. Huda.

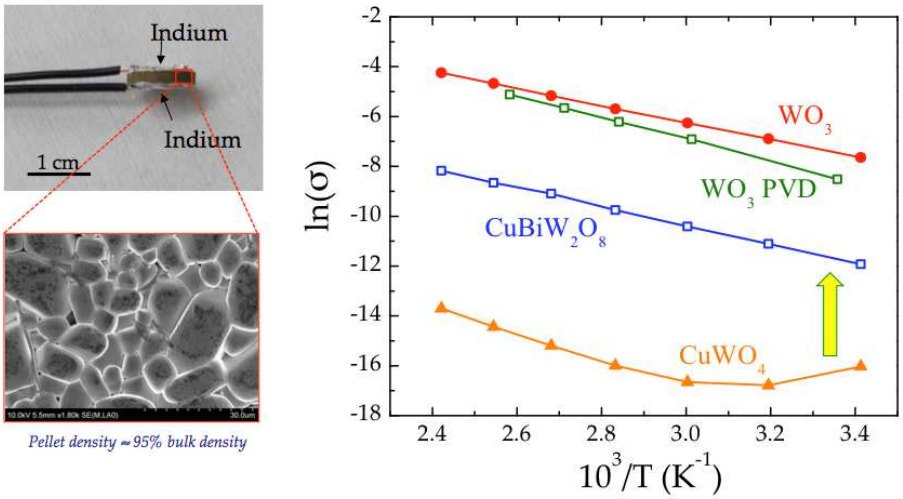

(a) (b)

Figure 45 (a) Picture of $CuWO_4$ pellets obtained via powder sintering and SEM micrograph showing the pellet density. (b) Conductivity measured on various oxides plotted in the Arrhenius fashion.

5. Techno-Economic Analysis Using H2A Production Model

This section summarizes the techno-economic analyses performed using the H2A model (version 3) [55] with amorphous silicon-based hybrid photoelectrodes. At the time this report is submitted to DOE (December 2013), the amorphous SiC-based PEC material class offered the best overall performances in terms of SHT efficiency (6.1% using a crystalline Si solar cell as the driver, assuming 100% Faradaic efficiency) and longest durability (up to 790 hours). Since the use of crystalline Si solar cells was a late development and full understanding of the maximum STH efficiency of the hybrid device is not clearly known at this stage, we focused on the hybrid device utilizing the a-Si solar cell in this analysis. At a 3.7% STH efficiency (demonstrated in this project), the hydrogen production cost for this type of hybrid device falls just short, i.e. at 25-26 \$/kg H_2, of the DOE's goal of \$22/kg. However, with some improvements of either the a-SiC photoelectrode material or its surface treatment it is not unreasonable to achieve 5% STH efficiency, for which the calculation below was carried out.

Two basic types of PEC reactors were analyzed in this techno-economic analysis: "Type 3" (fixed planar array) and "Type 4" (concentrated with tracking system). The plant size was calculated based on the STH efficiency, the average daily solar energy (6.19 kW/m^2 and 6.55 kW/m^2 for Type 3 and Type 4, respectively [56]) and the amount of H_2 produced per day (1 ton). The cost for the PEC materials, the Plexiglas (reactor encapsulation for both Type 3 and 4 plus the concentrator for Type 4) and the foundation/erection was calculated based on the production plant size. These were the only variables used in our analysis and all other costs outlined in the "capital cost" sheet of the H2A V3 model were kept constant (as they are related to the amount of H_2 produced per day, 1TPD). These three variables were also the only parameters considered for replacement costs. The lifetime of the PEC components was 2 years in all cases. The Plexiglas (concentrator and/or encapsulation) and the foundation/erection were replaced every 10 years. The lifetime of the production plan was set to 40 years. Throughout this analysis, the costs for encapsulation (\$39/m^2) and foundation/erection (\$22/m^2) were kept constant [56], whereas variation of the STH efficiency and the cost for PEC materials was introduced for sensitivity analysis.

A Type 3 photo-reactor (baseline) was first considered here, with an absorber material (a-Si and a-SiC) cost of \$28/m^2 [57,58] and the STH efficiency of 5%, a representative of the efficiency achieved with a-SiC -based HPE devices (5-6%). In this situation, a cost of \$19.3 per kg of H_2 is obtained. Using a similar material cost and STH efficiency, we then calculated the costs for a Type 4 photo-reactor with different concentration factors. Table 5 summarizes the results.

Table 5 Summary of costs for Type 3 and Type 4 photo-reactors with a varying concentration factor for the baseline case (material cost of \$28/m^2 and STH efficiency of 5%).

Type of Photo-reactor	Concentration factor	Cost (\$) /kg H_2	Note
Type 3	no	19.32	fixed planar array
Type 4	10	21.03	concentrated with tracking system
	15	18.39	
	20	13.71	

The above results demonstrates that the cost per kg of H_2 increases significantly with a 10x concentrator when compared to the baseline case used in Type 3 system, even though the total cost for PEC materials is reduced with the Type 4 system (divided by 10 when compared to the planar array system). The high hydrogen production cost (\$21.0) is related to the size of the production plant required for PEC systems with low STH efficiencies. Therefore, the capital cost is mainly governed by the concentrator cost (\$93.84/m^2) [56]. Increasing the concentration factor to 20x reduces the H_2 production costs down to \$13.7. This is because the cost of a concentrator decreases with increasing concentration factor, from \$93.84/m^2 and \$71.17/m^2 to \$36.73/m^2 for concentration factors of 10x, 15x and 20x, respectively [56]. It should be noted that the STH efficiency in the above analysis was considered unaffected by the concentration factor.

Next, we performed the sensitivity analysis in order to see how the cost for hydrogen production varies with the costs of material and STH efficiency. Three different scenarios were investigated.

Case #1 - Effect of the material cost (Type 3). In this case, the baseline STH value (5%) was used. Reducing the material cost (also referred as $Cost_{Abs}$) from \$28/m^2 to \$15/m^2 had a rather moderate effect on the cost per kg of H_2 (from \$19.3 to \$14.7). This is explained by the fact that the cost of the PEC material in all cases represents only a rather small fraction of the capital cost.

Case #2 - Effect of the STH efficiency (Type 3). Three different STH efficiencies, i.e. 15%, 10% and 5% (baseline) but with a fixed absorber material cost of \$28/m^2 was considered here. Increasing the STH efficiency to 10% reduced the cost to \$9.9 and finally, assuming a STH efficiency of 15%, a cost of \$6.7 per kg of H_2 was achieved.

Case #3 - Effect of the STH efficiency (Type 4). As Table 5 shows, increasing the concentration factor to 20x reduces the H_2 production costs significantly due to reduced cost of the concentrator. Now we want to see how much more reduction in the cost would be by a combined increase of both the STH efficiency and the concentration factor in Type 4 reactors. Here the material cost of \$28/m^2 (baseline) is used. The concentration factor is set at 20x. Increasing the STH efficiency from 5% to 10% had a significant impact on the hydrogen production cost, leading to \$7.1, a value comparable to that achieved with PEC systems capable of higher STH efficiency (15%) but integrated in Type 3 reactors. Finally, increasing the STH efficiency to 15% decreased the cost per kg of hydrogen to \$4.8, the lowest value achieved in this techno-economic analysis.

Figure 46 shows the cost per kilogram of hydrogen obtained in 3 different scenarios as described above, presented in the sensitivity analysis chart.

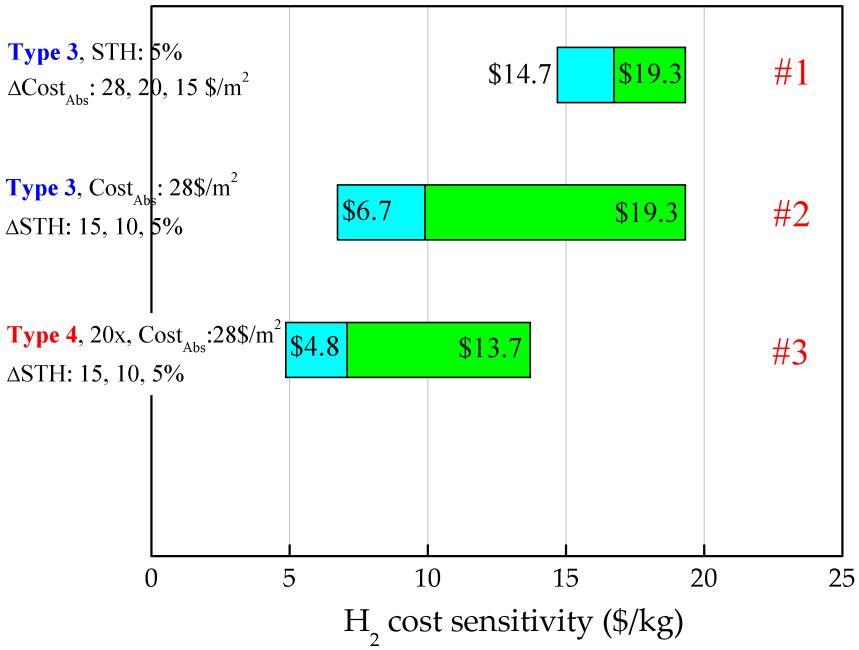

Figure 46 Hydrogen cost sensitivity calculated for 3 different sceneries and represented in the tornado chart fashion. The variable considered in each case is listed as "Δ variable" (with "variable" being the material cost, the light concentration factor or the STH efficiency).

Several key conclusions can be made from this analysis:

- A production cost of \$19.3 was obtained with a Type 3 reactor using STH efficiencies demonstrated in this program (5%) and absorber costs reported for amorphous silicon-based multijunction PV components (\$28/m^2). This value is lower than the goal fixed by DOE EERE for research program (\$22 per kg of H_2). One should keep in mind that the durability assumed in this calculation (2 years) has not been demonstrated yet.

- Increasing the STH efficiency to 15% with Type 3 reactors would reduce the hydrogen cost to $6.7. Although not demonstrated yet, this STH value is theoretically achievable with 2.0eV a-SiC -based PEC photoelectrodes.

- Reducing the material costs (Type 3) or the total area occupied by the solar absorbers (Type 4) has little effect on the cost of hydrogen if the STH efficiency is low (5%).

- The only way to significantly reduce the cost of hydrogen production is to increase the STH efficiency to at least 15%. It is interesting to note that a lower cost per kg of H_2 was achieved with concentrators when compared to planar array reactors, even though the use of concentrating tracking systems led to higher initial capital cost. One key advantage of Type 4 systems resides in the reduction of the absorber area (and their total cost). This has a significant impact when the PEC materials have to be replaced (every two years in this analysis).

6. Summary

In summary, great strides have been made in the fabrication of hybrid PV/PEC devices for hydrogen production. Three thin film photoelectrodes, including silicon-based compounds, copper chalcopyrite-based compounds, and metal oxides, have been developed during the course of this project. Through extensive experimentation, we have gained detailed knowledge about the fabrication and necessary properties of these thin film materials classes used for PEC water splitting, such as energy bandgap, band edge alignment, corrosion resistance and durability. A key development addressed the need for surface modification of the photoelectrodes which is *critical* to the performance of the hybrid PV/a-SiC and copper chalcopyrite-based devices. We have successfully integrated these thin film photoelectrodes with amorphous silicon solar cells and other PV devices either monolithically, or in a co-planar manner, and achieved reasonably good performance in hybrid PV/PEC devices. Main results and achievements from three material classes are presented in the following, respectively.

6.1 Amorphous Silicon-Based Compound Films

- We have fabricated state-of-the-art a-SiC:H films using the PECVD technique. Incorporation of carbon in amorphous silicon network enhances the bandgap to ≥ 2.0eV and adding H_2 during fabrication has led to a material with low defects.
- To investigate the quality of the material, a-SiC:H with Eg of 2.0 eV was first used as the active layer in single junction solar cell. The device showed an efficiency of ~7%, which indicated that the a-SiC:H produced is of high-quality.
- Next, we fabricated a-SiC photoelectrodes with a-SiC(p)/a-SiC(i) configuration, which exhibited photocurrent over 7 mA/cm^2 at potential -1.4 V (V vs. Ag/AgCl) in pH2 electrolyte, which indicated that the material was suitable for PEC applications.
- We then successfully integrated the a-SiC photoelectrode with an a-Si tandem solar cell monolithically, fabricated by the PECVD technique in the same cluster tool system. This hybrid device presents a flatband potential of ~ +0.90 V (vs. Ag/AgCl at pH2) below the H_2O/O_2 half-reaction potential, indicating it is in an appropriate position to facilitate water splitting. With surface treatment using Ru nanoparticles, the hybrid PV/a-SiC device exhibits a photocurrent of 3 mA/cm^2 in 0.5 M H_2SO_4 electrolyte.
- To further improve the efficiency of the PEC device we replaced the a-Si tandem "engine" with a high performance crystalline Si solar cell (also fabricated in the same PECVD reactor), which achieved a photocurrent of 4.91 mA/cm^2, or equivalent to a STH efficiency of 6.1%.
- Finally, we demonstrated that the hybrid device presents good corrosion resistance with a durability of up to 790 hours in 0.25 M H_2SO_4 electrolyte for water splitting, operating with the photocurrent of 3-4 mA/cm^2, biased by 1.3-1.5 V.

6.2 Copper Chalcopyrite-Based Films

- We have demonstrated that copper-chalcopyrite material class was capable of generating the photocurrent density level required for efficient water splitting. Our thin films were synthetized using conventional co-evaporation techniques currently used by the PV industry for $CuInGaSe_2$ solar cells. Our initial work on 1.68eV $CuGaSe_2$ (without containing In) showed that this material can generate up to 14 mA/cm^2 and is durable for up to 400 hours at a 5% STH level. This material falls short in terms of surface energetics and generates very little photovoltage. Therefore, majority of the bias must come from the PV drivers.
- We have fabricated a co-planar device using three series-connected a-Si solar cells and one $CuGaSe_2$ photocathode. A STH efficiency of 3.7% was measured under outdoor AM1.5G illumination. This value was calculated using the short circuit photocurrent density generated by this device and Faradaic efficiency. In a mechanical stack made with a poly-Si solar cell and a CuGaSe2 photocathode, a 400 mV anodic shift was observed leading to photocurrent density of -5 mA/cm^2 at $0V_{RHE}$.
- We also fabricated a p-n junction type photoelectrode by reactive sputtering technique, in which the red zinc oxy-sulfide thin film was deposited on CuGaSe2. Ruthenium nanoparticles were then added as HER catalyst. A 250 mV anodic shift was observed in this p-n junction photoelectrode, leading to photocurrent density at $0V_{RHE}$ of -1.5 mA/cm^2. Further, combining this device with a poly-Si in a

mechanical stack configuration shifted the onset potential further (+400 mV anodically), leading to photocurrent density of -7 mA/cm2 at $0V_{RHE}$.

- Wide bandgap copper chalcopyrite thin film materials were developed. We demonstrated that Se could be substituted with S using a simple annealing step. Current densities in the -5-6 mA/cm^2 range were obtained with red 2.0eV $CuInGaS_2$ photocathodes.

6.3 Metal Oxide-Based Compound Films

- We have demonstrated that a WO_3-based hybrid photoelectrode was feasible. Specifically, we showed that WO_3 paired with an a-Si tandem solar cell could generate short circuit photocurrent density of 2.5 mA/cm^2, equivalent to STH efficiency of 3.1%. Long-term durability tests also demonstrated WO_3 ability to split water over extended periods, for up to 600 hours at current density levels of 2.0-2.5 mA/cm^2.
- Good results have been achieved with Mo:WO_3/WO_3 PEC bilayered systems, where only the top part of WO_3 films was modified (doped with Mo, 200nm thick). Surface analyses indicated significant band-edges shifts, leading to the formation of a built-in potential that promotes extraction of photogenerated carriers. At saturation, the photocurrent is increased from ~3 mA/cm^2 to ~3.6 mA/cm^2.
- We have also explored other low bandgap WO_3 alloys for water splitting applications. Our study showed that a bandgap of 2.2eV was achievable in $CuWO_4$. The large bulk resistance of this material can be reduced effectively by combining $CuWO_4$ nanoparticles with conductive carbon nanotubes using a spray deposition process, leading to saturation photocurrent densities in the 0.4-0.5 mA/cm^2 range. Further improvements on $CuWO_4$ have been achieved by addition of bismuth, resulting in an increased conductivity by a factor of 100.

6.4 Techno-economic analysis

The techno-economic analysis performed with a-SiC material class demonstrated that the hydrogen production cost of $19.3 can be achieved with a Type 3 reactor assuming a STH efficiency of 5% that is close to what has been demonstrated in this program (~4%) and absorber costs reported for amorphous silicon-based multijunction PV components ($28/m^2). This value is lower than the goal fixed by DOE EERE for research program ($22 per kg of H_2). One should keep in mind that the durability assumed in this calculation (2 years) has not been demonstrated. Increasing the STH efficiency to 15% with Type 3 reactors would reduce the hydrogen cost to $6.7. Although not demonstrated yet, this STH value is theoretically achievable with 2.0eV a-SiC-based PEC photoelectrodes. Reducing the material costs (Type 3) or the total area occupied by the solar absorbers (Type 4) has little effect on the cost of hydrogen if the STH efficiency is low (5%). The only way to significantly reduce the cost of hydrogen production is to increase the STH efficiency. It is interesting to note that a lower cost per kg of H_2 was achieved with concentrators when compared to planar array reactors, even though the use of concentrating tracking systems led to higher initial capital cost. One key advantage of Type 4 systems resides in the reduction of the absorber area (and their total cost). This has a significant impact when the PEC materials have to be replaced (every two years in this analysis).

7. Outlook

At this point, we can conclude that the most promising materials investigated in this project are the a-SiC and the copper chalcopyrite-based thin film photoelectrodes. The hybrid PV/a-SiC device, using a crystalline Si solar cell as "engine", produced a photocurrent of 4.91 mA/cm^2, or equivalent to a STH efficiency of 6.1% and exhibited a durability of nearly 800 hours when operating under a photocurrent of 3~4 mA/cm^2 in 0.25 M H_2SO_4 electrolyte. However, more tests are necessary to ensure that the hybrid device can perform over a similar period without assistance of any external bias. In the case of the copper chalcopyrite photoelectrode, the hybrid PV/CGSe device exhibited a photocurrent of 3.5 mA/cm^2, or a STH efficiency of 4.3%, with durability up to 420 hours at a current bias of 4 mA/cm^2 in 0.5M H_2SO_4.

While we are encouraged by the above mentioned improvements in the hybrid PV/PEC devices which have established the viability using a low-cost approach to fabricate photoelectrodes for water splitting, we are aware of the tremendous difficulties that still lie ahead. In pursuing an environmentally benign approach for hydrogen production and with respect to DOE's long-term goal for solar-powered water splitting, i.e., 20% STH efficiency at a cost of $\leq$\$4/kg H_2), we have only taken the first step in this long journey. We now reiterate the high-priority areas for future activities and a pathway towards a higher STH efficiency:

7.1 For hybrid PV/a-SiC device

- Further pursue understanding of the surface energy band structure of the a-SiC, measured in electrolyte, as this would provide vital information about how the a-SiC surface interacts with electrolyte and how to tailor its composition and properties for PEC applications.
- Further investigate the effect of metal nanoparticles on the PEC performance of the hybrid device.
- Measure the Faradaic efficiency of hydrogen evolution on the hybrid PV/a-SiC devices.
- Find an optimum electrolyte (pH or conductivity) which helps hydrogen evolution while it maintains good durability for the hybrid devices.
- Fabricating monolithic high-performance hybrid device, where an a-SiC photoelectrode will be integrated directly with a high performance Si PV cell, leading to a 15% STH efficiency and beyond.

7.2 For copper chalcopyrite-based compounds

- Identify methods to increase cells photovoltage,
- Discover passivation layers with both high HER catalytic activity and resistance to corrosion,
- Fabricate efficient 2.0 eV bandgap chalcopyrite-based PEC material,
- Integrate wide bandgap chalcopyrite-based PEC with high efficiency solar cells.

7.3 For metal oxides

- Fabricate a monolithic WO_3-based HPE device
- Improve water splitting activity of $CuWO_4$
- Discover new quaternary systems with promising PEC characteristics.

Published work under this research program

1. Amorphous silicon compounds

In peel review journal (6)

Surface Modification of a-SiC Photoelectrode Using Metal Nanoparticles.
F. Zhu, I. Matulionis, N. Gaillard, J. Hu, J. Gallon, and A. Madan, MRS Online Proceedings Library, Vol.1539, 1539-d10-09 (2013)

Surface Modification of a-SiC:H Photoelectrodes for Photocurrent Enhancement.
I. Matulionis, J. Hu, F. Zhu, J. Gallon, N. Gaillard, T. Deutsch, E. Miller, and A. Madan, Proc. SPIE Vol.7770. (2010)

Amorphous Silicon Carbide Photoelectrode for Hydrogen Production from Water using Sunlight
F. Zhu, J. Hu, I. Matulionis, T. Deutsch, N. Gaillard, E. Miller, and A. Madan, Book chapter, "Solar Energy", edited by: Radu D. Rugescu, ISBN 978-953-307-052-0, pp. 432, February 2010, INTECH

Development of a photovoltaic (PV)/photoelectrochemical(PEC) hybrid device with amorphous silicon carbide as the photoelectrode for water splitting.
J. Hu, I. Matulionis, F. Zhu, J. Gallon, T. Deutsch, N. Gaillard, A. Kunrath, E. Miller, and A. Madan, MRS Proceedings, Vol.1171, 1171-S03-05 (2009)

Amorphous Silicon Carbide Photoelectrode For Hydrogen Production Directly From Water Using Sunlight.
F. Zhu, J. Hu, I. Matulionis, Todd Deutsch，Nicolas Gaillard, A. Kunrath, E. Miller and A. Madan, Philosophic Magazine, 89:28,（2009）2723-2739

Solar-to-Hydrogen Photovoltaic/Photoelectrochemical Devices Using Amorphous Silicon Carbide as the Photoelectrode.
J. Hu, F. Zhu, I. Matulionis, A. Kunrath, T. Deutch, L. Kuritzky, E. Miller, and A. Madan, Proc. 23rd European Photovoltaic Solar Energy Conference, Valencia, Spain, 69 (2008)
.

Presented in international conferences (3)

The Potential of Using a-SiC:H as the Photoelectrode for Water Splitting.
F. Zhu, J. Hu, I. Matulionis, T. Deutsch，N.Gaillard, E. Miller, and A. Madan, presented at NHA hydrogen conference and Expo., Long beach, CA, May 3-6, 2010.

Development of a Corrosion-Resistant Amorphous Silicon Carbide Photoelectrode for Solar-to-Hydrogen Photovoltaic/ Photoelectrochemical Devices.
I. Matulionis, F. Zhu, J. Hu, J. Gallon, A. Kunrath, E. Miller, B. Marsen, and A. Madan, SPIE Solar Energy and Hydrogen 2008, San Diego, USA, 10–14 August 2008.

A-SiC:H Films used as Photoelectrodes in a Hybrid, Thin-film Silicon Photoelectrochemical (PEC) Cell for Progress Toward 10% Solar-to Hydrogen Efficiency.
F. Zhu, J. Hu, A. Kunrath, I. Matulionis,, A. Kunrath, B. Marsen, B. Cole, E. Miller, and A. Madan, SPIE Solar Hydrogen and Nanotechnology 2007, San Diego, USA, 26–30 August 2007.

2. Copper chalcopyrite compounds

In peel review journal (7)

Development of Chalcogenide Thin Film Materials for Photoelectrochemical Hydrogen Production.
N. Gaillard, D. Prasher, J. Kaneshiro, S. Mallory, M. Chong, Material Research Society Proceedings, in press (2013).

Analysis of $CuIn_{0.7}Ga_{0.3}Se_2$ solar cells with nanosecond pulse length laser induced breakdown spectroscopy.
J. M. D. Kowalczyk, J. J. Perkins, A. DeAngelis, J. Kaneshiro, S. A. Mallory, Y. Chang, N. Gaillard, arXiv:1301.1313 (2013).

I-III-VI2 (Copper Chalcopyrite-based) Thin Films for Photoelectrochemical Water-Splitting Tandem-Hybrid Photocathode.
J. M. Kaneshiro, A. Deangelis, X. Song, N. Gaillard, E. L Miller, Material Research Society Proceedings 1324, DOI: http://dx.doi.org/10.1557/opl.2011.964 (2011).

Progress in new semiconductor materials classes for solar photoelectrolysis.
E.L. Miller, N. Gaillard, J. Kaneshiro, A. DeAngelis, R. Garland, International Journal of Energy Research 34, 1215 (2010).

*Copper-silver chalcporyites as top cell absorbers in tandem photovolta**ic and hybrid** photovoltaic/photoelectrochemical devices.*
J. Kaneshiro, A. Deangelis, N. Gaillard, Y. Chang, J. Kowalczyk, E.Miller, Proceeding of the 35th Photovoltaic Specialists Conference, 002448 (2010).

Advances in Copper-chalcopyrite Thin Films for Solar Energy Conversion.
J. Kaneshiro, N. Gaillard, R. Rocheleau, E. Miller, Sol. Energy Mater. Sol. Cells **94**, 12 (2010).

Development of Chalcogenide Thin Film Materials for Photoelectrochemical Hydrogen Production.
N. Gaillard, D. Prasher, J. Kaneshiro, S. Mallory, M. Chong, Material Research Society Spring Meeting (symposium Z2.07), San Francisco (2013).

Presented in international conferences (3)

INVITED - *High Bandgap Copper Indium Gallium Disulfide Materials For Solar-Assisted Water Splitting.*
N. Gaillard, D. Prasher, J. Kaneshiro M. Chong, J. Hu, M. Weir, C. Heske, Electrochemical Society meeting, Symposium I3, 2548, San Fransisco (2013).

Development of Chalcogenide Thin Film Materials for Photoelectrochemical Hydrogen Production.
N. Gaillard, D. Prasher, J. Kaneshiro, S. Mallory, M. Chong, Material Research Society Spring Meeting (symposium Z2.07), San Francisco (2013).

Hybrid Photovoltaic/Photoelectrochemical Device Design Using I-III-VI2 Copper Chalcopyrite-Based Photocathodes.
J. M. Kaneshiro, Y. Chang, N. Gaillard, The Electrochemical Society PRIME meeting, Symposium B10, 1710, Hononlulu (2012).

3. Metal oxide compounds

In peel review journal (13)

Predicting a new photocatalyst and its electronic properties by density functional theory
P. Sarker, D. Prasher, N. Gaillard, M. N. Huda, J. Appl. Phys. 114, 133508 (2013).

A Nanocomposite Photoelectrode Made of 2.2 eV Band Gap Copper Tungstate ($CuWO_4$) and Multi-Wall Carbon Nanotubes for Solar-Assisted Water Splitting.
N. Gaillard, Y. Chang, A. DeAngelis, S. Higgins, and A. Braun, Int. Journal of Hydrogen Energy 38, 3166 (2013).

Between Photocatalysis and Photosynthesis: Synchrotron spectroscopy methods on molecules and materials for solar hydrogen generation.
D. K. Bora, Y. Hu, S. Thiess, S. Erat, X. Feng, S. Mukherjee, G. Fortunato, N. Gaillard, R. Toth, K. Gajda-Schrantz, W. Drube, M. Grätzel, J. Guo, J. Zhu, E. C .Constable, D. D. Sarma, H. Wang, A. Braun, Journal of Electron Spectroscopy and Related Phenomena, DOI:10.1016/j.elspec.2012.11.009 (2012).

Soft x-ray and electron spectroscopy to determine the electronic structure of materials for photoelectrochemical hydrogen production.
L. Weinhardt, M. Blum, O. Fuchs, S. Pookpanratana, K. George, B. Cole, B. Marsen, N. Gaillard, E. Miller, K-S. Ahn, S. Shet, Y. Yan, M. M. Al-Jassim, J. D. Denlinger, W. Yang, M. Bär, C. Heske, DOI:10.1016/j.elspec.2012.11.015 (2012).

Copper Tungstate (CuWO4)–Based Materials for Photoelectrochemical Hydrogen Production.
N. Gaillard, Y. Chang, A. Braun, A. DeAngelis, Material Research Society Proceedings 1446, DOI: http://dx.doi.org/10.1557/opl.2012.952 (2012).

Photoelectrochemical Reforming of Glucose for Hydrogen Production using a WO3–based Tandem Cell Device.
D. V. Esposito, R. V. Forest , Y. Chang , N. Gaillard, S. Hou , K. H. Lee , B. E. McCandless, R. W. Birkmire and J. Chen, Energy Environ. Sci. 5, 9091 (2012).

Effect of thermal treatment on the crystallographic, surface energetics and photoelectrochemical properties of reactively co-sputtered copper tungstate (CuWO4) for water splitting.
Y. Chang, A. Braun, A. Deangelis, J. Kaneshiro and N. Gaillard, J. Phys. Chem. C 115, 25490 (2011).

Hydrogen production from photo-driven electrolysis of biomass-derived oxygenates: A case study on methanol using Pt-modified WO3 thin film electrodes.
D. V. Esposito, J. G. Chen, R. W. Birkmire, Y. Chang, N. Gaillard, Int. J. Hydrogen Energ. **36**, 9632 (2011).

Status of Research on Tungsten Oxide-based Photoelectrochemical Devices at the University of Hawai'i.
N. Gaillard, Proc. SPIE, Vol. 7770, 77700V; doi:10.1117/12.860970 (2010).

Mo incorporation in WO3 thin film photoanodes: Tailoring the electronic structure for photoelectrochemical hydrogen production.
M. Bär, L. Weinhardt, B. Marsen, B. Cole, N. Gaillard, E. Miller, and C. Heske, Appl. Phys. Lett. **96**, 032107 (2010).

Improved current collection in WO3:Mo/WO3 bilayer photoelectrodes.
N. Gaillard, B. Cole, B. Marsen, J. Kaneshiro, E.L. Miller, L. Weinhardt, M. Bär, C. Heske, K. -S. Ahn, Y. Yan, and M. M. Al-Jassim, J. Mater. Res. **25**, 45 (2010).

Surface Modification of Tungsten Oxide-Based Photoanodes for Solar-Powered Hydrogen Production.
N. Gaillard, J. Kaneshiro, E. L Miller, L. Weinhardt, M. Bär, C. Heske, K.-S. Ahn, Y.Yan, M. Al-Jassim, J. Mater. Res. **25**, 1171 (2010).

Surface Modification of Tungsten Oxide-Based Photoanodes for Solar-Powered Water Splitting.
N. Gaillard, J. Kaneshiro, M. Al-Jassim, C. Heske, E. Miller, Proceeding of the Material Research Society Spring Meeting, 458, San Francisco (2009).

Presented in international conferences (7)

Development of metal tungstate alloys for photoelectrochemical water splitting.
D. Prasher, M. Chong, Y. Chang, P. Sarker, M. N. Huda, N. Gaillard, Proc. SPIE 8822, Solar Hydrogen and Nanotechnology VIII, 88220E-88220E-7 (2013).

Theory-Driven Metal Oxide Down-Selection for Photoelectrochemical Hydrogen Production: the Case of Metal Tungstates.

N. Gaillard, Y. Chang, D. Prasher, P. Sarker and M. N. Huda, Material Research Society Spring Meeting (symposium D10.02), San Francisco (2013).

INVITED - *Performance and Limits of 2.2 eV Copper Tungstate (CuWO4) Mineral for Photoelectrochemical Hydrogen Production.*
N. Gaillard, Electrochemical Society PRIME meeting, Symposium B10, 1741, Honolulu (2012).

Analysis of Functional and Dysfunctional Defects in Photoelectrode Materials for Solar Water Splitting.
A. Braun, N. Gaillard, Y. Chang, D. K Bora, K. Gajda-Schrantz, J. Guo, Z. Liu, K. Sivula, M. Grätzel, E. Constable, Electrochemical Society PRIME meeting, Symposium B10, 1709, Hononlulu (2012).

Copper Tungstate (CuWO4)–Based Materials for Photoelectrochemical Hydrogen Production.
N. Gaillard, Y. Chang, A. Braun, A. DeAngelis, Material Research Society Spring Meeting, Symposium U2.8, San Francisco, (2012).

INVITED - *Status of Research on Tungsten Oxide-based Photoelectrochemical Devices at the University of Hawai'i*.
N. Gaillard, SPIE Solar Energy+ Technology, 77700V-77700V-14, San Diego (2010).

Surface Modification of Tungsten Oxide-Based Photoanodes for Solar-Powered Hydrogen
N. Gaillard, J. Kaneshiro, E.L. Miller, L. Weinhardt, M. Bär, C. Heske, K. -S. Ahn, Y. Yan, and M. M. Al-Jassim, Material Research Society Spring Meeting (symposium S2-1), San Francisco (2009).

References

[1] A. Fujishima and K. Honda*, Nature*, **238**, 37 (1972).
[2] A. Kudo and Y. Miseki, *Chem. Soc. Rev*., **38**, 253 (2009).
[3] K. Maeda, K. Teramura, and K. Domen, *J. Catal*. **254**, 198 (2008).
[4] S. Mubeen, J. Lee, N. Singh, S. Kramer, G. D. Stucky and M. Moskovits. *Nature Nanotech*. **8**, 247 (2013).
[5] C. Liu, J. Tang, H. M. Chen, B. Liu, and P. Yang, *Nano Lett*. **13**, 2989 (2013).
[6] E. L. Miller; R. E. Rocheleau, S. Khan, *International Journal of Hydrogen Energy*, **29**, 907 (2004).
[7] S. Y. Reece, J. A. Hamel, K. S. Thomas, D. Jarvi, A. J. Esswein, J. J. H. Pijpers, D. G. Nocera, *Science,* **334**, 645 (2011).
[8] L. H. Hihara, A. Iwane, S. Voss, R. E. Rocheleau and Z. Zhang, *Corrosion Science*, **41**, 1403 (1999).
[9] A. Madan and M. P. Shaw, *The Physics and Applications of Amorphous Semiconductors*, Academic Press, San Diego, p.155 (1989).
[10] Z. Chen, H. Dinh, and E. Miller, *Photoelectrochemical Water Splitting – Standards, Experimental Methods, and Protocols"*, Springer, 2013, **Chapter 2**, pp.13.
[11] U.S. Department of Energy, "*Hydrogen and Fuel Cell Infrastructure and Technology – Multi-Year Research, Development and Demonstration Plan*", **Chapter 3** (Revision 2006).
[12] F. Zhu, J. Hu, I. Matulionis, T. Deutsch，N. Gaillard, A. Kunrath, E. Miller, and A. Madan, *Philosophical Magazine*, **89** (28-30), 2723 (2009).
[13] J. Hu, F. Zhu, I. Matulionis, A. Kunrath, T. Deutsch, E. Miller, and A. Madan, *Proc. 23rd European Photovoltaic Solar Energy Conference*, Valencia, Spain, 69 (2008).
[14] R. Memming, Semiconductor Electrochemistry, Wiley-VCH, 2001.
[15] J. Hu, F. Zhu, I. Matulionis, T. Deutsch, N. Gaillard, E. Miller, and A. Madan, *Res. Soc. Symp. Proc*. **1171**, 1171-S03-05 (2009)
[16] I. Lauermann, R. Memming, and D. Meissner, *J. Electrochem. Soc.* **144**, 73 (1997).
[17] A. Heller, E. Aharon-Shalom, W. A. Bonner, and B. Miller,. *J. Am. Chem. SOC*. **104**, 6942 (1982)
[18] M. Szklarczyk and J. O. Bockris, *J. Phys. Chem*. **88**, 5241 (1984).
[19] R. N. Dominey, N. S. Lewis, J. A. Bruce, D. C. Bookbinder, and M. S. Wrighton, *J. Am. Chem. Soc*. **104**, 467-482 (1982).
[20] I. Matulionis, J. Hu, F. Zhu, J. Gallon, N. Gaillard, T. Deutsch, E. Miller, and A. Madan, *Proc. SPIE*. **7770**, 32 (2010).
[21] F. Zhu, I. Matulionis, N. Gaillard, Y. Chang, J. Hu, J. Gallon, and A. Madan, *Res. Soc. Symp. Proc*. **1539**, 1073 (2013).
[22] N. Gaillard, *HNEI Interim Report*, August, 2012.
[23] M. Bär, W. Bohne, J. Röhrich, E. Strub, S. Lindner, M.C. Lux-Steiner, Ch.-H. Fischer, *J. Appl. Phys*. **96**, 3857 (2004).
[24] I. Repins, M.A. Contreras, B. Egaas, C. DeHart, J. Scharf, C.L. Perkins, B. To, R. Noufi, *Prog. Photovolt. Res. Appl.* **16**, 235 (2008).
[25] P. Jackson, D. Hariskos, E. Lotter, S. Paetel, R. Wuerz, R. Menner, W. Wischmann, M. Powalla, *Prog. Photovolt. Res. Appl*. **19**, 894 (2011).
[26] S. Wojtczuk, P. Chiu, X. Zhang, D. Derkacs, C. Harris, D. Pulver and M. Timmons, *Proc. 35th Photovoltaics Specialists Conference*, Honolulu, HI, 001259 (2010).
[27] O. Khaselev, A. Bansal, J.A. Turner, Int. *J. Hydrogen Energ*. **26**,127 (2001).
[28] A. J. Bard and M. A. Fox, *Acc. Chem. Res*. **28**,141 (1995).
[29] B. Marsen, S. Dorn, B. Cole, R. E. Rocheleau, E. L. Miller, Mater. *Res. Soc. Symp. Proc*. 974E, Warrendale, PA, 0974-CC09-05 (2007).
[30] J. Leisch, J. Abushama, and J. A. Turner, *ECS Meeting Abstracts,* **502**, 821-821 (2006).
[31] B. Marsen, B. Cole, E. L. Miller, *Sol. Energy Mater. Sol. Cells*, **92**, 1054 (2008).
[32] M. Turcu and U. Rau, *J. Phys. Chem. Solids*, **64**,1591 (2003).
[33] S. B. Zhang, S.-H. Wei, A. Zunger, *J. Appl. Phys*. **83**, 3192 (1998).
[34] D. Schmid, M. Ruckh, F. Grunwald, H. W. Schock, *J. Appl. Phys*. **73**, 2902 (1993).
[35] E. L. Miller, A. DeAngelis and S. Mallory, in Roel van de Krol and Michael Grätzel, eds., "*Photoelectrochemical Hydrogen Production", Electronic Materials: Science & Technology,* Volume **102**, Springer 2012.
[36] R. Abe, T. Takata, H. Sugihara and K. Domen, *Chem. Commun*. 3829 (2005).
[37] K. Maeda and K. Domen, *J. Phys. Chem. Lett.*, **1**, 2655 (2010)
[38] K. Maeda, M. Higashi, D. Liu, R. Abe and K. Domen, *J. Am. Chem. Soc.,* **132**, 5858 (2010)

[39] M. Bar, *J. Appl. Phys*. **96**, 3857 (2004).
[40] E. Miller, R. Rocheleau, X. Deng*, Int. J. Hydrogen Energy*, **28**(6), 615 (2003).
[41] H. Wang, T. Deutsch, J. A. Turner, *ECS Transactions*. **6**, 37 (2008).
[42] N. Gaillard, Y. Chang, J. Kaneshiro, A. Deangelis and E. L. Miller, *Proc. SPIE*, Vol. **7770**, 77700V; doi:10.1117/12.860970 (2010).
[43] S. Chen, L. Wang, *arXiv*:1203.1970**v1** [cond-mat.mtrl-sci] (2012).
[44] M.N. Huda, Y. Yan, C-Y. Moon, S-H. Wei, and M.M. Al-Jassim, *Phys. Rev.* **B 77**, 195102 (2008).
[45] B. Cole, B. Marsen, E.L. Miller, Y. Yan, B. To, K. Jones, and M.M. Al-Jassim, *J. Phys. Chem*. **C112**, 5213 (2008).
[46] Gaillard, N.; Cole, B.; Marsen, B.; Kaneshiro, J.; Miller, E. L.; Weinhardt, L.; Bar, M.; Heske, C, *J. Mater. Res*. **25**, 1 (2010).
[47] M. Bär, L. Weinhardt, B. Marsen, B. Cole, N. Gaillard, E. Miller, and C. Heske, *Appl. Phys. Lett*. **96**, 032107 (2010).
[48] L. Weinhardt, M. Blum, M. Bar, C. Heske, B. Cole, B. Marsen, and E.L. Miller, *J. Phys. Chem*. **C112**, 3078 (2008).
[49] A. Paracchino*;* V. Laporte*;* K. Sivula*;* M. Grätzel*;* E. Thimsen*. Nature Materials* **10***,* 456 (2011).
[50] U.S. Department of Energy, *Basic Research Needs for Superconductivity*, Report of the Basic Energy Sciences, 2006.
[51] Chang, Y.; Braun, A.; Deangelis, A.; Kaneshiro, J.; Gaillard, N. *J. Phys. Chem. C*, **115**, 25490 (2011).
[52] Arora, S. K.; Mathew T.; Batra, N. M. *J. Phys. D: Appl. Phys*, **23**, 460 (1990).
[53] Benko, F. A.; MacLaurin, C. L.; Koffyberg, F. P. *Mat. Res. Bull.,* **17**, 133 (1982).
[54] Chang, Y.; Braun, A.; Deangelis, A.; Kaneshiro, J.; Gaillard, N. *J. Phys. Chem. C*, **115**, 25490 (2011).
[55] B. D. James, J. M. Moton and W. G. Colella, *Guidance for Filling Out a Detailed H2A Production Case Study*, July 9, 2013.
[56] B. D. James, G. N. Baum, J. Perez and K. N. Baum, *Technoeconomic Analysis of PEC Hydrogen Production*, internal report (2009).
[57] A. Jager-Waldau, *Status and Prospectives of Thin Film Solar Cell Production*, European Commission, 2007.
[58] F. Yang, *Solar Cells - Thin-Film Technologies*, **Chapter 16**: "Large Area a-Si/µc-Si Thin Film Solar Cells", ed. By Prof. Leonid A. Kosyachenko, 2011.